INSTRUMENTATION AND MEASUREMENT SERIES

New Sensors and Processing Chain

Edited by
Jean-Hugh Thomas
Nourdin Yaakoubi

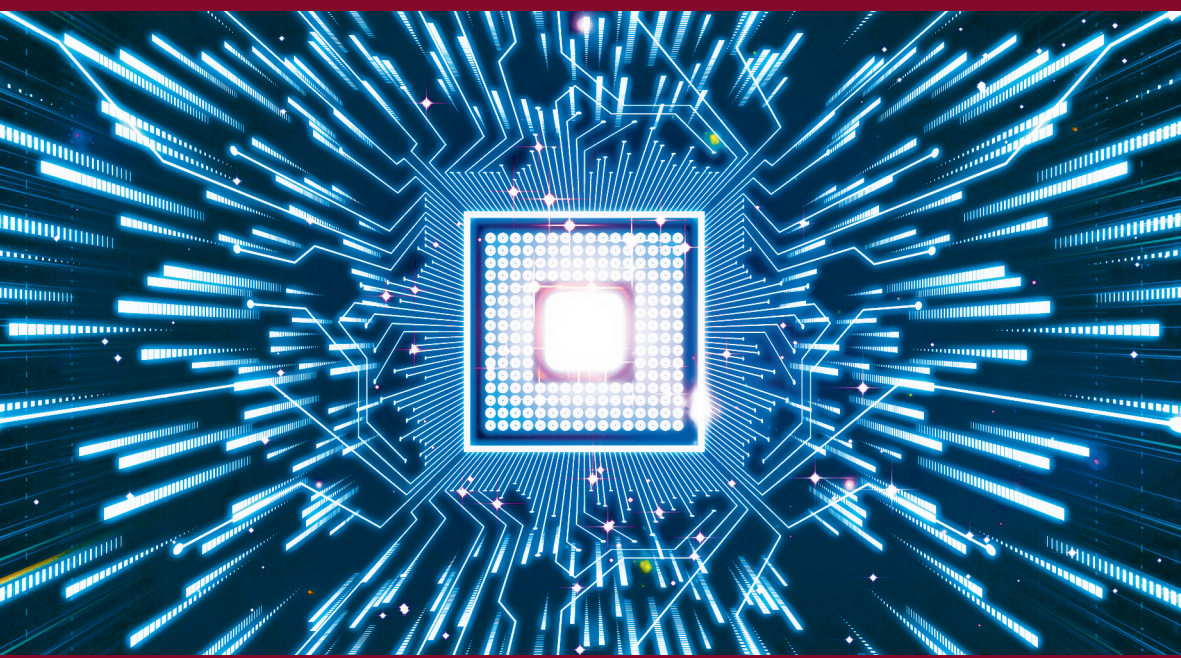

ISTE
WILEY

VISIT…

New Sensors and Processing Chain

Series Editor
Dominique Placko

New Sensors and Processing Chain

Edited by

Jean-Hugh Thomas
Nourdin Yaakoubi

ISTE
WILEY

First published 2014 in Great Britain and the United States by ISTE Ltd and John Wiley & Sons, Inc.

Apart from any fair dealing for the purposes of research or private study, or criticism or review, as permitted under the Copyright, Designs and Patents Act 1988, this publication may only be reproduced, stored or transmitted, in any form or by any means, with the prior permission in writing of the publishers, or in the case of reprographic reproduction in accordance with the terms and licenses issued by the CLA. Enquiries concerning reproduction outside these terms should be sent to the publishers at the undermentioned address:

ISTE Ltd
27-37 St George's Road
London SW19 4EU
UK

www.iste.co.uk

John Wiley & Sons, Inc.
111 River Street
Hoboken, NJ 07030
USA

www.wiley.com

© ISTE Ltd 2014
The rights of Jean-Hugh Thomas and Nourdin Yaakoubi to be identified as the authors of this work have been asserted by them in accordance with the Copyright, Designs and Patents Act 1988.

Library of Congress Control Number: 2014947783

British Library Cataloguing-in-Publication Data
A CIP record for this book is available from the British Library
ISBN 978-1-84821-626-6

Contents

PREFACE ix

CHAPTER 1. FABRICATION OF MICROELECTRODES USING ORIGINAL "SOFT LITHOGRAPHY" PROCESSES 1
Stéphane COTTE, Abdellatif BARAKET, François BESSUEILLE, Stéphane GOUT, Nourdin YAAKOUBI, Didier LEONARD and Abdelhamid ERRACHID

1.1. Introduction. 1
1.2. Materials and methods 2
1.2.1. Selective peeling 2
1.2.2. Localized passivation 3
1.3. Selective peeling process development and results 4
1.4. Localized passivation process development and results. 5
1.5. Conclusions. 8
1.6. Bibliography 8

CHAPTER 2. LOVE WAVE CHARACTERIZATION OF MESOPOROUS TITANIA FILMS 11
Laurianne BLANC, Grégory TORTISSIER, Cédric BOISSIÈRE, Corinne DEJOUS and Dominique REBIÈRE

2.1. Introduction. 11
2.2. Love wave platform 12
2.3. Mesoporous materials. 13
2.4. Environmental ellipsometric porosimetry 15
2.4.1. Measurement principle. 15
2.4.2. Sorption isotherm 16
2.5. Experimental set-up 17
2.5.1. Mesoporous sensitive layer deposition 17

2.5.2. Test bench 17
2.5.3. Results 19
2.6. Numerical simulations 19
2.6.1. Love wave propagation numerical model. 19
2.6.2. Simulation of sensor frequency response 23
2.6.3. Extraction of shear modulus of the TiO_2 film 25
2.7. Causes of mechanical stress induced by humidity sorption. 27
2.7.1. Capillary contraction 27
2.7.2. Swelling and residual sol–gel stress 28
2.8. Conclusions. 30
2.9. Bibliography 31

CHAPTER 3. IMMUNOSENSING WITH SURFACE ACOUSTIC WAVE SENSORS: TOWARD HIGHLY SENSITIVE AND SELECTIVE IMPROVED PIEZOELECTRIC BIOSENSORS. 35
Najla FOURATI and Chouki ZERROUKI

3.1. Introduction. 35
3.2. SAW sensors and measurement systems. 36
3.2.1. SAW transducers 36
3.2.2. Measurement instrumentation 38
3.2.3. An example of SAW device and conditioning system 40
3.2.4. SAW immunosensors' potential and their possible improvement 42
3.3. Immunosensing applications to evaluate SAW device performances 45
3.4. Survey of clinical applications of SAW immunosensor systems 54
3.4.1. Cardiac biomarker detection 55
3.4.2. Bacterial detection 57
3.4.3. Cell detection 57
3.4.4. Virus detection 60
3.4.5. Cocaine detection. 61
3.5. Conclusion 62
3.6. Bibliography 62

CHAPTER 4. AC NANOCALORIMETER ON SELF-STANDING PARYLENE MEMBRANE 69
Emmanuel ANDRE, Aitor FERNANDEZ LOPEANDIA, Jean-Luc GARDEN, Dominique GIVORD and Olivier BOURGEOIS

4.1. Introduction. 69
4.2. Advantage of this type of microdevice. 69

4.2.1. The samples 70
4.2.2. Measurement method: the AC calorimetry 70
4.3. Nanocalorimeter for measuring nano objects 71
4.3.1. The parylene membrane 72
4.3.2. Thermometer and heater in NbN_x 73
4.3.3. Manufacturing 74
4.3.4. Sample placement 77
4.4. Device performances 77
4.4.1. Temperature calibration 77
4.4.2. Thermal conductance of the empty cell 78
4.4.3. Dynamic characterization of an empty calorimetric cell 79
4.4.4. Heat capacity of an empty calorimetric cell 80
4.4.5. Heat capacity of a $GdAl_2$ microcrystal 81
4.5. Conclusion 83
4.6. Acknowledgments 83
4.7. Bibliography 83

CHAPTER 5. OSCILLATORY FAILURE DETECTION IN THE FLIGHT CONTROL SYSTEM OF A CIVIL AIRCRAFT USING SOFT SENSORS 85
Do Hieu TRINH, Benoît MARX, Philippe GOUPIL and José RAGOT

5.1. Introduction 85
5.2. Modeling of the studied system 86
5.3. Design of a soft sensor for the oscillatory failure detection 88
5.4. Fault detection by standard deviation test 90
5.4.1. Residual generation 90
5.4.2. Generation of failure indicators 93
5.4.3. Failure detection by standard deviation test 94
5.4.4. Discussion on failure detection by standard deviation test 96
5.5. Fault detection by correlation test 97
5.5.1. Pattern generation 98
5.5.2. Failure indicator generation and fault detection by correlation test 100
5.5.3. Discussion on the failure detection by correlation test 103
5.6. Conclusion 104
5.7. Acknowledgments 104
5.8. Bibliography 104

CHAPTER 6. EMBEDDED SENSORS FOR THE ANALYSIS OF DRIVERS' BEHAVIOR 107
Patrick PLAINCHAULT, Sébastien AUBIN, Patrice BRIAND, Jean-Michel AUBERLET and Thierry BOSCH

6.1. Introduction 107
6.2. Trajectories' observatory 109
6.2.1. Trajectory 110
6.2.2. The measurement 110
6.2.3. Bragg fibers 110
6.2.4. Resistive sensors 112
6.2.5. Electromagnetic loops 114
6.3. The sensors' network 115
6.3.1. Spacing between the sensors 115
6.3.2. The sensor network's display 116
6.4. Weather conditions 117
6.5. Analysis processing 117
6.5.1. Analysis before installation 118
6.5.2. Analysis of the development's aftermath 120
6.6. Conclusion 122
6.7. Acknowledgments 122
6.8. Bibliography 123

CHATPER 7. LARGE DEFORMABLE ANTENNAS 125
Sylvain GIRARD, Hervé GILLES, Philippe LEPRINCE, Olivier CLOUARD, Mourad CHTIOUI, Isabelle BARBEREAU, Guillaume LESUEUR and Thomas MERLET

7.1. Introduction 125
7.2. Mechanical analysis 128
7.3. Optical instrumentation for deformable antennas 128
7.3.1. Principle of the optical sensor based on fiber ribbons 132
7.3.2. Principle of optical sensor based on polarization rotation 135
7.4. Experience on a planar structure 139
7.5. Conclusion 145
7.6. Acknowledgments 146
7.7. Bibliography 146

LIST OF AUTHORS 149

INDEX 153

Preface

Extracting information on a system is required to understand its state, to describe its behavior and to predict its early damage in order to be able to undertake the necessary corrective actions. The essential mechanism for data acquisition is the physical sensor, which can be electronic, chemical, biological, mechanical, acoustic, etc. For some years, the sensor environment has been changing. The sensor has become a central part of a more complex process that operates as a team, communicates, takes decisions and is able to diagnose the state of the system under surveillance. Hereafter, the sensor is in charge of several tasks, getting smaller and smaller, sharing information with other sensors in a communication network. The instrumentation chain, the processing chain and the decision-making process can be seen as a software sensor. This evolution of the sensor is noticeable in many fields as shown by the various conferences on the subject around the world.

The chapters proposed here reflect the abundance of work about instrumentation, from the sensor, often miniaturized, to the diagnosis.

Sensor miniaturization provides a gain in volume and mass for an increase in processing power, but requires high-precision manufacturing. For microsystem engineering, it is essential to have an expert knowledge of the materials and to work on the development of new technology addressed here such as thin film layer deposition, lithography and “soft lithography”. The latter is illustrated here with the aim of developing localized metallization processes for the microfabrication of electrodes to be used in electrochemical biosensors. The control of materials, technology and microsystem reliability is very useful to ensure the proper functioning of the device, which also requires the development of characterization techniques.

An example of microfabrication coupled with an original measurement device is given here for a highly sensitive ac-calorimeter. The characterization of the shear modulus of a mesoporous titania film, combining a Love wave sensor with environmental ellipsometric porosimetry is the subject of another chapter. In addition, readers will be able to notice the advantages of miniaturizing, in the framework of biosensors, called gravimetric surface acoustic wave (SAW) sensors specialized in biological particle recognition.

The improvement of functional safety is of major concern, particularly in the case of the flight control process of an aircraft. Readers will see how oscillatory failures on the control system are detected from comparisons between signals acquired by physical sensors and data provided by several models of the flight behavior of the aileron of the aircraft.

The automatic surveillance of roads is also taking advantage of the sensor evolution. Thereby, a network of optical and resistive sensors, linked by the same communication bus, embedded in the road, makes possible the analysis of the trajectories followed by the drivers.

The ingenuity of radar antennas highlighting a limited mechanical structure complexity, deformed and dynamically compensated, will grab the reader's attention. The surface distortions are measured from optical sensors based on fiber ribbons or polarization rotation and used to feed algorithms compensating the radiation patterns of the antenna subjected to deformation.

Jean-Hugh THOMAS
Nourdin YAAKOUBI
Acoustics Laboratory at the University of Maine –
LAUM UMR CNRS 6613
National School of Engineers of Le Mans – ENSIM
September 2014

1

Fabrication of Microelectrodes Using Original "Soft Lithography" Processes

1.1. Introduction

Nowadays, there is a significant need for low-cost analytical tools that are capable of giving fast and accurate detection for environmental and medical applications. Downsizing devices is the main answer to this issue. It permits a high analysis throughput as well as both a decrease in sample and reactant consumption and a decrease in the instrumentation cost.

The most widely used technology, at the present time, for downsizing devices is photolithography [BRA 94]. A photosensitive resin is spin-coated onto the substrate surface, which is then irradiated through a mask using ultraviolet (UV) light. Whether the resin technology is positive or negative, the irradiated regions or the non-irradiated regions are removed using a developer. Metallic microstructures can be obtained using sputtering and lift-off. This technology makes possible the mass production of micrometric and sub-micrometric structures. However, this technology is not low cost because of the requirement for clean room facilities and high-tech equipment. In addition, this technology is not suitable for non-planar surfaces and it is only applicable on photosensitive materials (e.g. photoresists).

A new type of substrate patterning, known as soft lithography [XIA 98], and more especially microcontact printing, has been developed by Professor Whitesides' team. A soft elastomeric stamp (typically made from

Chapter written by Stéphane COTTE, Abdellatif BARAKET, François BESSUEILLE, Stéphane GOUT, Nourdin YAAKOUBI, Didier LEONARD and Abdelhamid ERRACHID.

polydimethylsiloxane (PDMS)) with a relief structure is used to transfer it onto the substrate surface. In the microcontact printing (μCP) technique, the stamp is "inked" with a chemical solution and is then put into close contact with the substrate surface [XIA 98]. The stamp is peeled off and the surface is then patterned with the "ink".

The most popular application of μCP is the transfer of an alkanethiol as "ink" onto a gold surface [KUM 93]. Alkylthiols form a self-assembled monolayer (SAM) at the surface that protects gold from chemical etching. Whitesides' team has demonstrated that using this technology, patterns with characteristic features down to 30 nm can be achieved. Furthermore, this technology is of low cost. Whether the substrate is planar or not [JAC 95], various types of substrates can be used (e.g. silicon [XIA 95], glass [GEI 03] and polymer [HID 96]), and depending on the chemical function at the end of the alkyl chain, various surface chemistries can be obtained.

Our work aims at developing original localized metallization processes for the microfabrication of electrodes to be used in electrochemical biosensors. This technology is applied on polymer [BES 09] or glass substrates (work presented here). Two original processes using alkanethiol μCP are described: the first process consists of a selective peeling of the metal thin-film areas not protected by the SAM, which makes it possible to avoid any chemical etching step in the process; the second process consists of passivating, with the help of a SAM, a gold electroless catalytic coating deposited on the substrate, which makes it possible to trigger localized growth of the metal and to avoid the need for a homogeneous gold thin film deposited using Physical Vapor Deposition (PVD) onto the substrate surface.

1.2. Materials and methods

1.2.1. *Selective peeling*

For the selective peeling process, glass substrates coated with gold thin films were used. The thin film was deposited using PVD cathode sputtering (EMSCOPE SC 500). To improve the practical adhesion of gold to the glass substrate, a thin layer of silver nanoparticles was first deposited. More precisely, microscope soda-lime glass slides (Roth-Sochiel, Lauterbourg, France) were cleaned in a piranha solution (3:1 mixture of H_2SO_4 96% and H_2O_2 30%) at 130°C for 30 min. Glass slides were then rinsed in ultrapure water (MilliQ, Millipore) and dried under a continuous flow of nitrogen.

The thin layer of silver nanoparticles was prepared directly on the glass slide by successive immersion in a 4% KOH solution, a 0.2 $g.L^{-1}$ $SnCl_2$ solution and, finally, a 10 $g.L^{-1}$ $AgNO_3$ solution. Between each immersion, substrates were rinsed in ultrapure water. After drying under a continuous flow of nitrogen, substrates were metallized using PVD cathode sputtering. The thickness of the thin film was estimated to be about 20 nm following abacus.

For the selective peeling process, a monolayer of octadecanethiol was deposited by microcontact printing on the gold-coated substrate surface. To ensure this step, the PDMS stamp was stored in an ethanol solution of octadecanethiol (2 mM). After the octadecanethiol deposition, a glass substrate with adhesive on top (UHU glass adhesive, containing 2-hydroxyethylmathacrylate) was deposited onto the modified substrate. The two substrates were pressed to make possible the spreading of the adhesive along the whole area. The glass slides were then irradiated for 10 min under a UV lamp to ensure polymerization. After cooling, the glass slides were removed. On the gold coating side, areas not protected by the SAM were peeled off but removed gold parts exhibit the original pattern on the slide with the adhesive layer.

1.2.2. *Localized passivation*

Cleaned glass substrates (see section 1.2.1) were surface modified with 3- aminopropyltriethoxysilane (APTES) in order to obtain amino groups at the substrate surface. More precisely, substrates were immersed in a 1% APTES solution in methanol for 45 min. Substrates were then rinsed in methanol, ultrapure water and finally dried under a continuous flow of nitrogen.

The gold electroless catalytic coating was obtained by adsorbing gold nanoparticles on the amino groups at the substrate surface. For this matter, substrates were immersed in a gold nanoparticle solution for six hours. This catalytic coating was then passivated by octadecanethiol microcontact printing (2 mM ethanol solution).

For silver electroless metallization, the solution was prepared by mixing 0.5 g of $AgNO_3$, 0.02 g of $SnCl_2$, 31 mL of ultrapure water, 19 mL of ammonium hydroxide (25%) and 40 µL of formaldehyde. The solution was used at ambient temperature and metallization took place for 5 min.

1.3. Selective peeling process development and results

In the conventional microcontact printing process applied to gold substrates (Figure 1.1), localized SAM of octadecanethiol protects the substrate from chemical etching. Thus, microstructures are obtained by selective etching of unprotected areas. However, chemical etching necessitates the use of toxic solutions.

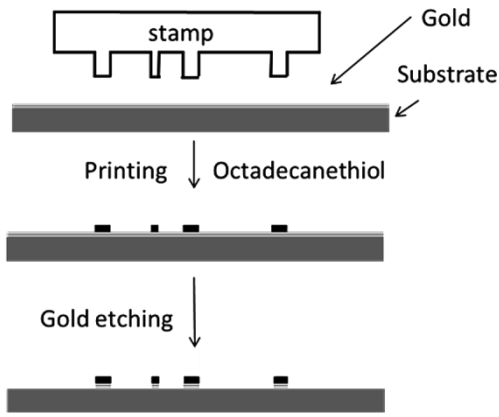

Figure 1.1. *Principle of conventional microcontact printing of alkanethiol to protect the gold layer from chemical etching*

In the first original process presented in this chapter (Figure 1.2), microcontact printing is used to obtain a localized monolayer of octadecanethiol. Unlike the conventional process, the gold layer is not etched but peeled off using an adhesive. Indeed, the SAM exhibiting a compact form prevents the adhesive from bonding to the gold layer. For unprotected areas, the adhesive sticks to the metal layer. To remove the adhesive, it is proposed to use a glass substrate that will also strongly stick to the adhesive. During the separation step, the bonding strength between the glass and the gold layer not covered by the octadecanethiol SAM is weaker than the bonding strength between the adhesive and the gold monolayer; thus, the latter will be peeled off.

Figure 1.3 shows an example of microstructures that can be obtained with the selective peeling process. The inset shows a close-up of the photographs and demonstrates the process feasibility for micrometric patterns (estimated smallest width about 60 μm).

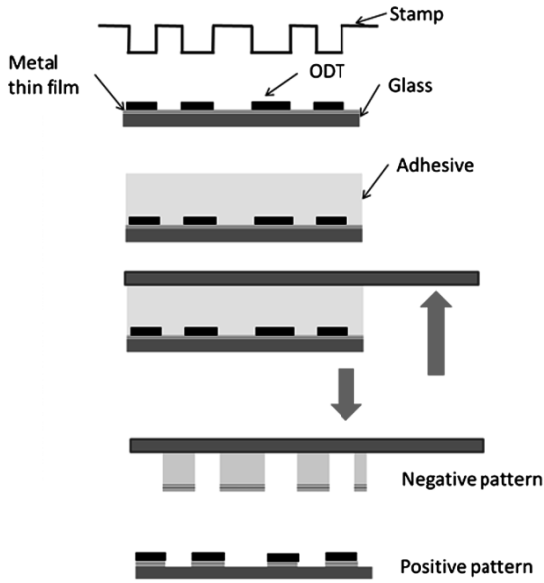

Figure 1.2. *Principle of the selective peel-off process*

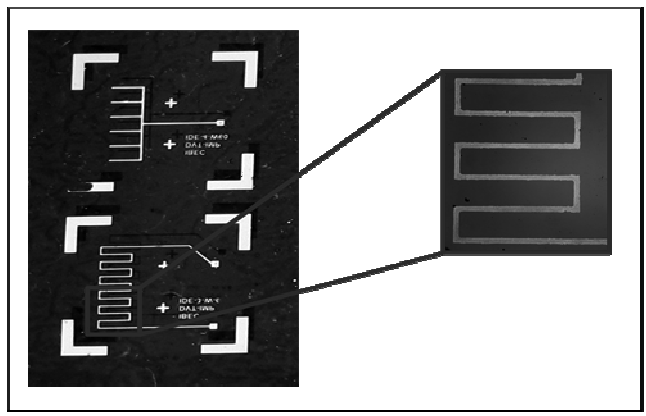

Figure 1.3. *Picture of an interdigitated electrode system obtained using the selective peel-off process applied with a gold thin layer and an alkanethiol self-assembled monolayer*

1.4. Localized passivation process development and results

In the localized passivation process, the aim is to grow a localized layer of electroless silver. Electroless metallization (Figure 1.4) is based on a

reaction between ions from the metal to be deposited and a chemical reducer, both being mixed in the same bath. The bath must be stabilized by the use of a complexing agent to limit spontaneous reduction of metal ions. Upon contact with a catalytic substrate surface (e.g. gold nanoparticles), reaction takes place and hence there is metal deposition specifically on this surface.

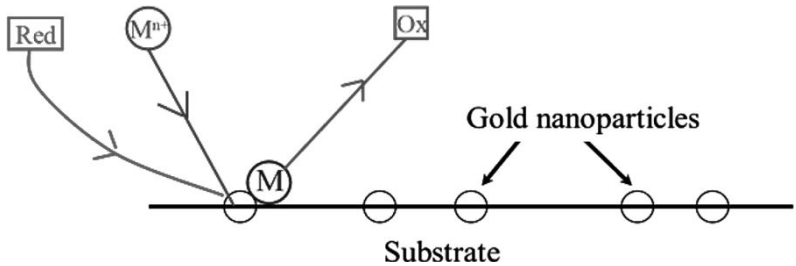

Figure 1.4. *Electroless metallization principle at the interface of a substrate coated with gold nanoparticles that are catalytic to silver electroless metallization*

The principle of the original process described in this chapter (Figure 1.5) consists of coating the whole surface of a glass substrate with a layer of gold nanoparticles that are catalytic to silver electroless metallization. In order to grow a localized silver electroless layer, octadecanethiol microcontact printing is used to passivate the catalytic layer. The octadecanethiol monolayer at the nanoparticle surface makes it possible to avoid any chemical etching at the surface. Thus, a silver deposit is obtained only in areas not protected by the SAM of octadecanethiol.

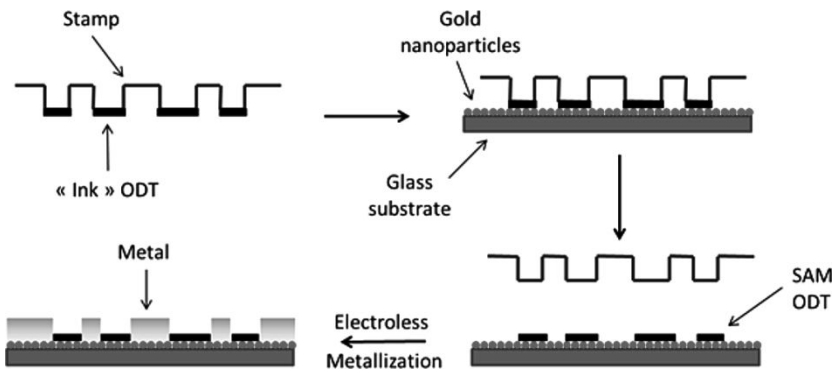

Figure 1.5. *Principle of the localized passivation process developed in this work*

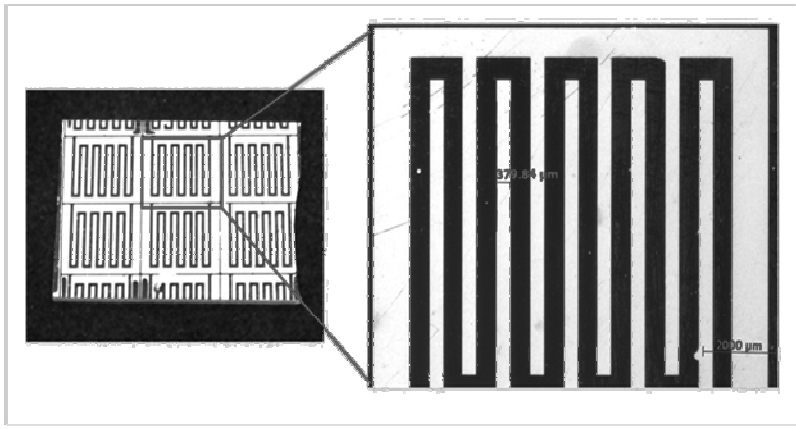

Figure 1.6. *Picture of a set of interdigitated electrodes obtained using the localized passivation process described in Figure 1.5*

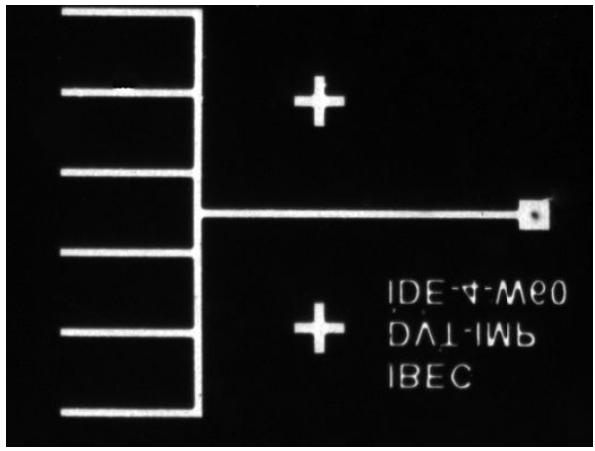

Figure 1.7. *Picture of a microelectrode obtained using the localized passivation process described in Figure 1.5. The smallest width is 60 µm*

Figure 1.6 shows an example of a set of interdigitated electrodes obtained using the localized passivation process based on a layer of gold nanoparticles, SAM localized deposition followed by silver electroless metallization. The pattern exhibits the smallest width dimension of about

300 μm. The same process was used to obtain electrodes exhibiting the smallest width of about 60 μm, as can be seen in Figure 1.7. It demonstrates the ability of this process to reproduce micrometric scale patterns.

1.5. Conclusions

Due to soft lithography and especially due to microcontact printing, two original processes making it possible to replicate microelectrodes were successfully developed.

In the first process (selective peeling process), an adhesive was used to reveal the patterns obtained using microcontact printing, which makes it possible to avoid any chemical etching step.

In the second process (localized passivation process), microcontact printing was used to obtain a localized passivation of a catalytic layer (gold nanoparticles), which makes it possible to obtain a localized silver electroless layer.

1.6. Bibliography

[BES 09] BESSUEILLE F., GOUT S., COTTE S., *et al.*, "Selective metal pattern fabrication through micro-contact or ink-jet printing and electroless plating onto polymer surfaces chemically modified by plasma treatments", *The Journal of Adhesion* , vol. 85, no. 10, pp. 690–710, 2009.

[BRA 94] BRAMBLEY D., MARTIN B., PREWETT P.D., "Microlithography: an overview", *Advanced Materials for Optics and Electronics,* vol. 4, no. 2, pp. 55–74, 1994.

[GEI 03] GEISSLER M., KIND H., SCHMIDT-WINKEL P., *et al.*, "Direct patterning of NiB on glass substrates using microcontact printing and electroless deposition", *Langmuir*, vol. 19, no. 15, pp. 6283–6296, 2003.

[HID 96] HIDBER P.C., HELBIG W., KIM E., *et al.*, "Microcontact printing of palladium colloids: micron-scale patterning by electroless deposition of copper", *Langmuir*, vol. 12, no. 5, pp. 1375–1380, 1996.

[JAC 95] JACKMAN R.J., WILBUR J.L., WHITESIDES G.M., "Fabrication of submicrometer features on curved substrates by microcontact printing", *Science*, vol. 269, no. 5224, pp. 664–666, 1995.

[KUM 93] KUMAR A., WHITESIDES G.M., “Features of gold having micrometer or centimeter dimensions can be formed through a combination of stamping with a elastomeric stamp and an alkanethiol “ink” followed by chemical etching”, *Applied Physics Letters*, vol. 63, no. 14, pp. 2002–2004, 1993.

[XIA 95] XIA Y., MRKSICH M., KIM E., *et al.*, “Microcontact printing of octadecylsiloxane on the surface of silicon dioxide and its application in microfabrication”, *Journal of the American Chemical Society*, vol. 117, pp. 9576–9577, 1995.

[XIA 98] XIA Y., WHITESIDES G.M., “Soft lithography”, *Annual Review of Materials Science*, vol. 28, pp. 153–184, 1998.

2

Love Wave Characterization of Mesoporous Titania Films

2.1. Introduction

In the last few years, mesoporous oxides have achieved a strong development due to their specific properties such as high active surface (150 to 1,000 m^2/cm^3), adjustable porosity (suitable for particles and species molecular trapping) and wide functionalizing and structuring possibilities [SAN 08]. Therefore, mesoporous oxide films have raised much interest for chemical sensor design [TIE 07].

In particular, Love wave sensors (guided shear horizontal surface acoustic wave) coated with mesoporous sensitive layers have shown good sensitivity and short-time response for volatile organic compounds (VOCs) [TOR 09] and heavy metal detection [GAM 14].

Parameters of the material may differ during vapor sorption, such as rigidity, viscoelasticity or permittivity. These properties must be characterized and modeled accurately to improve microsensor design. The literature provides little information about these nanostructured materials, especially when they are used in high frequencies. Note that mechanical properties of thin films, such as density and stiffness, strongly depend on their fabrication

Chapter written by Laurianne BLANC, Grégory TORTISSIER, Cédric BOISSIÈRE, Corinne DEJOUS and Dominique REBIÈRE.

and deposition processes [CAR 02]. Therefore, it is important to consider the films in their real operating conditions.

Several characterization techniques are commonly used for the characterization of Young's modulus, such as Brillouin light scattering [CAR 05], nanoindentation [GAI 09], or micro-traction [TAN 10]. However, they are difficult to carry out under humidity exposure.

Thus, a dedicated experimental set-up developed for the characterization of film shear modulus is presented in this work. It combines a Love wave sensor with environmental ellipsometric porosimetry.

Environmental ellipsometric porosimetry is generaly used to characterize mesoporous materials and presents many advantages [BOI 05]. In particular, measurements are performed *in situ* and are non-destructive. Young's modulus is calculated at the sorption cycle end and it corresponds to the fully hydrated film. Acoustic waves are used to determine film shear modulus throughout the sorption cycle.

In section 2.2, we describe the Love wave device. Then, mesoporous materials and environmental ellipsometric porosimetry (EEP) are described. The experimental device, combining acoustic wave and EEP, and the results will be presented. Simulations of Love wave propagation have been performed and shear modulus variations of a mesoporous titania film have been determined with a maximum variation of 2.1 GPa during the desorption. Finally, the possible explanations of this nonlinear reponse have been discussed, regarding the porous nature of the film and its specific fabrication process.

2.2. Love wave platform

The Love wave sensing principle is based on the perturbation of a guided shear horizontal surface acoustic wave.

The device consists of an AT cut quartz piezoelectric substrate (0°; 121.5°; 90°) allowing horizontal transverse polarization of acoustic waves. The Ti/Au interdigitated transducers (IDTs) consists of 44 split finger pairs with a 40 µm periodicity (λ) ensuring the wave generation. The acoustic path length (between the two transducers) is 164 λ. A 4.5 µm SiO_2 guiding layer was

deposited on the top of the quartz substrate in order to generate Love waves and to confine the acoustic energy [ZIM 01]. Adding a sensitive layer on the propagation path enabled the sorption of molecules (Figure 2.1) ensuring both amplification effect and possible specificity. The sorption modifies the physicochemical properties of the sensitive layer, which are measured through the phase velocity variations.

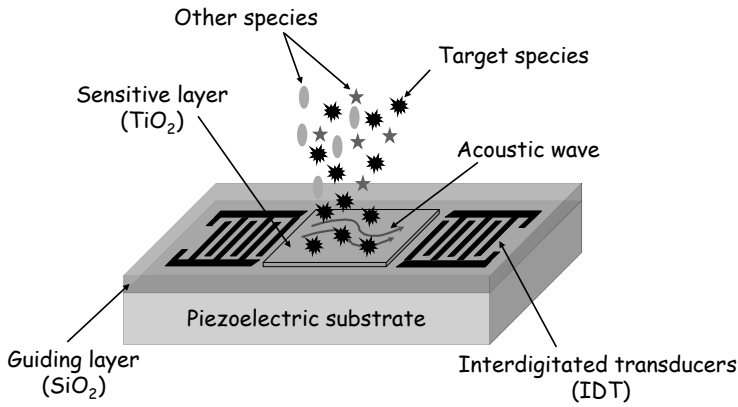

Figure 2.1. *Love wave sensor*

For high-resolution experimental measurements, the Love wave delay-line is inserted in the feedback loop of an amplifier in order to achieve an oscillator system. The real-time measured frequency shifts are linked to the wave velocity shifts (Figure 2.2).

The oscillator is based on the Barkhausen conditions. It consists of an amplifier and a variable attenuator in order to compensate the insertion loss of the acoustic device, a band pass filter and a coupler for sampling a part of the signal, which is measured with a universal counter (Agilent Technologies, HP53132A, 255 MHz Universal Counter, Santa Clara, CA). The oscillator presents a short-term stability of 1 Hz/s and the sensor synchronous frequency is about 117 MHz [MOL 04].

2.3. Mesoporous materials

A microporous material presents pores with a diameter less than 2 nm and a macroporous material, greater than 50 nm. Mesoporous oxides are defined

as porous oxides with pore diameters in the 2-50 nm range. Due to their pore size, these materials have very large surface areas up to 1,000 m^2/g. They can be functionalized, either during preparation or after mesostructure formation [NIC 05], which makes them very attractive for sensing applications.

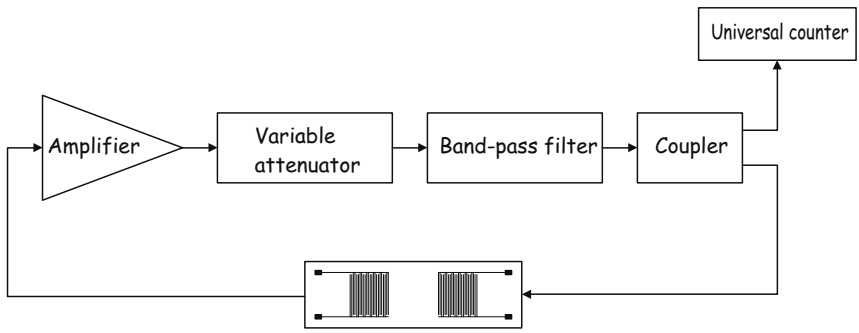

Figure 2.2. *Block diagram of the Love wave device oscillator*

Mesoporous titania films were prepared through the e*vaporation induced self-assembly* (EISA) process based on the sol–gel method [GRO 04]. The principle is based on the transformation of a liquid-based metal precursor in a wet gel by a set of chemical reactions at ambiant temperature (Figure 2.3).

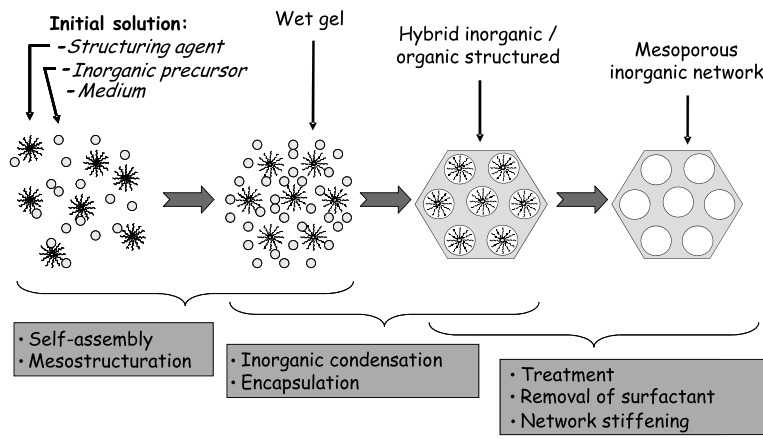

Figure 2.3. *Illustration of the EISA process [SAN 08]*

The synthesis of a solution is conventionally carried out at ambient temperature. The solution is formed of metal alkoxides (inorganic

precursors), surfactants (templating agents) and solvent. The addition of water leads to a competition between hydrolysis and condensation. The self-assembly between precursors and surfactant forms aggregates that can take many shapes (spherical, cylindrical or lamellar micelles) that allow the formation of an organized mesoporous structure. Once the solution is coated on a substrate by "spin" or "dip-coating", solvent evaporation leads to a rapid equilibrium between atmospheric pressure and water contained in the film and the organic–inorganic matrix begins to form. During this phase, any change in atmospheric composition may change the mesostructure. Finally, a thermal cure is used to extract the surfactant and consolidate the inorganic network [SAN 10].

2.4. Environmental ellipsometric porosimetry

Environmental ellipsometric porosimetry (EEP) is a non-destructive optical technique for thin-film characterization that is based on the change of polarization of a reflected laser beam onto a surface. Porosity, pore size distribution and specific surface area of thin porous films, from several nanometers to several micrometers thick [BOU 04], are determined through the measurement of their thickness and their refractive index under humidity exposure at ambient temperature [BOI 05].

This technique is widely used for mesoporous film characterization whose pore sizes are between 2 and 30 nm [LIC 10, ROU 06]. It can also be applied to multilayered systems [FUE 08].

A typical result consists of drawing water sorption isotherms in the film subjected to a continuous air flow with a controlled partial humidity pressure. Remember that a sorption isotherm is a curve characterizing the amount of physisorbed gas in the porous volume as a function of the proportion of applied gas.

2.4.1. *Measurement principle*

The EEP system enables the characterization of a mesoporous film at ambient temperature and pressure. It comprises a spectroscopic ellipsometer (SOPRA Co.) and a pressure controlled chamber. A humidity generator

provides a pulsed air flow with adjustable relative humidity (RH) level measured with a resistive humidity sensor.

During adsorption, humidity increases and water fills the pores gradually. During desorption, the condensed water is evaporated. The film thickness and refractive index are measured for each humidity step [MOG 02]. The amount of adsorbed water in the pores V_{water} is calculated using the Lorentz- Lorenz model [BAK 02] and the maximum value of the ratio of water volume on the film volume ($\frac{V_{water}}{V_{film}}$) when the pores are filled, leads to the determination of the film porosity. Analysis of the sorption isotherm, based on the Kelvin equation [BOI 05], enables us to determine the dimensions of pores and microchannels. This equation includes the radius of curvature of the meniscus in the pore. The pore size is determined during the adsorption, over the capillary condensation and the microchannel size is calculated during desorption. The Young's modulus of the film is determined by the modified Kelvin equation [BOI 05]:

$$E = \frac{d_0 RT}{V_L} \frac{\frac{1+p}{p}}{G} \frac{1}{k} \qquad [2.1]$$

with d_0, the thickness of unstressed film; V_L, the molar volume of water; $p = \frac{b}{a}$, ellipsoidal pores anisotropy that represents the ratio between the ellipsoidal larger radius a and the ellipsoidal small radius b; k, a variable whose value is derived from the modeling of the film thickness evolution, detailed in [MOG 02]; $G = 1 + \frac{C}{2p^2}$; $C = \frac{\ln\left(\frac{1+e}{1-e}\right)}{e}$ and e, the pore eccentricity.

2.4.2. *Sorption isotherm*

The amount $\frac{P}{P_0}$ is equal to the relative humidity (RH) in the case of water vapor, where P is the partial pressure of the applied gas and P_0 its saturating vapor pressure at the considered temperature, and is cycled between 0 and 100%. Different kinds of sorption isotherms can be observed according to the adsorbent material porous texture and to the type of adsorbent–adsorbate interactions. The *International Union of Pure Applied Chemistry* (IUPAC) proposed a classification of these isotherms into six categories [SIN 85].

For mesoporous materials, a sorption isotherm of type IV is typically obtained [SIN 85]. At low pressures, it is characterized by a multimolecular

adsorption on the mesopore surface. For higher pressure, a saturation level, with variable length, reflects an abrupt adsorption due to capillary condensation. The film saturation value level gives porosity [BOI 05]. A hysteresis between adsorption and desorption is generally observed. 0

2.5. Experimental set-up

2.5.1. *Mesoporous sensitive layer deposition*

At first, it is necessary to mask the sensor transducers to protect them and obtain a localized, reproducible and uniform film with limited side effects. In this work, a masking technique by Kapton (adhesive film) has been chosen for the device fabrication that presents the best trade-off between simplicity of film implementation and homogeneity, detailed in [TOR 09].

The experiments are performed with a mesoporous titania sensitive layer. The solution is composed of 20.66 g of ethanol, 1.45 g of water, 0.56 g of F127 (surfactant) and 3.347 g of a solution consisting of one $TiCl_4$ molecule to five molecules EtOH [CRE 03]. It is deposited on the sensor propagation path by "spin-coating" with an acceleration of 1,000 rpm/min/s and a speed of 2,000 rpm/min over 15 s. The sensor is then placed in a humidity chamber (75% RH) for 3 h (hydrolysation). Then, the layer is stabilized in an oven at 130°C for 24 h (solvent evaporation). Finally, the film is calcined at 400°C for 4 h to remove the structuring agent and to obtain a mesostructured thin layer (Figure 2.4). The film has a thickness of 100 nm with a good homogeneity. Nevertheless, edge effects related to Kapton are observed despite its removal immediately after solution deposition.

2.5.2. *Test bench*

A dedicated test bench has been developed, allowing the application of the RH level on the sensor and the simultaneous recording of the frequency response of the sensor and changes in optical properties of the titania layer (Figure 2.5).

The Love wave device is inserted into a suitable measuring cell with a gas inlet and openings allowing ellipsometer beam transmission and gas evacuation. The mass flow controllers, controlled by a software controller, provide the dry air–humidity mixture in order to obtain an adjustable RH

value. The delivered flow is constant and fixed at 5 L/min. Tests were carried out by increasing steps of 2% RH between 2 and 96% RH, and then by decreasing steps until 2% RH, exposing the device to full adsorption–desorption cycles. Each step lasts 30 s, in order to reach steady state.

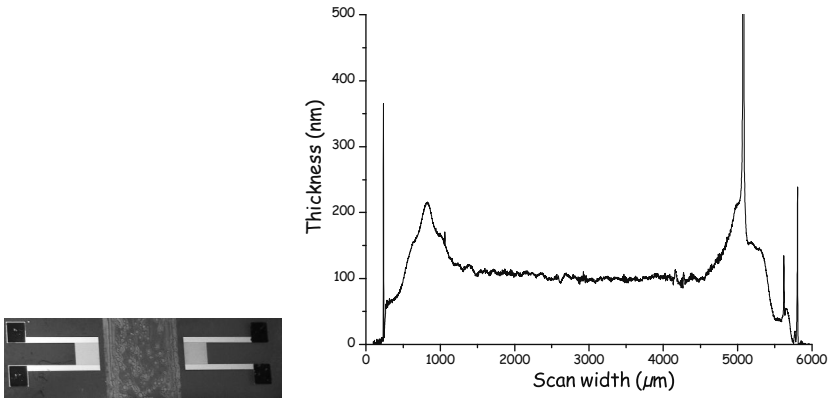

Figure 2.4. *a) Picture of mesoporous thin film coated on the acoustic path of the Love wave sensor and b) depth profile curve of the film obtained with profilometer (VEECO Dektak 150)*

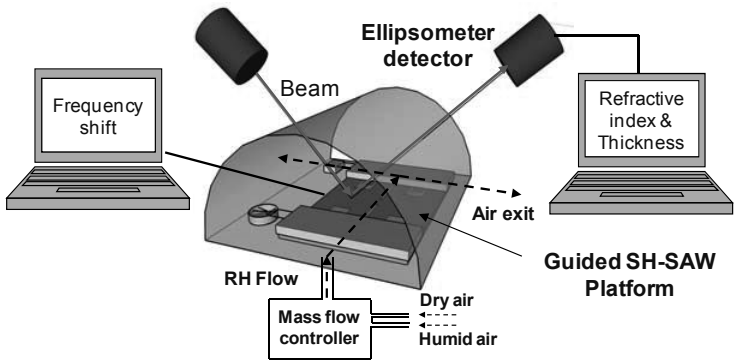

Figure 2.5. *Experimental set-up combining EEP (environmental ellipsometric porosimetry) with the Love wave platform*

2.5.3. *Results*

2.5.3.1. *Ellipsometric measurements*

Figure 2.6 shows the sorption isotherm of the TiO_2 film and the evolution of its thickness. The isotherm is a type IV, according the IUPAC classification, and shows porosity close to 25% for the considered film. The capillary condensation phenomenon appears around 70% RH, which is characteristic of TiO_2 films [BRE 09]. The film thickness is between 106.6 nm and 112.5 nm. The Young's modulus of the "wet" film is determined during film capillary contraction and is estimated at 8 GPa.

The distribution of pore size is not uniform and showed the presence of micropores (Figure 2.7). The average size is 9.8 nm–12.8 nm for the pores and 6.4 nm–8.3 nm for the microchannels.

2.5.3.2. *Acoustic measurements*

The device frequency shifts during the sorption are recording for each point of RH. The obtained curve presents a shape close to that of the sorption isotherm (type IV), with a capillary condensation threshold around 70% RH. The maximum frequency shift is 75 kHz (Figure 2.8).

2.6. Numerical simulations

2.6.1. *Love wave propagation numerical model*

A numerical model is used to determine the phase velocity of Love waves in a layered structure (Figure 2.9) [MAZ 04]. The model is based on the matrix resolution of propagation equations (equation [2.2]) of an acoustic wave in multilayer structures [KIM 97, ADL 90].

$$\begin{cases} \rho \dfrac{\partial^2 U}{\partial t^2} = C_{ijkl} \dfrac{\partial^2 U_1}{\partial x_j \partial x_k} + e_{kij} \dfrac{\partial^2 \Phi}{\partial x_j \partial x_k} \\ e_{jkl} \dfrac{\partial^2 U_1}{\partial x_j \partial x_k} - \epsilon_{jk} \dfrac{\partial \Phi}{\partial x_j \partial x_k} = 0 \end{cases} \qquad [2.2]$$

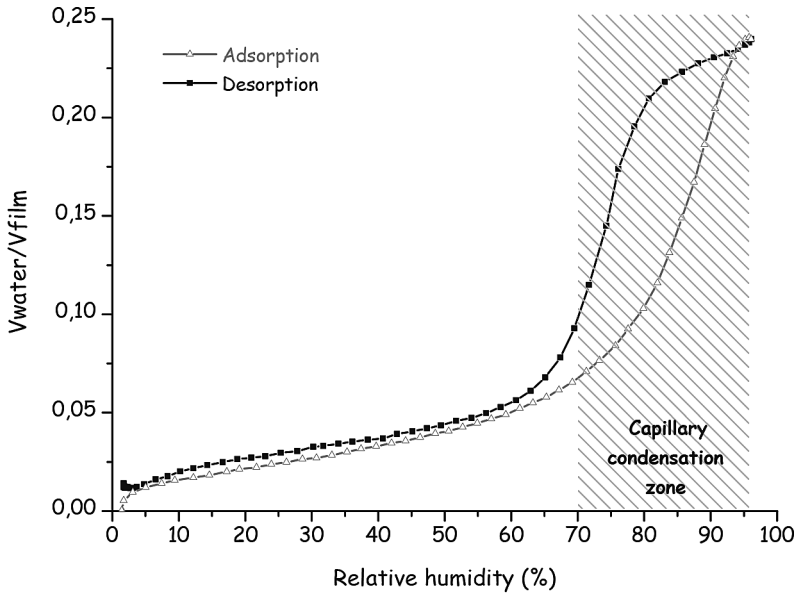

a)

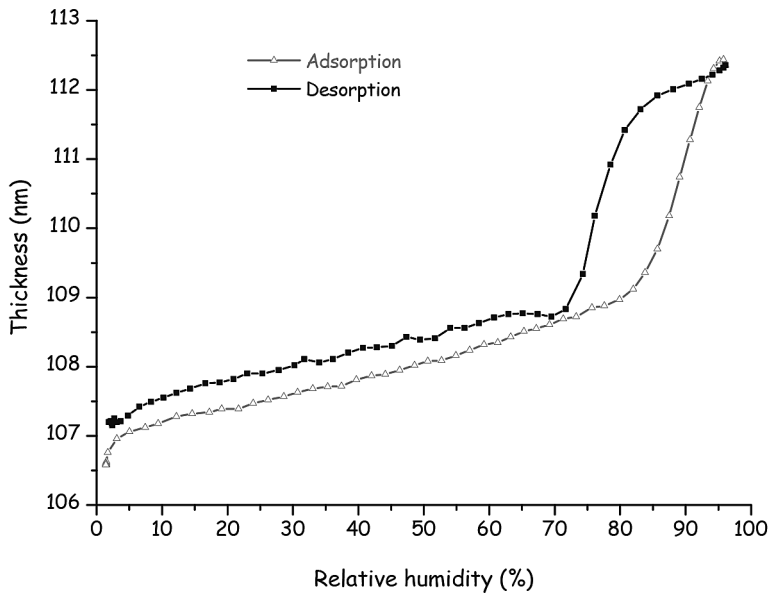

b)

Figure 2.6. *a) Adsorption–desorption isotherm and b) thickness variation of the mesoporous titania film, measured by ellipsometry at 18°C*

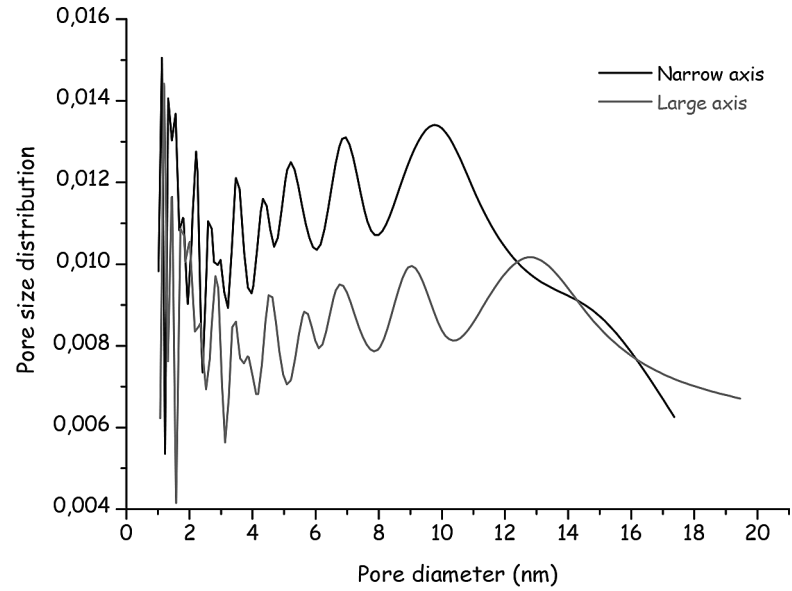

a)

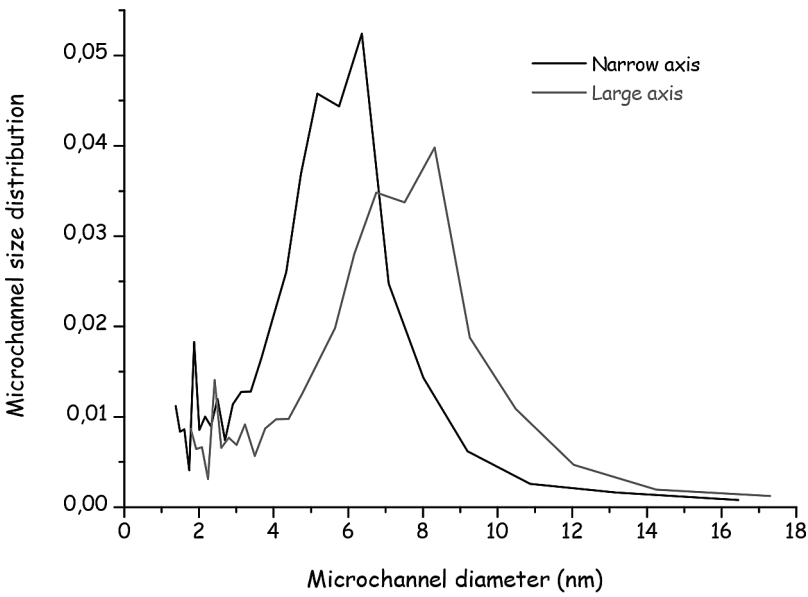

b)

Figure 2.7. *Distribution a) of the pore size and b) microchannels of the TiO_2 film, measured by ellipsometry at 18°C*

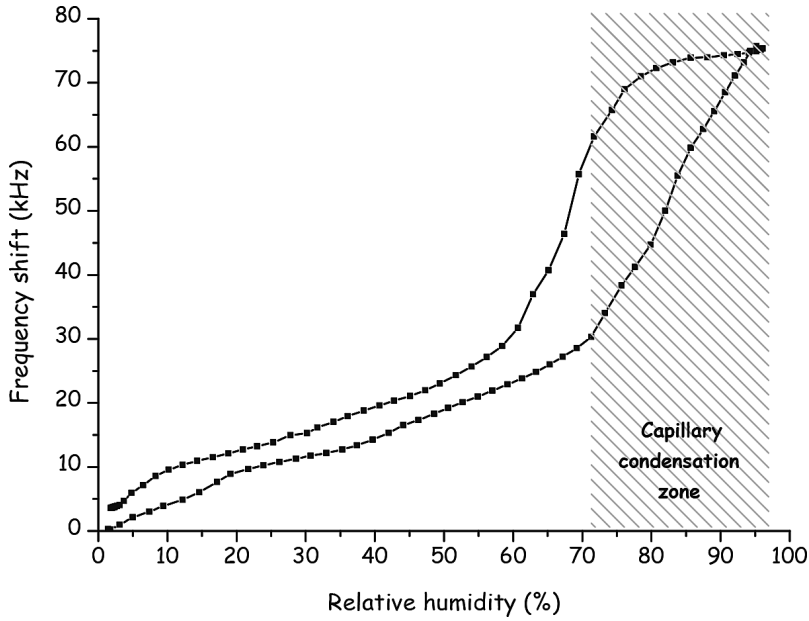

Figure 2.8. *Variation of the resonant frequency of the sensor during the humidity sorption by the Ti_2 film*

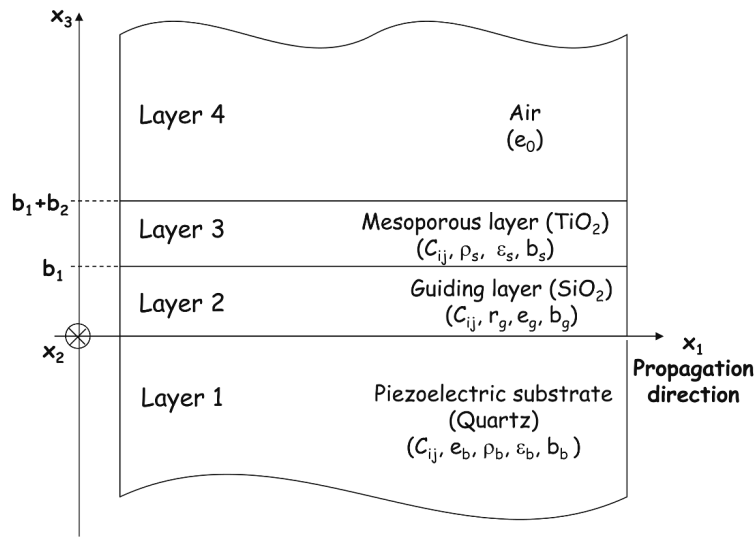

Figure 2.9. *Multilayer model of the Love wave sensor*

Figure 2.9 shows the layers of the device and the corresponding input parameters with $C_{\alpha\beta}$ the stiffness tensor, ρ the density, ϵ the permittivity, b the thickness, and e the piezoelectric tensor. The propagation equations are solved in each layer of the structure, and a transfer matrix that describes the amplitude of the displacement and the stress at any point of the layer is created. The product of the transfer matrices of each layer describes the acoustic wave propagation throughout the multilayer structure. The detail of the matrix solution of the equations is given in [MAZ 04].

The titanium oxide film is assumed to be cubic and isotropic [GRO 03]. Its stiffness tensor $C_{\alpha\beta}$ can be written as follows [ROY 00]:

$$C_{\alpha\beta} = \begin{bmatrix} C_{11} & C_{12} & C_{12} & 0 & 0 & 0 \\ C_{12} & C_{11} & C_{12} & 0 & 0 & 0 \\ C_{12} & C_{12} & C_{11} & 0 & 0 & 0 \\ 0 & 0 & 0 & C_{44} & 0 & 0 \\ 0 & 0 & 0 & 0 & C_{44} & 0 \\ 0 & 0 & 0 & 0 & 0 & C_{44} \end{bmatrix} \quad [2.3]$$

where the coefficients C_{11}, C_{12} and C_{44} depend on Young's modulus E and on Poisson's ratio ν:

$$C_{11} = \frac{E(1-\nu)}{(1+\nu)(1-2\nu)} \quad [2.4]$$

$$C_{12} = \frac{E\nu}{(1+\nu)(1-2\nu)} \quad [2.5]$$

$$C_{44} = \frac{E}{2(1+\nu)} \quad [2.6]$$

2.6.2. *Simulation of sensor frequency response*

At first, we simulate the device frequency shift under the same RH cycle (2% to 96% RH). Data extracted from ellipsometric measurements has been used as input parameters for the TiO_2 film, in particular:

– film thickness variations;

– Young's modulus, extracted at the end of the sorption cycle and supposed constant in a first part, equal to 8 GPa, corresponding to a shear modulus C_{44} = 3.1 GPa;

– mesoporous film density ρ_{meso}, determined as follows:

$$\rho_{meso} = (1 - \Phi) * \rho_{bulk} + \frac{V_{water}}{V_{film}} * \rho_{water} \qquad [2.7]$$

with Φ the porosity, ρ_{bulk} the TiO_2 density, $\frac{V_{water}}{V_{film}}$ the ratio of water adsorbed volume over film volume and ρ_{water} the water density.

Simulations are performed every 10% RH and simulated frequency shifts are plotted as a function of RH and compared to those obtained experimentally in Figure 2.10.

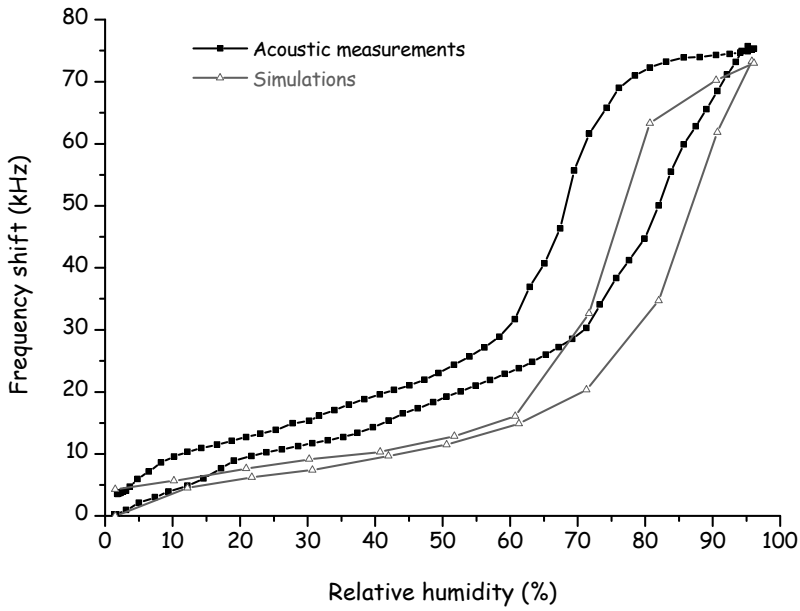

Figure 2.10. *Comparison between simulated (△) and experimental (■) frequency shifts*

Simulation results show isotherms with the same shapes as those derived from acoustic measurements. The threshold of capillary condensation is also

close to 70 % RH and the maximum frequency variation is the same as that measured (75 kHz).

The difference between measurements and simulations, in particular to high pressures, may be explained by the fact that the Young's modulus was assumed to be constant for the simulations. Due to the horizontal transverse polarization of Love waves, only the parameter C_{44} has an influence on the wave phase velocity calculation [LIU 08]. Therefore, we assume that the material stiffness varies with the humidity sorption.

2.6.3. *Extraction of shear modulus of the TiO_2 film*

The extraction principle of shear modulus during the sorption cycle is presented in Figure 2.11. Parameters used for simulations are derived from ellipsometric measurements ($\frac{V_{water}}{V_{film}}$, porosity ϕ and film thickness b_{meso}) and acoustic measurements (frequency shift ΔF_{water}), and from the literature (TiO_2 density ρ_{bulk}, water density ρ_{water}, permittivity ϵ, piezoelectric tensor $e_{\alpha\beta}$ and stiffness tensor $C_{\alpha\beta}$).

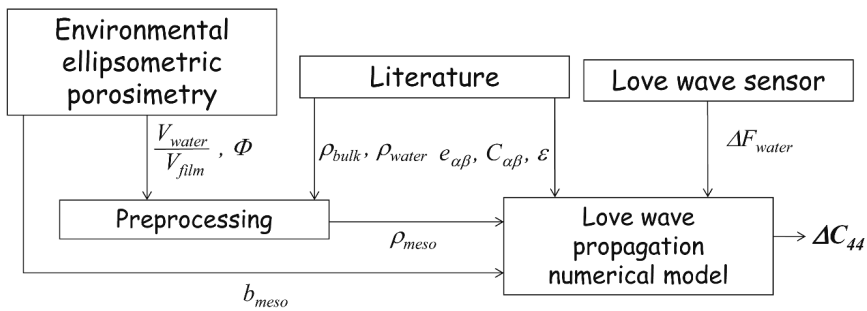

Figure 2.11. *Schematic diagram illustrating shear modulus extraction of the mesoporous TiO_2 film combining Love wave sensor and EEP*

Compared with previous simulations, the shear modulus is computed for each step of RH and is adjusted to fit simulated and experimental frequency shifts ($\pm$ 500 Hz).

Figure 2.12 presents so-obtained shear modulus variations. Four zones can be observed during adsorption:

– zone I: from 10 to 20% RH: decrease of the shear modulus, filling of the micropores;

– zone II: from 20 to 70% RH: linear decrease of the modulus, formation of a water film in the pores;

– zone III: from 70 to 85% RH: steep decrease of the shear modulus due to capillary condensation;

– zone IV: from 85 to 95% RH: strong increase of the shear modulus to reach the starting value, capillary contraction of the film.

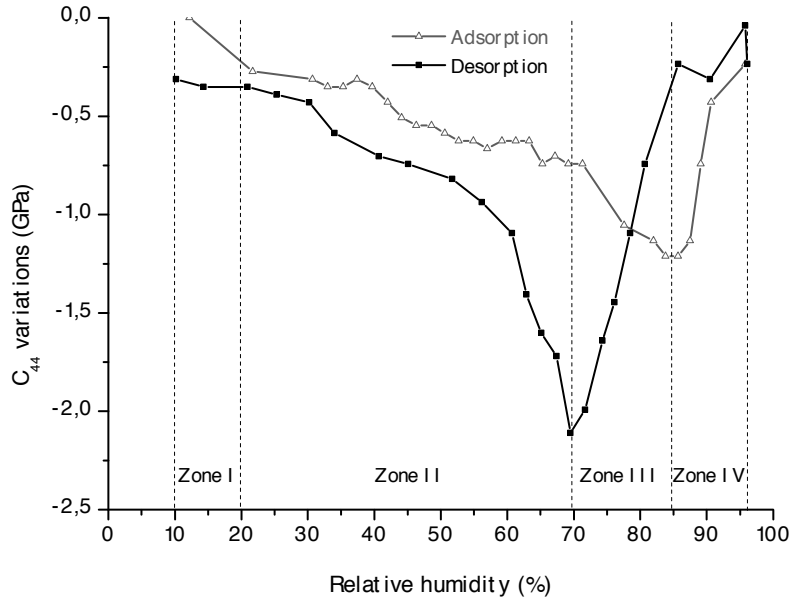

Figure 2.12. *Shear modulus variation of the film as a function of RH*

The last three steps of this process are observed similarly during desorption but with a lower value of the minimum modulus and at a lower RH. In zone I, the shear modulus remains almost constant, which may be attributed to more difficult desorption of water in micropores.

Shear modulus variations observed during the sorption highlight the influence of the water sorption in the film. During adsorption, the shear modulus decreases by 39%, then increases to its initial value (2.9 GPa, which corresponds to a Young's modulus close to 5 GPa). During desorption, the

shear modulus decreases by 67%, and increases to recover the initial value, after the capillary condensation threshold.

2.7. Causes of mechanical stress induced by humidity sorption

The strong nonlinear response at high exposure (zone IV) is not fully explained by water condensation. Three possible sources of stresses that alter the film mechanical behavior have been considered: capillary contraction, micropore swelling, and residual sol–gel stress. The first phenomenon is linked to the film's mesoporous nature whereas the two others are mainly side-effects of the specific fabrication process developed for the deposition of mesoporous oxides on quartz piezoelectric substrates.

2.7.1. *Capillary contraction*

During adsorption, the strong reincreasing of the shear modulus in the condensation zone suggests a contraction. The film is supposed to shrink because of the capillary forces induced by the water films growing on the surface of the pores and pulling on the pore walls, due to the strong affinity of water for itself as described in Figure 2.13. The shear modulus variations are not linear because the pores have different sizes within the film (Figure 2.7) and thus do not undergo capillary condensation at the same time: the smallest pores are filled first. The differences between adsorption and desorption are explained by the "ink-bottle" shape of the ellipsoidal pores, the "bottleneck"-shaped openings delay the release of water.

However, the thickness of the film (shown in Figure 2.6(a)) continuously grows as the humidity level increases during the adsorption phase of the adsorption–desorption cycle, which is not in agreement with the capillary contraction assumption. Therefore, capillary contraction should not be considered as the sole mechanical phenomenon occurring in the film, as it is only visible on the thickness variations induced by sorption as an inflection point in the course of the swelling process, when capillary condensation occurs.

For low RH levels, it was expected that the film should expand as a result of the filling of the smallest pores first, but afterward the film continues its expansion as the RH level increases. It does not fit the expected pattern

suggested by the shear modulus variations, that is, a constant (or slightly raising) slope up to the capillary condensation threshold followed by capillary contraction and then stress release. The expected hypothetical thickness curve is represented in Figure 2.14 and compared to the experimental measurements.

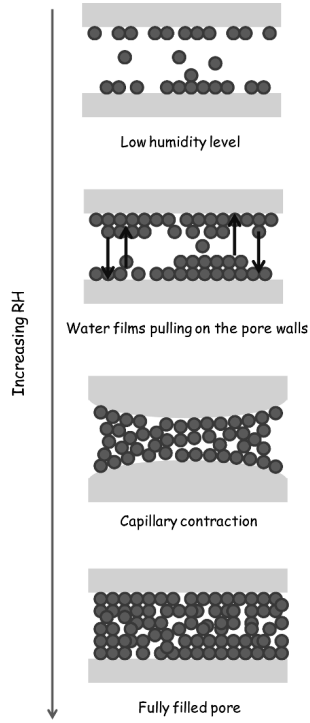

Figure 2.13. *Capillary contraction induces by water sorption*

2.7.2. *Swelling and residual sol–gel stress*

The original fabrication process of mesoporous films required high-temperature gradients that could have damaged the considered acoustic platform. Temperatures over 450°C are harmful to the Quartz piezoelectric substrate. The applied thermal cure, described in detail in [TOR 09], had to be modified to a longer cure process (1 h) with lower temperatures (400°C), and the question of full or partial crystallization had to be raised, as well as the

consequences of possible partial crystallization on the performances of the detection platform. Actually, our measurement system has provided relevant elements to discuss that issue.

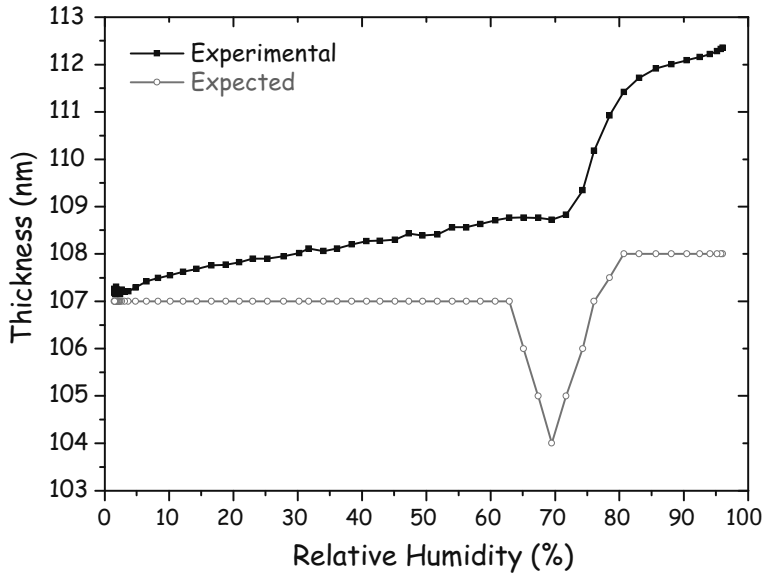

Figure 2.14. *Experimental and theoretical (for a fully crystallized film) thickness variations of the TiO_2 film*

Partial crystallization may have two major consequences: the presence of grain boundaries, microporous zones that act as a cement for TiO_2 grains, and a larger pore size distribution span than expected (Figure 2.7) [LAN 06]. As a consequence, there is a continuous filling of the pores from the minimum to the maximum applied humidity level, with the smallest pores being filled first. In addition, narrow pores swell more than large pores because, in narrow pores, water molecules and their clusters have the possibility of interacting with more than one of the pore walls at the same time, which means that more than one pore wall can contribute to the adsorption. In that configuration, the balance between adsorption heat and strain forces is stronger and increases the swelling phenomena along the thickness-axis (as it is not possible to swell in the substrate-plane direction because the film is rigidly bonded to the substrate). Therefore, adsorption with more than one micropore wall generates more heat, and, at the nanoscale, this high sorption energy is able to

slightly shift the surrounding atoms in order to reach the best surface interaction configuration possible.

Partial crystallization is also indirectly linked to the presence of a residual sol–gel stress. Before crystallization, the amorphous film is strongly stressed by the substrate, and this stress, (which is a contraction), is usually continuously released during crystallization, which means that full crystallization implies full stress release. Incomplete crystallization is thus responsible for an additional remaining "sol–gel stress" in the film in the direction perpendicular to the substrate. Moreover, the large thermal expansion coefficient of the quartz substrate tends to delay film crystallization [BAS 08]. One way for the film to relieve a part of this remaining contraction is through swelling, and once again the swelling phenomena occurs along the thickness-axis.

As a result, capillary contraction tends to be shadowed not only by overall condensation, but also by the presence of grain boundaries in the mesoporous matrix, which swell more than mesopores during sorption and by a residual sol–gel stress that also fosters swelling as a way to be released.

2.8. Conclusions

This chapter has presented a characterization method coupling ellipsometry porosimetric and Love waves acoustic detection to determine the evolution of the shear modulus of a mesoporous film subjected to a humidity sorption cycle. The possible explanations of the mechanical stress have been studied. The method was developed with a Love wave sensor with a resonance frequency of 117 MHz and a 110 nm sensitive TiO_2 film.

First, the method's principle is to obtain a humidity sorption isotherm by ellipsometry and Love wave, and then, the integration of ellipsometric measurements into a propagation Love waves simulation software. The shear modulus evolution of the film is obtained by fitting simulations and acoustic measurements. We have shown a significant influence of sorption on the mechanical behavior of the film with a shear modulus decreasing by 2.1 GPa during desorption, compared to typical value estimated at 3.1 GPa for dry and wet films.

Three possible sources of stresses have been considered: capillary contraction, swelling induced by micropore filling, and residual solgel stress. Capillary contraction is due to the nature of the mesoporous film and cannot be prevented. Micropore swelling is a consequence of the specific fabrication technique for mesoporous oxides on quartz piezoelectric substrates. Residual sol–gel stress is caused by the fabrication process as well, and is also linked to partial crystallization.

Improvements could thus come from optimizing the fabrication process, choosing another piezoelectric substrate (e.g. Langasite), or upgrading numerical models for data recovery. Moreover, thoroughly controlling crystallization and pore size may lead to better overall linearity or enhanced linearity in specific humidity ranges. In this context, the considered experimental set-up combining Love waves with EEP may soon prove again to be a powerful tool to study sensitive film mechanical parameters and the crystallization level.

2.9. Bibliography

[ADL 90] ADLER E.L., "Matrix methods applied to acoustic waves in multilayers", *IEEE Transactions on Ultrasonics, Ferroelectrics, and Frequency*, vol. 37, pp. 485–490, 1990.

[BAK 02] BAKLANOV M., MOGILNIKOV K., "Non-destructive characterisation of porous low-k dielectric films", *Microelectronic Engineering*, vol. 64, pp. 335–349, 2002.

[BAS 08] BASS J., GROSSO D., BOISSIÈRE C., *et al.*, "Pyrolysis, crystallization, and sintering of mesostructured titania thin films assessed by *in situ* thermal ellipsometry", *Journal of the American Chemical Society*, vol. 130, pp. 7882–7897, 2008.

[BOI 05] BOISSIÈRE C., GROSSO D., LEPOUTRE S., *et al.*, "Porosity and mechanical properties of mesoporous thin films assessed by environmental ellipsometric porosimetry", *Langmuir*, vol. 21, pp. 12362–12371, 2005.

[BOU 04] BOURGEOIS A., BRUNET BRUNEAU A., FISSON S., *et al.*, "Determination of pore size distribution in thin organized mesoporous silica films by spectroscopic ellipsometry in the visible and infrared range", *Thin Solid Films*, vol. 447–448, pp. 46–50, 2004.

[BRE 09] BREZESINSKI T., WANG J., POLLEUX J., *et al.*, "Templated nanocrystal-based porous TiO_2 films for next-generation electrochemical capacitors", *Journal of the American Chemical Society*, vol. 131, pp. 1802–1809, 2009.

[CAR 02] CARLOTTI G., COLPANI P., PICCOLO D., *et al.*, "Measurement of the elastic and viscoelastic properties of dielectric films used in microelectronics", *Thin Solid Films*, vol. 414, pp. 99–104, 2002.

[CAR 05] CARLOTTI G., CHÉRAULT N., CASANOVA N., *et al.*, "Elastic constants of low-k and barrier dielectric films measured by Brillouin light scattering", *Thin Solid Films*, vol. 493, pp. 175–178, 2005.

[CRE 03] CREPALDI E.L., DE A.A. SOLER-ILLIA G.J., *et al.*, "Controlled formation of highly organized mesoporous titania thin films: from mesostructured hybrids to mesoporous nanoanatase TiO_2", *Journal of the American Chemical Society*, vol. 125, no. 32, pp. 9770–9786, 2003.

[FUE 08] FUERTES M., COLODRERO S., LOZANO G., *et al.*, "Sorption properties of mesoporous multilayer thin films", *Journal of Physical Chemistry C*, vol. 112, no. 9, pp. 3157–3163, 2008.

[GAI 09] GAILLARD Y., RICO V.J., JIMENEZ-PIQUE E., *et al.*, "Nanoindentation of TiO_2 thin films with different microstructures", *Journal of Physics D: Applied Physics*, vol. 42, pp. 1–9, 2009.

[GAM 14] GAMMOUDI I., BLANC L., MOROTÉ F., *et al.*, "High sensitive mesoporous TiO_2-coated love wave device for heavy metal detection", *Biosensors and Bioelectronics*, vol. 57, pp. 162–170, 2014.

[GRO 03] GROSSO D., DE A.A. SOLER-ILLIA G.J., *et al.*, "Highly porous TiO_2 anatase optical thin films with cubic mesostructure stabilized at 700°C", *Chemistry of Materials*, vol. 15, pp. 4562–4570, 2003.

[GRO 04] GROSSO D., CAGNOL F., DE A.A., *et al.*, "Fundamentals of mesostructuring through evaporation-induced self-assembly", *Advanced Functional Materials*, vol. 14, no. 4, pp. 309–322, 2004.

[KIM 97] KIM H., "Propagation of surface acoustic waves in anisotropic piezolelectric multilayers: transfer matrix formalism", *The Korean Physical Society*, vol. 10, no. 2, pp. 125–132, 1997.

[LAN 06] LANCELLE-BELTRAN E., PRENÉ P., BOSCHER C., *et al.*, "Nanostructured hybrid solar cells based on self-assembled mesoporous titania thin films", *Chemistry of Materials*, vol. 18, pp. 6152–6156, 2006.

[LIC 10] LICITRA C., BOUYSSOU R., CHEVOLLEAU T., *et al.*, "Multi-solvent ellipsometric porosimetry analysis of plasma-treated porous SiOCH films", *Thin Solid Films*, vol. 518, pp. 5140–5145, 2010.

[LIU 08] LIU J.X., FANG D.N., WEI W.Y., *et al.*, "Love waves in layered piezoelectric/ piezomagnetic structures", *Journal of Sound and Vibration*, vol. 315, nos. 1–2, pp. 146–156, 2008.

[MAZ 04] MAZEIN P., ZIMMERMANN C., REBIÈRE D., *et al.*, "Love wave chemical sensors: design and optimisation. Case of organophosphorous compounds detection", *2004 IEEE International Symposium on Industrial Electronics*, vol. 1, pp. 31–35, 2004.

[MOG 02] MOGILNIKOV K., BAKLANOVZ M., "Determination of Young's modulus of porous low-k films by ellipsometric porosimetry", *Electrochemical and Solid-State Letters*, vol. 5, no. 12, pp. 29–31, 2002.

[MOL 04] MOLL N., DEJOUS C., REBIERE D., *et al.*, "An improved love-wave oscillator for low concentration chemical sensing application", *Procedings of XIXth Conference on Design of Circuits and Integrated Systems*, France, 2004.

[NIC 05] NICOLE L., BOISSIÈRE C., GROSSO D., *et al.*, "Mesostructured hybrid organic – inorganic thin films", *Journal of Materials Chemistry*, vol. 15, pp. 3598–3627, 2005.

[ROU 06] ROUESSAC V., COUSTEL R., BOSC F., *et al.*, "Characterisation of mesostructured TiO_2 thin layers by ellipsometric porosimetry", *Thin Solid Films*, vol. 495, pp. 232–236, 2006.

[ROY 00] ROYER D., DIEULESAINT E., *Elastic Waves in Solids I: Free and Guided Propagation*, Springer-Verlag, Berlin, Heidelberg, 2000.

[SAN 08] SANCHEZ C., BOISSIÈRE C., GROSSO D., *et al.*, "Design, synthesis, and properties of inorganic and hybrid thin films having periodically organized nanoporosity", *Chemistry of Materials*, vol. 20, pp. 682–737, 2008.

[SAN 10] SANCHEZ C., ROZES L., RIBOT F., *et al.*, "'Chimie douce': a land of opportunities for the designed construction of functional inorganic and hybrid organic-inorganic nanomaterials", *C.R. Chimie*, vol. 13, pp. 3–39, 2010.

[SIN 85] SING K., EVERETT D., HAUL R., *et al.*, "Reporting physisorption data for gas/solid systems with special reference to the determination of surface area and porosity", *Pure and Applied Chemistry*, vol. 57, no. 4, pp. 603–619, 1985.

[TAN 10] TANG J., WANG H., LIU R., *et al.*, "A directly strain measuring method for electroplated nickel micro-tensile test", *Microsystem Technologies*, vol. 16, no. 11, pp. 1839–1844, 2010.

[TIE 07] TIEMANN M., "Porous metal oxides as gas sensors", *Chemistry A European Journal*, vol. 13, pp. 8376–8388, 2007.

[TOR 09] TORTISSIER G., BLANC L., TETELIN A., *et al.*, "Mesoporous coated films on love wave acoustic devices for gas detection", *Sensor Letters*, vol. 7, no. 5, pp. 984–988, 2009.

[ZIM 01] ZIMMERMANN C., REBIÈRE D., DEJOUS C., *et al.*, "A love-wave gas sensor coated with functionalized polysiloxane for sensing organophosphorus compounds", *Sensors and Actuators B: Chemical*, vol. 76, nos. 1–3, pp. 86–94, 2001.

3

Immunosensing with Surface Acoustic Wave Sensors: Toward Highly Sensitive and Selective Improved Piezoelectric Biosensors

3.1. Introduction

A biosensor can be defined as an analytical device comprising two elements in spatial proximity: a biological recognition element, able to interact specifically with an analyte or a target, and a transducer which converts the recognition event into an electronic measurable signal. Many possible elements can be combined with a transducer to construct a biosensor. The possible range of analytes is almost limitless: from simple molecules to very complex molecules. They are limited only by the ingenuity of scientists to discover and match appropriate enzymes, bacteria, antibodies, cells, etc. New ones are discovered regularly. Mutations and genetic engineering open the possibilities of growing new strains or mutants which might have new applications [EGG 97]. Moreover, contrarily to conventional bioassays, biosensors allow the detection of molecular interactions as they take place, without requiring auxiliary procedures, making them highly attractive for biotechnological applications [ALT 08].

Biosensors concerned with monitoring solely antibody–antigen (Ab–Ag) interactions are termed immunosensors. These devices are based on the principles of conventional solid-phase immunoassays, such as enzyme

Chapter written by Najla FOURATI and Chouki ZERROUKI.

linked immunosorbent assay (ELISA), with either Ab (also called immunoglobulin, Ig) or Ag immobilized at the sensor surface.

An extensive range of analytes can be detected and measured by immunosensors, e.g. medical diagnostic markers, drugs, bacteria, cells, and environmental pollutants such as pesticides. However, the advantages of an absence of labeling requirements and the ability to investigate the reaction dynamics of Ab–Ag binding have given these devices the potential to revolutionize conventional immunoassay techniques [MOR 96]. Three main types of transducer have been used in immunosensor technology: electrochemical [HAS 13, HER 12, LI 12], optical [HAS 13, MAR 14, SHA 07] and piezoelectric [O'SU 99, PAN 12, VAU 03]. The first use of a piezoelectric immunosensor was proposed by Shons *et al*. in 1972 (a quartz crystal microbalance was modified for the determination of Ab activity in solution) [SHO 72]. Since this original publication, considerable research has been devoted to the development of piezoelectric immunosensors and today there are about 500 papers[1] in the literature describing various aspects of these devices.

Herein we present a brief review of recent advances not on piezoelectric immunosensors in general but on the most promising ones: the Surface Acoustic Wave (SAW) immunosensors. The first part is dedicated to a brief description of the principle of the most used SAW transducers and their common measurement instrumentation. In the second and the main part, a survey of clinical applications in the SAW immunosensing domain is presented.

3.2. SAW sensors and measurement systems

3.2.1. *SAW transducers*

SAW devices have been widely used as electronic components in mobile and wireless communications [CAM 98], for signal processing (filters, oscillators, resonators, delay lines, etc.). Their interest is the significantly small wavelength, compared to electromagnetic waves, for a given frequency, which permits a miniaturization leading to much more compact devices. The basic principle is related to the generation and the detection of

1 The exact number of references is 464. Result obtained using SciFinder for the terms "piezoelectric immunosenors"on May 16th 2014.

SAW using piezoelectric substrate materials. The most common ones are quartz, lithium tantalite, lithium niobate and langasite (Table 3.1). More recently, many works have focused on wide bandgap materials like Gallium Nitride (GaN) and more particularly Aluminum Nitride (AlN), which can be fabricated using micro-electromechanical systems (MEMS) technology with high integration density, to obtain thinner films, thus to reach higher frequencies (in the GHz range) [KAL 14, CAM 13, MUL 14].

Materials	*SAW speed (m/s)*	*Propagating mode*	*Coupling constant k^2 (%)*	*Temperature coefficient (ppm/°C)*
ST-X quartz	3158	Rayleigh	0.16	-0.035
26.6°Y-X $La_3Ga_5SiO_{14}$	2742	Leaky SAW	0.32	-0.078
36°Y-X $LiTaO_3$	4240	Leaky SAW	7.25	-35
41°Y-X $LiNbO_3$	4790	Leaky SAW	17.2	-52

Table 3.1. *Principal properties of common piezoelectric substrate materials*

Typical SAW devices consist of two sets of metallic interdigital transducers (IDTs), fabricated over the piezoelectric substrate using the lithography process (Figure 3.1). The IDTs with a comb-shaped structure serve for the input and output radio frequency (RF) signals. The input IDT converts the electric field energy into a mechanical wave (SAW) that spreads on the substrate surface to the output IDT where the mechanical energy is converted into electric field.

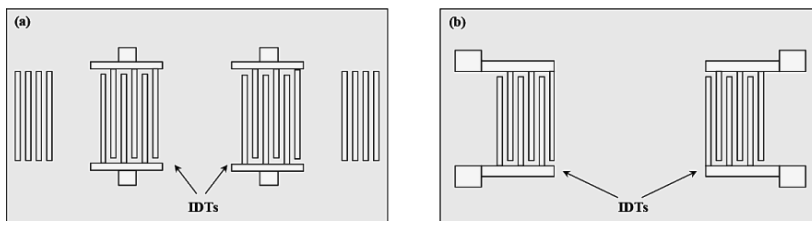

Figure 3.1. *a) Two-port SAW resonator; b) two-port SAW delay line*

The last 20 years have seen a surge of interest in using such devices for chemical and biological applications [JAK 11, POW 06, TSO 08, VOI 12]. The basic principle of SAW sensors is the detection of changes in

the propagation characteristics of the SAWs which are caused by perturbations on the active surface of the device. According to the device used and to the measurement mode, the physical, chemical or biological variations, occurring on the sensor's sensitive area, can be estimated from the output signal by measuring: (1) insertion loss and phase shift (delay line), (2) oscillation frequency (both resonator and delay line), (3) resonant frequency, quality factor and input impedance (resonator).

3.2.2. *Measurement instrumentation*

Besides using a network analyzer to measure amplitude and phase variations of the output electrical signal, two measuring systems can be used: oscillator and pulse mode.

In the case of SAW oscillator configuration, the basic principle depicted in Figure 3.2 is quite similar for both resonators and delay lines. Each delay line/resonator is inserted in the feedback loop of an oscillator where an automatic gain control amplifier that provides insertion loss compensation to satisfy Barkhausen conditions is included, and thereby maintains the oscillations of the device. The output signals of both the sensing and the reference SAW sensors (resonators or delay lines) are mixed, filtered (by a low-pass filter) and finally measured with a frequency meter.

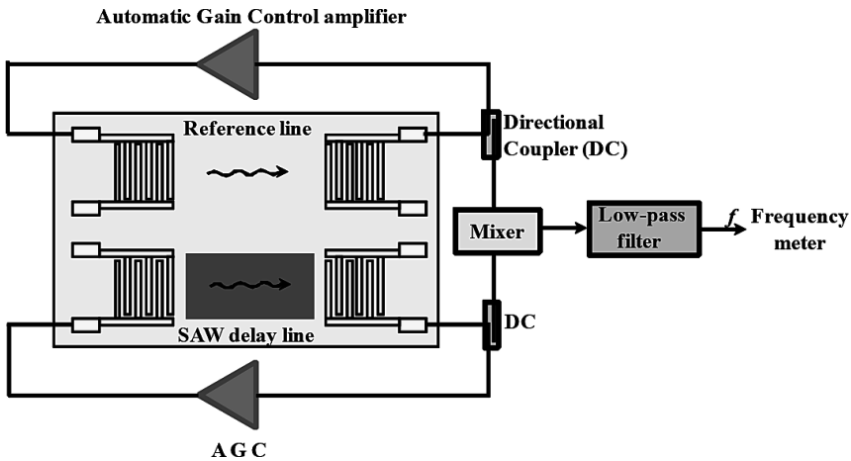

Figure 3.2. *Schematic representations of the measuring systems in oscillator mode*

Note that one of the difficulties that may be encountered in the case of SAW sensors concerns the existence of spurious signals (multiple reflections from the edges and/or the IDTs) that are difficult to remove without insertion loss. An example of edge reflection is presented in Figure 3.3. The most important is often the triple transit, resulting from successive reflections of acoustic waves, first by the output IDTs then by input IDTs. This signal is at the origin of the oscillations around the characteristic frequency. One possible solution consists of using a matching circuit with variable inductances and capacitances (in both the input and the output circuits) to minimize the amplitude of the triple transit. As the latter travels the sensitive area three times, it has a delay of 3τ (τ is the delay time corresponding to the direct path of the main wave). It is therefore possible to overcome this difficulty for delay line SAW sensors through a temporal filter, as is the case in a less used configuration: the impulse mode.

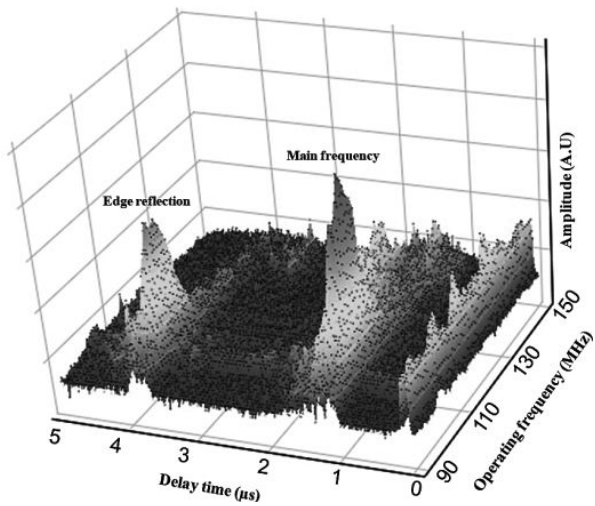

Figure 3.3. *Measurement of the SAW delay-line response, according to frequency at different delay time*

In the impulse mode system, the delay lines are inserted in two independent paths. The measured parameter is phase and/or amplitude variations of the sensing line according to the reference one (Figure 3.4). A high frequency (HF) generator carries out the input signal at the fundamental frequency, which is modulated, via an HF amplifier, by means of a rectangular pulse signal generator. Pulse trains' frequency and width vary

according to the device used. For a 100 MHz $LiTaO_3$ SAW sensor, the values often used are about 10 kHz and 1.8 µs for the frequency and the width respectively. The resulting signal is applied to the sensor input then the output signal is injected into a comparator to estimate its phase and amplitude variations, according to the original HF signal. A "boxcar integrator" synchronized on the pulse signal generator, makes it possible to select the useful signal (according to its delay) and to send it (averaged and integrated over fixed duration) into a digital analogical converter.

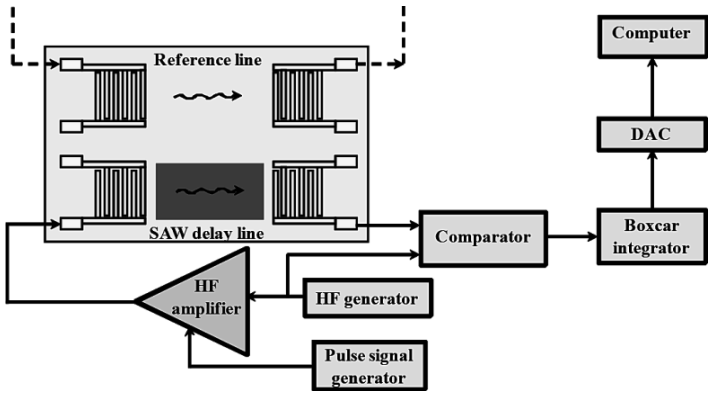

Figure 3.4. *Schematic diagram of the impulse mode system*

3.2.3. *An example of SAW device and conditioning system*

A variety of SAW sensors have been developed for numerous applications in liquid media. They differ in substrate material nature, design and architecture of the IDTs, the choice of the acoustic wave propagating mode, and of course on packaging and associated fluidic systems. The explicit and exhaustive presentation of these points is not the purpose of this review, that is why we limit ourselves to a brief description of systems we have developed and which do not significantly differ from those of other teams. Our system consists of non-labeled sensors based on a two-port SAW dual delay line fabricated on a 36 rot $LiTaO_3$ substrate. The IDTs (chromium/gold: 20 /80 nm) were photolithographically patterned with a periodicity of λ = 40 µm which corresponds to an operating frequency of about 104 MHz. Each electrode consists of 30 double finger pairs, thus minimizing triple transit interferences. The sensing area, the region between the input and output IDTs, were metallized with 20/80 nm Cr/Au thin layer,

to favor leaky SAW (LSAW) propagation instead of surface skimming bulk waves (SSBW) [HAS 00, HAR 97a]. The acoustic energy is thus confined close to surface substrate, making the sensor highly sensitive to any perturbation occurring in the propagating medium. Gold metallization also makes it possible to provide a suitable surface for molecule grafting and to make devices less sensitive to ionic strength variations. A Kalrez® cell is placed over the sensing area to contain solutions and to ensure interdigitated transducers' insulation (Figure 3.5). Kalrez® was chosen among other materials for its biocompatibility and mainly for its "nature" since it does not stick to the sensing area, like PDMS, and does not need an additional joint like PMMA. Moreover, it causes only 5 dB additional attenuation of the surface wave at the fundamental frequency of 104 MHz. A PMMA sill including inlets and outlets is then added. Experiments were driven using a peristaltic pump (Gilson Minipuls 3) to ensure continuous fluids flow at a rate of 190 µL/min (Figure 3.5).

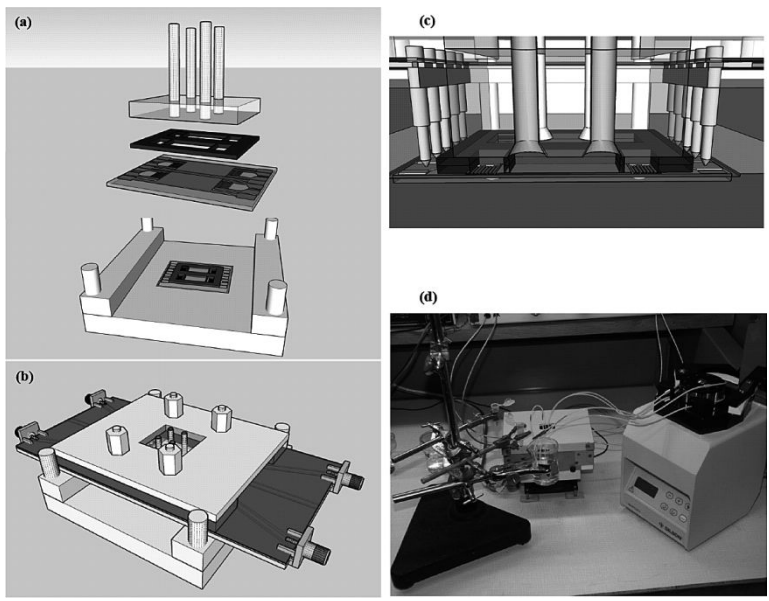

Figure 3.5. *a)–c) Schematic representations of the various parts of the conditioning systems. a) The metallic base, SAW dual delay line sensor and fluidic cell; b) overview of the system assembly with printed circuit board to access the electrical contacts and the mechanical protection box; c) sectional view showing the pine electric contact and tips of the fluidic system with flared ends; d) overview of the system assembly and the fluidic circuit with peristaltic pump*

3.2.4. *SAW immunosensors' potential and their possible improvement*

The merits of SAW immunosensors are clearly related to the affinity, specificity and selectivity of the Ags/Abs binding reactions. It should be first clarified that the specificity for the measurement of analytes in all immunosensor systems is dependent on the application of binding molecules. New developments in protein engineering for immunoglobulins (Ab fragments, chimeric antibodies, etc.) or in substituting antibodies by alternative binding components, like aptamers, or structures (molecular imprinting) will, therefore, be applicable to this technology [LUP 01].

A SAW immunosensor can use either a single or multi-step binding(s) to the crystal surface. A single step measures the binding of one component to the modified crystal surface, while multistep methods rely on the sequential binding of two or more components [YAN 00].

3.2.4.1. *Antigen–antibody (Ag–Ab) selective recognition*

Many immunosensors are built on the basis of biotin/streptavidin (or streptavidin /anti streptavidin) affinity. To obtain an Ab/Ag sensor we also benefit from this affinity model [BER 11]. Various successive steps have been carried out on the sensing area of the gold metalized delay line. The first step consisted of the grafting of biotinylated self-assembled monolayer. In the second step, bovine serum albumin (BSA) was drained into the flow cell, to block free spaces between biotin molecules. In the third step, streptavidin (antibody) was injected in the flow cell. Finally, we used an anti-streptavidin (antigen) produced in rabbits as a specific Ag to test the Ag/Ab recognition, and an IgG sheep as a non-specific one for the sensor's selectivity test. Of course, and even if not mentioned, each step must be followed by washing steps (ultra pure water and phosphate buffered saline mainly). The choice of multiple steps has been motivated by checking the SAW sensor's response in terms of sensitivity and saturation when the investigated changes occur relatively far from SAW sensor's surface, where the acoustic energy is confined. Moreover, we equally tested the HRP–streptavidin (horseradish peroxidase conjugated streptavidin) to highlight an eventual effect of steric hindrance. All these steps were monitored via phase variation versus time, using the impulse mode system. Each recognition reaction leads to a specific phase shift amplitude and

kinetic, except for IgG sheep where no changes were observed on the sensor's response as expected. These experiments show that the various steps in the presence of macromolecules had an effect on Ag concentration saturation values and on recognition reaction kinetics, but not on sensitivity.

Weiss *et al*. have built an immunosensor with 20 multilayers without a sensitivity loss, showing the robustness of such SAW devices [WEI 98]. But neither our experiment, nor that of Weiss has to be generalized. Indeed, when the acoustic wave propagates in a semi-infinite medium, it remains confined to the surface, with a penetration depth of fraction of its wavelength [NAR 12]. This means that for GHz frequencies, the correspondent wavelengths become smaller, which can affect the sensor's response toward phenomena occurring "far" from the surface.

3.2.4.2. *Experimental estimation of kinetic rates*

Dual configurations, presented in section 3.2.2, are generally used when performing immunosensing gravimetric measurements. In this case one SAW sensor is used as a reference, while the second SAW sensor is exposed to the test sample containing the corresponding Ag or Ab. Ag/Ab recognition will lead to a decrease of phase or frequency values depending on the electronic system used.

Another interest of SAW immunosensors is their capacity to follow up in real-time Ag/Ab recognition reactions, thus allowing us to determine the kinetics of the immunocomplex formation. In fact, the reaction between the immobilized compound and the molecule in solution can often be represented by the following equation [3.1]:

$$Ag + Ab \rightleftarrows AgAb \qquad [3.1]$$

For this so-called solid-phase technique, two different approaches can be used: determining the equilibrium constants or the binding rates.

The equilibrium constants k_a (association) and K_d (dissociation) are often obtained from equilibrium experiments, while the binding rates k_{on} and k_{off} are obtained from kinetic experiments according to equation [3.2]:

$$\frac{d\left[AgAb\right]}{d\,t} = k_{on}\left[Ag\right]\left[Ab\right] - k_{off}\left[AgAb\right] \qquad [3.2]$$

$[C_x]$ is the concentration of the species C_x.

Recording of the phase/frequency shifts versus time, during the Ag/Ab recognition for solutions of known concentrations, permits the extraction of k_{on} and k_{off} binding constants. Thus, equation [3.2] becomes:

$$\frac{dX}{d\,t} = k_{on}\left[Ab\right]\left(X_{max} - X\right) - k_{off}\left(X\right) \qquad [3.3]$$

where X is the acoustic phase variation (impulse mode) or the frequency shift (oscillator configuration); $[Ab]$ is the Ab concentration; k_{on} and k_{off} are the association and dissociation rates.

Using numerical approach, equation [3.3] becomes:

$$\frac{\Delta\left(dX/dt\right)}{\Delta X} = k_{on}\left[Ab\right] + k_{off} \qquad [3.4]$$

This equation permits an experimental estimation of the constants k_{on} and k_{off} from the values of phase/frequency shift corresponding to the sensor's linear domain, then the equilibrium constant k_{eq} ($k_{eq} = k_{on}/k_{off}$) [BER 11].

3.2.4.3. *SAW sensor's improvements*

To improve the SAW sensor's sensitivity, there are two preferred methods: (1) the confinement of acoustic energy near the sensor's surface, where the changes to be monitored occur; (2) an increase in the fundamental frequency. Since the theoretical work of Love [LOV 67], on the effect of additional layer to SAW sensor upon shear wave confinement, and the first demonstration of feasibility by Gizeli [GIZ 92], many Love-based devices have been developed. The wave confinement makes the sensor more sensitive to changes over its surface, which permits investigations requiring enhanced sensitivity. If the polymers present a great potential, due to their low shear velocity, when used as guiding layer materials, they do however suffer from their high acoustic loss. This explains the continuous

investigations on suitable materials presenting the better compromise between these two properties besides the most used one: SiO_2. Multilayered structures, as well as piezoelectric layers such as ZnO, seem to be promising candidates for a guiding layer in Love SAW sensors [POW 06].

The simplified form of equation [3.5] highlights the evidence of frequency dependence of a SAW sensor's sensitivity:

$$\Delta f / f_0 = -C \times f_0 \times \Delta m / S \qquad [3.5]$$

where Δf represents the frequency shift and $\Delta m/S$ is the mass load on the sensors per area.

f_0 is the fundamental frequency and C is a proportionality parameter where all constants involved in the sensing processes are held, depending on the piezoelectric substrate.

As the sensor's sensitivity increases by increasing the frequency up to the GHz domain, the enhancement can be sufficient for common applications. Lee *et al*. have observed that sensitivity of SAW sensors was approximately 2 times higher in the case of 400 MHz than for 200 MHz frequency [LEE 11].

The possibility of combining an appropriate guiding layer and high operating frequency (in the GHz range) allowed us to envisage reaching a sufficiently high sensitivity for a large variety of applications.

3.3. Immunosensing applications to evaluate SAW device performances

Most studies concerning immuno-SAW devices did not aim at highly sophisticated surface modification methods, but only to demonstrate the performance of the particular SAW system, mainly in terms of mass sensitivity (S) and detection limit (DL) values. A chronological review of these sensing devices is presented in Table. 3.2. All washing steps are deliberately not mentioned.

Immuno species	*SAW device*	*Main results*	*Ref*
Human IgG /Anti human IgG	– Love plate device: 42.5°Y-cut quartz coated with a 1.23 µm thick PMMA layer. – f = 110 MHz. – Phase variations measured with a 4195A network analyzer.	– *First Love wave immunosensor* – IgG/polymer interaction based on spontaneous adsorption without chemical activation of PMMA surface. – Linear relationship between concentration and phase change for low IgG concentrations. – Phase change approaches a saturation level for IgG concentrations > 0.3 mg/ml.	[GIZ 92]
Rabbit anti-goat IgG/Goat anti human IgG	– SH-SAW in 36 rot propagating $LiTaO_3$ substrate. – Dual delay line configuration with a frequency of 115 MHz. – Phase variations measured with a HP8752A network analyzer. – Used for measurements at the third harmonic of 345 MHz.	– After surface functionalization: (1) incubation of protein A during 1 h on the sensor surface, (2) incubation of the Ab solution for 1 h, (3) exposure to BSA during 30 mn to reduce nonspecific interactions. – Theoretical DL ≈33 pg. – S = 110 kHz/(ng/mm^2). – High signal enhancement factors of 4.5 and 12 achievable by gold colloid labeled antigens with colloid diameters of 5 and 10 nm, respectively. – Specificity of the antibody demonstrated by a pre-absorption experiment.	[WEL 96]
– Human IgG – Anti-atrazine IgG (ESL)/Atrazine	– Love plate device: 42.5°Y-cut quartz coated with either PMMA or amorphous silica. – f = 110 MHz. – Phase variations measured with a 4195A network analyzer.	– Aim of the work: study of properties effects of over layers used for guiding Love wave. – IgG adsorption: – dilution of human IgG in PBS buffer (pH 7.3), – contact with the device surface during 10 min, – injection of the protein solution which is kept at room temperature. – Anti-atrazine adsorption: activation of the gold surface with 50 µg ml^{-1} protein A in PBS buffer at room temperature for 1 h, – injection in the flow cell of 250 µg ml^{-1} of anti-atrazine IgG (ESL). – Linear relationship between concentration and phase change for low IgG concentrations. – Phase change approaches a saturation level for IgG high concentrations. – Sensitivity S of the 1.6 µm PMMA coated SAW device = 430 g cm^{-2}.	[GIZ 97]

		– Phase shift corresponding to the binding of 250 µg ml^{-1} of anti-atrazine ≈ 4. – Phase shift corresponding to the binding of 400 ppb atrazine ≈ 0.4.	
Polyclonal sheep immunoglobulin G (IgG)/ Anti-sheep IgG	– Love wave sensor fabricated on an ST-cut quartz substrate. – Guiding layer: 5.6 µm thick SiO_2 layer. – f = 110 MHz – Dual delay-line oscillators.	– Mass sensitivity (in air): S = 380 cm^2 g^{-1} (or 41 Hz ng^{-1} cm^{-2}). – Immobilization of IgG receptor via the salinization of the SiO_2 layer. – Surface functionalization: coverage of sensing and reference channels for 1 h with a droplet (≈ 15 µl) of concentrated IgG solution. – Sheep IgG immobilization ⇨ frequency change between 16 and 18 kHz ⇨ surface masse density between 390 and 440 ng cm^{-2}. – Rabbit IgG immobilization ⇨ frequency change of ≈ 11 kHz ⇨ surface masse density ≈ 270 ng cm^{-2}. – Non-specific responses usually in the range of 5–10% of the specific responses.	[HAR 97b]
3 types of matching polyclonal antibodies: (1) AffiniPure rabbit anti-sheep IgG H+L, (2) AffiniPure sheep anti-mouse IgG H+Land AffiniPure mouse anti-rabbit H+L	– SH-SAW in 36 rot propagating $LiTaO_3$ substrate. – Dual delay line configuration with a fundamental frequency of 115.3 MHz. – Phase variations measured with a HP 8752A network analyzer. – Used for measurements at the third harmonic of about 348 MHz.	– Surface functionalization: (1) a droplet of PBS solution is put onto the sensitive path,(2) a droplet of concentrated antibody solution is added, (3) another droplet of PBS is put onto the sensitive path, (4) addition of a droplet of antibodies solution that matches the binding site of the antibodies immobilized at the surface in the previous step ⇨ Possibility to build a stack of about 20 layers of antibodies. – Cross-linked antibodies build up a structure resembling a very soft polymer film, where a Love-like mode is trapped after reaching a certain thickness. – The values found for the elastic coefficients (1 MPa) compare well with those for very rubbery polymers.	[WEI 98]
Anti-glucose oxydase/Glucose oxydase	– SAW-sensors low-loss filters on a 36 rot. $LiTaO_3$ X (Murata, Japan).	– 210 kHz after rinsing with the antigen for sensors protected with polyimide, functionalized by CNBr and coated with activated antibodies.	[WES 99]

	– Devices placed in a TO 18 chamber and built in a teflon adapter which connect the sensor to the fluidic system. – Measurements made in an oscillator circuit.	– If sensors are first pre-treated with BSA⇨ a frequency shift of ≈100 kHz representing the part of the unspecific binding of protein to the antibody layer. – Sensitivity S = 51 Hz/pg.	
Rabbit anti mouse IgG/Goat anti rabbit IgG	– A combination of SiO_2 protective layer on $LiTaO_3$ substrate and an inductively coupled SAW device. – A primary coil is connected to the RF circuitry while the second one is formed by the IDTs and their interconnections. – Phase and amplitude detected using a HP 8752 network analyser.	– Surface functionalization: (1) incubation of protein A during 1 h on the sensor surface, (2) incubation of the Ab solution for 1 h, (3) exposure to goat anti rabbit IgG. – Follow up of Ab/Ag recognition. – Substantial decrease of signal attenuation in the device resulting in an insertion loss of about 30–35 dB.	[FRE 01]
Anti-FTIC/FTIC	– ST-Quartz resonator – $f \approx$ 250 MHz. – SAW resonators with various coatings mounted in TO-8 packages, inserted into the sensor head module and subjected to various fluorescent analyte gases. – Device connected into an oscillator circuit.	– Construction of a vapor phase biosensor by immobilizing a monolayer of antibodies onto the surface of a SAW device. – Surface functionalization: (1) dissolution of protein A in a buffer solution at physiological pH, (2) addition of anti-FITC antibody to the buffered protein, (3) placement of the mixture in a refrigerator for 2 h, (4) coating the gold surface with 3 µl of the cross-linker–antibody solution, (5) application of a thin layer of hydrogel (3 ml) by spinning for 30 s at 3,000 rpm. – S = 3 Hz/pg. – DL ≈ a few pictograms. – Selectivity tests made with nitrogen gas.	[STU 02]

Protein A/ Monoclonal antibodies of anti-E3G	– 3 types of substrate: (1) $LiTaO_3$ substrate operating at 104 MHz, (2) quartz substrate operating at 108 MHz and (3) quartz substrate operating at 155 MHz – Love wave devices: substrates coated with a Novolac photoresist polymer layer. – Phase variations measured with a HP 4195ANetwork analyser for Quartz 108 MHz device – Phase variations measured with a 8753ES Network Analyser for Quartz 155 MHz and $LiTaO_3$ 104 MHz.	– Aim of the work: study of the effect of operating frequency, piezoelectric substrate and waveguide layer thickness on the sensitivity of the acoustic waveguide sensor during the specific binding of an antibody by a protein. – Surface functionalization: (1) placement of freshly prepared gold-surface in the device holder and exposure to PBS buffer for approximately 1 h, (2) contact between protein A and the device surface for 30 min, (3) addition of different solutions of monoclonal antibodies of anti-E3G at a concentration range of 0.7–667 nM in PBS. – Follow up of phase changes of the devices during the binding of IgG to the protein A. – Sensitivities ratios: $S(Q_{155\ MHz}) / S(Q_{108\ MHZ}) = 1.3$, $(Q_{108\ MHz}) / S(LT_{104\ MHZ}) = 1.1$.	[GIZ 03]
Anti-urease/ urease	– Resonator filters based on HPSSW designed in cooperation with Siemens and then purchased as E062 from Epcos. – 36°YX $LiTaO_3$ as substrate material. – Operating frequency of 433.9 MHz. – Measurements done in an oscillator circuit.	– Surface functionalization: (1) deposition of 0.1 µm of parylene C via chemical vapor deposition at low pressure and room temperature, (2) incubation of SAW devices coated with a solution of 0.1 mg/mL of OptoDex-A in PBS, (3) surface activation, – immobilization of anti-urease. – Unspecific interactions observed by incubating the surface with 4 mg/mL BSA. – Incubation with urease ⇨ a linear decrease for several minutes (slope = -12.62 Hz/s). – End of the measurement ⇨ a drift of +0.27 Hz/s.	[LAN 03]

	– Design of 3 flow cells. The corresponding volumes are 50 µl, 4.8 µl and 60 nl.	– Reduction of the flow cell volumes ⇨ reduction of measurement duration from more than 0.5 h (flow cell volume 50 µL) down to a few minutes (flow cell volumes 4.8 µL and 60 nL). – Time reduction from the 4.8 µL cell to the 60 nL one not significant probably due to the valves and the tubing length of the remaining fluidic.	
Human IgG(hIgG)	– A combined SPR/SAW technique. – ST-cut quartz substrate patterned with double-finger IDTs for launching a Love mode acoustic wave at a frequency of 123.5 MHz. – Guiding layer: 1.13 µm thick PECVD silicon dioxide layer. – Phase and insertion loss monitored using a HP 4396A network analyzer.	– Investigation of several techniques: QCM-D, AFM, SAW device and SPR. – Difference in kinetic trend between SPR/SAW measurements and QCM-D. – QCM and SAW techniques measure the combined mass uptake coming from both the adsorbed protein and trapped water in the protein layer, whereas optical or labeling techniques does not include the mass of trapped water. – Most of the trapped water is getting expelled from the films upon durable contact with the solid support because of the hydrophobic interaction between the protein macromolecules and the hydrophobic surface. – Conformation changes occurring upon contact with hydrophobic support ⇨ the effective protein film thickness from combined SPR/SAW measurements is smaller than the extended state molecular dimension of the IgG molecule.	[ZHO 04]
C60-hemoglobin (C60-Hb)/anti-hemoglobin (anti-Hb) antibody C60-myoglobin (C60-Mb)/ anti-myoglobin (anti-Mb) antibody	$LiTaO_3$ SAW sensor working at 145 MHz.	– Surface functionalization: (1) coating of the crystal with fullerene C60, (2) insertion of the C60 coated crystal into a biospecies solution. – Linear frequency responses to the concentrations of anti-Hb and anti-Mb antibodies with sensitivities of 0.14 and 1.27 kHz/(µg/mL). – Detection limits of 0.32 and 0.035 µg/mL for anti-Hb and anti-Mb antibodies respectively. – Optimum pH = 7.3. – Optimum temperature = 27°C. – No interference of common bio-species in human blood, e.g. urea, ascorbic acid, tyrosine, and metal ions to the SAW immunosensors coated with C60-Hb.	[CHA 07]

C60-hemoglobin (C60-Hb)/ Anti-hemoglobin (anti-Hb) antibody C60-myoglobin (C60-Mb)/ Anti-myoglobin (anti-Mb) antibody	– Investigation of two types of piezoelectric immunosensors: QCM (10 MHz) and $LiTaO_3$ SH-SAW (145 MHz). – SAW immunosensor system, obtained from F-Tech. Co (Taiwan) contains delay-line type SAW oscillators, oscillator circuit, peristaltic pump, a constant temperature chamber and a personal computer.	*– The same results as the previous study for $LiTaO_3$ sensors.* – Development of an electrochemical surface acoustic wave sensor (ESAW): two parallel square-plate electrodes welded with long-distance wires and coaxial cables used to contact to the metal shell of the 315 MHz SAW/quartz resonator. – Selective detection with the ESAW of glucose in solutions. – ESAW detection system exhibited a linear frequency response to the log concentration of glucose with a slope of $\approx 9.3 \times 10^2$ Hz decade^{-1}. – DL of glucose is below 10^{-3} M (glucose concentration in biological samples such as blood is within 10^{-2}– 10^{-3} M).	[CHO 08] The same team as [CHA 07]
Protein capture (Goat anti-rabbit antibody)	– $LiTaO_3$ SH-SAW sensors operating at 260 MHz. – Spin-on glass as a coating of the device surface. – Measurements performed using a HP 8752C network analyzer. – No differential measurements.	– Thin films of spin-on glass considerably enhance the sensitivity of the SAW device – First use of polymers based on polyvinylamines for immobilization of the capture protein. – New antibody immobilization technique ⇨ avoid of non-specific binding of foreign materials at the sensor surface + possibility to do measurements in whole blood. – Minimum detectable antibody concentration of 4 µg/ml compares favourably with that of established systems. – Reliable results for diagnosis available already after 20 min.	[RUP 08]
Biotin/ HRP–Streptavidin	– $LiTaO_3$ SH-SAW sensors operating at 104 MHz. – Pulse excitation technique to monitor amplitude and phase changes.	– Surface functionalization: (1) grafting of a mixed self-assembled (SAM) monolayer formed by biotinyl-PE and 16-mercaptohexadecanoicacid, (2) blockage of free spaces between biotin molecules with BSA. – Mass sensitivity in glycerol: $S_1 = 2.20 \pm 0.60/(ng/mm^2)$. – $\Delta\Phi = 15$ during SAM formation. – Mass sensitivity corresponding to SAM formation: $S_2 = 6.90 \pm 0.70/(ng/mm^2)$.	[BER 09]

		– $\Delta\Phi = 3°$ after BSA Blockage. – $\Delta\Phi = 4$ after streptavidin–biotin recognition. – Mass sensitivity S_3 related to BSA blocking and biotin streptavidin bound: $S_3 = 0.03 \pm 0.01/(ng/mm^2)$.	
Antigenitic HA Peptide/Murine anti HA antibody Antigenitic FLAG peptide/Murine anti FLAG antibody	– Love wave devices: AT-cut quartz substrate covered by a ≈ 4 µm thick SiO_2 guiding layer deposited by PECVD. –$f \approx 116$ MHz.	– Surface functionalization: (1) functionalization of the guiding layer by a semi carbazide based silane, (2) dipping of the silane functionalized transducers in a solution of tert-butylcarbazate (Boc-NH-NH2) with absolute ethanol used as catalyst for 1 h at r.t., (3) unmasking of the semi carbazide groups to get reactive functions for peptide immobilization. – Validation of peptide reactivity by AFM and fluorescence microscopy – Total mouse IgG antibody used as a negative control. – Recorded frequency shifts: $\Delta F = 4000 \pm 30$ Hz (n = 2) for FLAG/anti-FLAG and $\Delta F = 1300 \pm 30$ Hz (n = 2) for and HA/anti-HA. – Calibration curve of murine anti-HA: $y = -2.53x + 60.7$, $R^2 = 0.993$. – $S = 10^6$ Hz L g^{-1}. – LD = 3 pg/mm^2.	[FER 09]
Neutravidin /biotinylated-BSA (b-BSA)	– µF-on-SAW: a chip with 2 sensor elements +4 channel microfluidic module. – Love wave devices: quartz coated with a thin PMMA layer (few hundreds of nm thick). – Phase variations measured with a HP8753ES Network analyser.	– Aim of the study: realization of a multi-channel microfluidic module on SAW sensor chips (µF-on-SAW) to achieve multi-analyte detection. – Monitoring of 2 types of interactions: (1) physical adsorption of neutravidin on sensor gold surface, and (2) subsequent specific binding of b-BSA. – High reproducibility of the sensitivity among sub-areas of the array (92%).	[MIT 09]
Anti-HSA antibody/HSA antigen	– Quartz SH-SAW delay line operating at 250 MHz and	– Surface functionalization: (1) modification of the sensor surface with probe proteins,	[KOG 10]

	$LiTaO_3$ SH-SAW sensor operating at 206 MHz. – Transmitting and receiving floating electrode unidirectional transducer (FEUDT). – Cavities above the IDTs composed of SU8 walls built by photolithography technique.	(2) immobilization of antibodies onto the linker layer. – Velocity and attenuation changes of the quartz-based devices higher than those of the $LiTaO_3$-based devices. – Data of calibration curve of quartz immunosensor fitted using a nonlinear least-squares method.	
Anti-H IgG/H IgG)	– Love-mode immunosensors based on structures of ZnO/36 YX-$LiTaO_3$ – Growth of ZnO films on the 36 YX-$LiTaO_3$ substrates by RF magnetron sputtering technique. – Deposition of a gold layer on ZnO to immobilize antibodies. – For comparison, SiO_2/36 YX-$LiTaO_3$ structures are fabricated by the deposition of SiO_2 layers on 36 YX-$LiTaO_3$.	– Surface functionalization: (1) exposure of the gold surface to protein A for 1 h at 32°C, (2) incubation of the surface in the concentrated anti-H IgG solution for 2 h at 32°C, (3) blocking nonspecific binding sites with BSA solution in PBS for 1 h. – Realization of several Love-mode sensors (ZnO/36 YX-$LiTaO_3$ and SiO_2/36 YX-$LiTaO_3$) to evaluate mass sensitivities of the sensors. – Antibody–antigen immunoreactions carried out at the same conditions. – Optimal thickness of ZnO = 1.2 μm – ZnO optimized thickness < SiO_2 overlayer (6 μm). – Sensors with ZnO guiding layers have higher sensitivities than those with conventional SiO_2 overlayers.	[ZHO 10]
Streptavidin/ Antistreptavidin HRP-Streptavidin/ Antistreptavidin	– $LiTaO_3$ SH-SAW sensors operating at 104 MHz. – Pulse excitation technique and HP 8711C network analyser to monitor amplitude and phase changes.	– Surface functionalization: (1) grafting of a mixed self-assembled (SAM) monolayer formed by biotinyl-PE and 16-mercapto hexadecanoic acid, (2) blockage of free spaces between biotin molecules with BSA, (3) streptavidin (or HRP streptavidin) grafting. – Linear phase variations of phase versus streptavidin concentration up to 10 nM ⇨ S = 0.25/nM.	[BER 11]

		– Decrease of concentration saturation values from 23 ± 2 nM for streptavidin to 10 ± 2 nM (for HRP–streptavidin). – HRP causes a steric effect ⇨ reduction of kinetic constant k_{eq} from 6.7×10^8 M^{-1} (for streptavidin) to 2.2×10^8 M^{-1} (for HRP–streptavidin).	
A9H12/LAG-3	– Love wave device: delay lines built on an AT quartz coated with a 2.5 µm thick silica layer. – f = 125 MHz. – The low frequency vibrating mixer is an acoustic transducer consisting of an active piezoelectric element and a silicon structure.	– Aim of the study: impact of local acoustic mixing to promote or accelerate antibody grafting on activated surfaces. – Surface functionalization: (1) SAM grafting on the SAW sensor of mPEG thiol and PEG thiol acids, (2) activation with NHS/EDC, (3) covalent immobilization of A9H12 antibody. – Mixing increases Ab transfer to the sensing area: phase variation of about 8.2 ± 0.3 in the acoustically activated mode versus 3.3 ± 0.3 in the passive mode ⇨ Increase of the surface coverage by about 2.5 (in accordance with SPR results). – In the absence of acoustic energy, biological particles are driven to the biochip surface by diffusion. – In the acoustically activated case, particle drift is due to the combination of the induced displacement force and the natural diffusion except in the vicinity of the biochip where the diffusion is dominant. – For Ab/Ag reaction: $\Delta\Phi = 3.6 \pm 0.3$ without acoustic mixing, $\Delta\Phi = 4.5 \pm 0.3$ with acoustic mixing ⇨ improvement of the captured Ag density of ≈ 20%.	[KAR 11]

Table 3.2. *Survey of Immunosensing applications to evaluate SAW devices performances*

3.4. Survey of clinical applications of SAW immunosensor systems

Applications dealing with “real” clinical samples are still rare. Most of the papers describing the use of immunosensors in this field only have an exemplary character, as presented in section 3.3.

3.4.1. *Cardiac biomarker detection*

According to the World Health Organization (WHO), cardiovascular disease (CVD) is a major cause of human death in both developing and developed countries. Its early and quick diagnosis is thus extremely important and crucial. Existing methods of diagnosis for CVD are based on tests conducted in central laboratories that may take several hours or even days from when tests are ordered to when results are received. The elaboration of biosensors, which can (1) help in rapid diagnosis, (2) provide better health care, and (3) reduce the waiting time for results dissemination (highly stressful to the patients), is probably one of the most promising solutions. There has been considerable interest in finding diagnostic and prognostic biomarkers that can be detected in blood and predict CVD risk. Of these, C-reactive protein (CRP) is the best known biomarker followed by cardiac troponin I or T (cTnI/T), myoglobin, lipoprotein-associated phospholipase A(2), interlukin-6 (IL-6), interlukin-1 (IL-1), low-density lipoprotein (LDL), myeloperoxidase (MPO) tumor necrosis factor alpha (TNF-α) and creatine kinase (CK)-MB [QUR 12].

Publications concerning the development of SAW biosensors to detect cardiac markers are rather recent. The earliest reference on this subject was published in 2008, as presented in Table 3.4.

SAW device	Main results	Ref
– A Love mode SAW biosensor: ZnO thin films grown on 500 Å thick SiO_2 layer that was grown on a (1, 0, 0) Si substrate. – ZnO film is the guiding layer of the acoustic wave and SiO_2 film is the substrate. – Operating frequencies: 747.7 MHz and 1.586 GHz.	– Biosensor devices used to measure the IL-6 protein mass and study the effectiveness of the IL-6 protein attachment processes. – 3 attachment processes: (1) direct surface adsorption of the IL-6 antibody onto the ZnO sensor window surface followed by the subsequent bound of IL-6 protein, (2) surface activation by hydroxylation followed by silanization and IL-6 immobilization through bovine serum albumin (BSA), (3) surface activation and IL-6 immobilization through the monoclonal antibody. – Active area of the biosensor: two different size square windows where the proteins are attached. – Comparison between surface adsorption and surface immobilization through BSA and antibody, showed that the surface adsorption is not an effective approach to antibody–protein attachment and detection.	[KRI 08]

	– Extended linearity for higher sensor frequency and for the immobilization process through the monoclonal antibody. – Preliminary measurements with the biosensor prototype successfully detected low levels of IL-6 protein in human serum.	
– A Love wave device operating at 200 MHz. – 36 rot $LiTaO_3$ substrate coated with 5.2 µm-thick SiO_2 guiding layer. – A laboratory-built oscillator circuit. – Fluids in the cartridge controlled pneumatically by 2 external peristaltic pumps and 8 three-way solenoid valves positioned in a valve plate. – Each fluidic sequence was carried out automatically with a circuit board by transmitting control signal to the pumps and the valves.	– Human plasma containing cardiac markers was mixed with AuNPs, which had been conjugated in advance with the detection antibodies for troponin I, CK-MB, and myoglobin. – Cardiac markers were allowed to bind to their corresponding antibodies on AuNPs. Then, the solution was applied to the sensor surface, on which capture antibodies of each cardiac marker had been immobilized, and immunoreaction proceeded. – Fluidic steps: (1) spiking troponin I, CK-MB, and myoglobin, (2) load of the whole human blood into the cartridge, (3) application of air pressure onto the blood (4) filtration of blood plasma through the porous membrane (5) transported to the plasma reservoir (6) detection of antibody-AuNP conjugates (7) passage through the mixer and incubation on the SAW sensor surface for sandwich immunoreaction. – Frequency follow up during all these steps.	[CHO 11]
– A Love mode dual delay line SAW biosensor on 36_YX-$LiTaO_3$ substrate. – 5.2 µm thick SiO_2 as guiding laye for operating frequency at 200 MHz. – 2.6 µm thick SiO_2 as guiding layer for operating frequency at 400 MHz.	– A fully automated system with SAW immunosensor was developed for detection of cardiac biomarker: troponin I (cTnI). – Monoclonal anti-cTnIs were immobilized on the detection areas of the SAW sensors. – Mixing Plasma containing cTnI with gold conjugated nanoparticles–antibody (cTnI) before injection on the sensor where anti-cTnIs were immobilized. – The high sensitive AuNP-based sandwich immunoassay, presented a limit of detection of 6.7 pg mL^{-1}, far below the clinical cut-off level of cTnI (0.06–1.5 ng mL^{-1}). – "The first" example of a centrifugal micro fluidic point-of-care testing system that fulfills requirements of the early diagnosis of acute myocardial infractions.	The same team: [LEE 11], [LEE 13a], [LEE 13b]

Table 3.3. *Survey of cardiac markers using SAW immunosensors*

3.4.2. *Bacterial detection*

Dissemination of harmful bacteria in food or water supplies as a result of accidents, pollution or terrorist activity can produce serious consequences in the form of economic losses and human suffering [BER 06]. An important aspect of disease control is the detection of organisms responsible for causing an outbreak. There are several methods currently available which include either conventional approaches (plating and culturing, enumeration methods, biochemical testing, microscopy and flow cytometry) or new methods (immunological techniques, DNA microarrays and mass spectrometry). However, many of these methods are time-consuming (plating and culturing), expensive (mass spectrometry, DNA microarrays), or will give total bacterial load rather than just the number of viable cells (ELISA) [DEI 04]. SAW immunosensors are thus a real alternative to these techniques, mainly due to their sensitivity, selectivity and fast response times.

SAW immunosensors have been investigated to detect two types of bacteria: *Bacillus anthracis* simulant [BRA 04] and *Escherichia coli* O157:H7, a microorganism which has been linked to a wide spectrum of clinical manifestations, including asymptomatic carriage, non-bloody diarrhea, hemorrhagic colitis, the hemolytic-uremic syndrome, and thrombotic thrombocytopenic purpura [SU 95]. Main results concerning *E. coli* detection using SAW biosensors are gathered in Table 3.4.

3.4.3. *Cell detection*

One way to study cell signaling is to bring cells into contact with the biosensing surface, which could be achieved by cell culture. Note that, because of the large dimension of cells, compared to the short penetration depth of a biosensor, only their bottom portion is generally sensed [VEL 09]. Only a few studies are concerned with cell detection with SAW immunosensors.

Bröker *et al.* have realized a nanostructured chip which enables the binding of cancer cells and detection of extremely low numbers of circulating tumor cells (CTC). For this purpose they have used a sam® 5

biosensor[2] which showed significant responses to less than 10 cells injected in a single run. Besides its selectivity, the highly robust nanostructured chip has an easily regenerable surface permitting successive detection of cells [BRO 12].

SAW device	*Main results*	*Ref*
– Love plate device: ST quartz coated with a 5 µm thick sputtered SiO_2 layer. – f = 110 MHz. – Dual channel configuration. – Measurement of frequency variations.	– Simultaneous detection of two different microorganisms: *Legionella* and *Escherichia coli*. – Use of 4 novel protocols to detect bacteria by coating them onto the surface of the SAW followed by binding to specific antibody. – If the bacteria are coated onto the surface in a droplet⇨ Sensitivity of bacteria detection not increased by using a silanized SAW. – If *E. coli* is delivered into one side of a dual tank in 0.5 ml of liquid ⇨ Greatest sensitivity of detection: 4×10^5 cells/ml achieved with a silanized SAW. – The developed Love wave device can detect *E. coli* at a concentration of 4×10^5 cells/ml and *Legionella* at a concentration of 2.5×10^6 cells/ml. – Analysis time lower than 3 h.	[HOW 00]
– SH SAW devices fabricated on langasite (LGS) Euler angles (0°, 22°, 90°). – Transmission coefficient phase monitored using a HP 4195A network analyzer.	– Delay lines fabricated and derivatized with a rabbit polyclonal IgG antibody, which selectively binds to *E. coli* O157:H7. – Quantification of non-specific binding effect: use of an antibody directed against the trinitrophenyl hapten (TNP) as binding layer. – Use of 2 experimental methods: a liquid phase flow-through method and a dip-and-dry method. – The flow-through method produced a reduced (0.1–0.7°) variation in the $\angle S_{21}$ response, because of the relatively large distance of the *E. coli* from the sensitive LGS SH SAW surface. – For the dip-and-dry method, *E. coli* is selectively bound onto the surface of the LGS SH SAW delay line ⇨ $13.5° < S_{21}$ response < 15.5°.	[BER 05] and [BER 06]

2 Five Love-wave sensors prepared from ST-cut quartz substrates coated with SiO_2 guiding layer. Acoustic waves were excited perpendicular to the crystallographic *X*-axes at a working frequency between 147 and 150 MHz.

	– The same measurement for *E. coli* exposed to anti-TNP prepared surfaces ⇨ °0°< S_{21} response < 3°. – A 30:1 preference for *E. coli* binding to the anti-O157:H7 layer compared to the anti-TNP layer observed with fluorescence microscopy, confirming the selectivity of the antibody surface to *E. coli*.	
– Love plate device: ST quartz coated with a 4 µm thick sputtered SiO_2 layer. – f = 118 MHz. – Dual channel configuration. – Measurement of frequency variations.	– Use of 2 different molecules to immobilize anti-*E.coli* antibodies on the silica waveguide: a C22 organosilicon with terminal glycidyl groups and a (3-glycidoxypropyl) trimethoxysilane (GPTS) – Injection of GAM-γ Ab solution at 37°C ⇨ A frequency shift of ≈ 25 kHz at equilibrium for both GPTS and C22 monolayers ⇨ Nearly the same mass of anti-*E. coli* antibodies were immobilized. – If functionalized with C22 organosilicon SAM, addition of an *E. coli* bacteria suspension (10^6 CFU/mL) ⇨ Δf = 5.5 kHz in less than 100 min ⇨ Bacteria captured on the waveguide surface *E. coli* and detected in real time. – Functionalization of the surface with a GPTS monolayer ⇨ No significant sensor response.	[DIN 10]
– One-port SAW resonators (314.5 MHz). – Measurement of frequency variations.	– Measurements obtained by immersing a pair of gold electrodes into a sealed syringe filter which contained a culture solution containing lauryl sulfate trytose (LST). – Frequency changes of the two electrodes caused by generation of small CO_2 bubbles on the surface of the electrodes in series to a SAW resonator. – Signals 10 times greater than those obtained by conventional SAW systems. – The calibration curve of detection time versus density of *E. coli* showed a linear relationship with a correlation coefficient (R^2) of 0.9434 over the range of 10^2 to 10^7 cells/mL.	[CHA 12]

Table 3.4. *Survey of E. coli detection using SAW immunosensors*

Otori *et al.* developed a 42 YX $LiTaO_3$ SH-SAW sensor[3] to follow up the effect of H_2O_2 on the rat lung epithelial cell SV40-T2 in real-time. This design has enabled the sensitive monitoring of physical cell characteristics changes, such as viscosity or density inside the cells. Correlation between phase variation, insertion loss, and the destruction of the tight junction of the cells incubated on the SH-SAW device has been established [OTO 13].

Hao *et al*. have developed a Love wave device[4] to detect two types of cell: Jurkat and K562 in 15 min. Results show that the greatest sensitivity of detection, 10^3 cells/mL, was achieved with a silanized SAW when Jurkat cells were delivered into liquid micro-chambers of 1 mL. In this experiment, target cells were first coated onto the SAW surface and then specific Ab was added. The corresponding DL was found superior to that achieved with the conventional method (Ab applied first) [HAO 13].

3.4.4. *Virus detection*

In recent decades, there have been increasing cases of emerging and re-emerging diseases brought about by infectious viruses including dengue virus (DENV), influenza virus, hepatitis virus, human immunodeficiency virus (HIV), etc. Currently, the highest sensitivity for virus detection is achieved with assays relying on polymerase chain reaction (PCR). However, this technique requires a long processing time (typically 24 h) as well as advanced laboratory equipment and trained personnel. Therefore demand for sensitive and accurate viral biosensors with rapid detection systems is increasing. Techniques currently being applied to achieve this aim mainly include electrochemical biosensors, optical biosensors, using surface plasmon resonance (SPR), and quartz crystal microbalances [CAY 10, CHE 13]. However, detection of viral agents by Ab-coupled SAW is largely absent from the literature. In one of the few[5] published studies Tamarin *et al.* developed a Love wave sensor[6] and used it to study physical parameters of specific binding between antibodies and M13 bacteriophages [TAM 03].

3 Operating frequency ≈ 50 MHz.

4 SH-SAW fabricated with 36°rot $LiTaO_3$ substrate coated with a 4 µm thick SiO_2 guiding layer. Dual delay line configuration with an operating frequency of about 122.5 MHz.

5 Only 3 studies have been devoted to this field.

6 ST-cut quartz substrate with a 6 µm thick SiO_2 guiding layer. Operating frequency ≈100 MHz.

Results indicate that the immunosensor allowed detection tests up to 4×10^{12} pfu ml^{-1}, without saturation effect. A longer response time (about 2 h) is however necessary for high concentrations.

Bisoffi *et al.* [BIS 08] have investigated an immunobiosensor that combines the sensitivity of a Love wave sensor[7] with the specificity provided by antibodies for the detection of either Coxsackie virus B4 or the category A bioagent Sin Nombre virus (SNV). Results show that rapid detection (within seconds) of increasing concentrations of viral particles was linear over a range of order of magnitude for both viruses, and that for both pathogens, the sensor's selectivity for its target was not compromised by the presence of confounding Herpes Simplex virus type 1. Furthermore, the developed SAW biosensor was capable of selectively detecting SNV agents in complex solutions, such as naturally occurring bodies of water (river, sewage effluent) without analyte pre-processing.

The previous Love wave device has been investigated by the same team to detect Human Immunodeficiency Virus types 1 and 2 (HIV-1 and HIV-2). Rapid and accurate detection of HIV-1 and HIV-2 has been demonstrated in both simple (PBS) and complex solutions (including 50% of human serum). Additionally, results indicate that the developed sensor rapidly and differentially detects the virus of interest in the presence of a cross-confounding one [BIS 13].

3.4.5. *Cocaine detection*

Currently, the narcotic sniffing dog remains the most accurate, reliable and widely used sensing technology in the war on drugs. However, in the presence of non-target odors, these animals show a higher propensity for so-called false alarms. For this reason, there has been an increasing demand for a portable, highly specific vapor-sensing device capable of distinguishing a target vapor signature in a complex odor. Stubbs *et al.* [STU 03] have investigated real-time vapor phase detection of cocaine molecules with a SAW sensor[8] coated with anti-benzoylecgonine (anti-BZE) antibodies. A distinctive response or signature was observed under laboratory conditions,

7 A 36 rot $LiTaO_3$-based SAW transducer with 5 μm thick silicon dioxide waveguide sensor. Operating frequency ≈ 325 MHz.

8 An ST-X quartz resonator with a center frequency of approximately 250-MHz.

where the cocaine vapors were presented using an INEL vapor generator. The same work has been published in another paper [STU 05].

3.5. Conclusion

This review focuses on recent advances on immunosensing development and applications using SAW sensors. Even if the majority of applications do not deal with real clinical samples, the large range of concerned analytes (biomarkers, drugs, bacteria, cells, etc.) reveals the potential of this kind of biosensor in monitoring recognition of almost all the known pairs of Ag/Ab. In fact, sensitivity, miniaturization, absence of labeling requirements as well as the ability to *in situ* investigate the reaction dynamics of Ab/Ag binding, made these devices highly attractive compared to conventional bioassay techniques.

The continuing research on appropriate materials and structures allowing SAW confinement besides the use of high operating frequencies (in the GHz domain) allows us to envisage a new sensor developing with sufficiently high sensitivity for a large variety of applications.

3.6. Bibliography

[ALT 08] ALTSCHUH D., "Immunochemistry and Biosensors", *Actes ESONN' 07*, Grenoble – France, p. 80, 2008.

[BER 05] BERKENPAS E., MILLARD P., DA CUNHA M.P., "Novel O157: H7 E-coli detector utilizing a Langasite surface acoustic wave sensor", *IEEE Sensors*, vol. 1 and 2, pp. 1237–1240, 2005.

[BER 06] BERKENPAS E., MILLARD P., DA CUNHA M.P., "Detection of Escherichia coli O157: H7 with langasite pure shear horizontal surface acoustic wave sensors", *Biosensors and Bioelectronics*, vol. 21, pp. 2255–2262, 2006.

[BER 09] BERGAOUI Y., ZERROUKI C., FOUGNION J.M., *et al.*, "Sensitivity estimation and biosensing potential of lithium tantalate shear horizontal surface acoustic wave sensor", *Sensor Letters*, vol. 7, pp. 1001–1005, 2009.

[BER 11] BERGAOUI Y., ZERROUKI C., FOURATI N., *et al.*, "Antigen-antibody selective recognition using $LiTaO_3$ SH-SAW sensors: investigations on macromolecules effects on binding kinetic constants", *European Physical Journal Applied Physics*, vol. 56, p. 13705, 1–5, 2011.

[BIS 08] BISOFFI M., HJELLE B., BROWN D.C., *et al.*, "Detection of viral bioagents using a shear horizontal surface acoustic wave biosensor", *Biosensors and Bioelectronics*, vol. 23, pp. 1397–1403, 2008.

[BIS 13] BISOFFI M., SEVERNS V., BRANCH D.W., *et al.*, "Rapid detection of human immunodeficiency Virus Types 1 and 2 by use of an improved piezoelectric biosensor", *Journal of Clinical Microbiology*, vol. 51, pp. 1685–1691, 2013.

[BRA 04] BRANCH D.X., BROZIK S.M., "Low-level detection of a Bacillus anthracis simulant using Love-wave biosensors on 36 YX $LiTaO_3$", *Biosensors and Bioelectronics*, vol. 18, pp. 755–763, 2003.

[BRO 12] BRÖKER P., LÜCKE K., PERPEET M., *et al.*, "A nanostructured SAW chip-based biosensor detecting cancer cells", *Sensors and Actuators B*, vol. 165, pp. 1–6, 2012.

[CAM 98] CAMPBELL C.K., *Surface Acoustic Wave Devices for Mobile and Wireless Communications*, Academic Press Inc., 1998.

[CAM 13] CAMPANELLA H., "Aluminum nitride MEMS resonator-based sensors and transducers", *Instrumentation, Mesure, Métrologie*, vol. 3–4, pp. 39–58, 2013.

[CAY 10] CAYGILL R.L., BLAIR G.E., MILLNER P.A., "A review on viral biosensors to detect human pathogens", *Analytica Chimica Acta*, vol. 681, pp. 8–15, 2010.

[CHA 07] CHANG H.W., SHIH J.S., "Surface acoustic wave immunosensors based on immobilized C60-proteins", *Sensors and Actuators B,* vol. 121, pp. 522–529, 2007.

[CHA 12] CHANG Y-H., JANG H.D., HSU C.L., *et al.*, "Quantitative determination of Escherichia Coli in water sources in the environment using a surface acoustic wave impedance system modified with a syringe filter", *Analytical Letters*, vol. 45, pp. 1485–1494, 2012.

[CHE 13] CHENG M.S., TOH C.S., "Novel biosensing methodologies for ultrasensitive detection of viruses", *Analyst*, vol. 138, pp. 6219–6229, 2013.

[CHO 08] CHOU F-F., CHANG H-W., LI T.-L., *et al.*, "Piezoelectric crystal/surface acoustic wave biosensors based on Fullerene C60 and enzymes/antibodies/proteins", *Journal of the Iranian Chemical Society*, vol. 5, pp. 1–15, 2008.

[CHO 11] CHOI Y-S., DO J.P., LEE H.J., *et al.*, "A fully-automated surface acoustic wave immunosensing system for the detection of cardiac markers in whole blood", *15th International Conference on Miniaturized Systems for Chemistry and Life Sciences*, Seattle, Washington, WA, October 2–6, 2011.

[DEI 04] DEISINGH A.K., THOMPSON M., "Biosensors for the detection of bacteria", *Canadian Journal of Microbiology*, vol. 50, pp. 69–77, 2004.

[DIN 10] DINH D.H., PASCAL E., VELLUTINI L., *et al.*, "Novel optimized biofunctional surfaces for Love mode surface acoustic wave based immunosensors", *Sensors and Actuators A*, vol, 146, pp. 289–296, 2010.

[EGG 97] EGGINS B.R., *Biosensors: An Introduction*, John Wiley & Sons, 1997.

[FER 09] FERTIER L., CRETIN M., ROLLAND M., *et al.*, "Love wave immunosensor for antibody recognition using an innovative semicarbazide surface functionalization", *Sensors and Actuators B*, vol. 140, pp. 616–622, 2009.

[FRE 01] FREUDENBERG J., VON SCHICKFUS M., HUNKLINGER S., "A SAW immunosensor for operation in liquid using a SiO_2 protective layer", *Sensors and Actuators B*, vol. 76, pp. 147–151, 2001.

[GIZ 92] GIZELI E., GODDARD N-J., LOWE C-R.A., "Love plate biosensor utilising a polymer layer", *Sensors and Actuators B: Chemical*, vol. 6, pp. 131–137, 1992.

[GIZ 97] GIZELI E., "Design considerations for theacoustic waveguide biosensor", *Smart Materials and Structures*, vol. 6, pp. 700–706, 1997.

[GIZ 03] GIZELI E., BENDER F., RASMUSSON A., *et al.*, "Sensitivity of the acoustic waveguide biosensor to protein binding as a function of the waveguide properties", *Biosensors and Bioelectronics*, vol. 18, pp. 1399–1406, 2003.

[HAR 97a] HARDING G.L., DU J., "Design and properties of quartz-based Love wave acoustic sensors incorporating silicon dioxide and PMMA guiding layers", *Smart Materials and Structures*, vol. 6, pp. 716–720, 1997.

[HAR 97b] HARDING G.L., DU J., DENCHER P.R., *et al.*, "Love wave acoustic immunosensor operating in liquid", *Sensors and Actuators A*, vol. 61, pp. 279–286, 1997.

[HAR 13] HASANZADEH M., SHADJOU N., ESKANDANI M., *et al.*, "Electrochemical nano-immunosensing of effective cardiac biomarkers for acute myocardial infarction", *Trends in Analytical Chemistry*, vol. 49, pp. 20–30, 2013.

[HAO 13] HAO H.C., CHANG H.Y., WANG T.P., *et al.*, "Detection of cells captured with antigens on shear horizontal surface-acoustic-wave sensors", *Journal of Laboratory. Automation*, vol. 18, pp. 69–76, 2013.

[HAS 00] HASHIMOTO K.-Y., *Surface Acoustic Wave Devices in Telecommunications*, Springer, Berlin, p. 330, 2000.

[HAS 13] HASANZADEH M., SHADJOU N., SOLEYMANI J., *et al.*, "Optical immunosensing of effective cardiac biomarkers on acute myocardial infarction", *Trends in Analytical Chemistry*, vol. 51, pp. 158–168, 2013.

[HER 12] HERVAS M., LOPEZ M.A., ESCARPA A., "Electrochemical immunosensing on board microfluidic chip platforms", *Trends in Analytical Chemistry*, vol. 31, pp. 109–128, 2012.

[HOW 00] HOWE E., HARDING G.A., "Comparison of protocols for the optimisation of detection of bacteria using a surface acoustic wave (SAW) biosensor", *Biosensors and Bioelectronics*, vol. 15, pp. 641–649, 2000.

[JAK 11] JAKUBIK W.P., "Surface acoustic wave-based gas sensors", *Thin Solid Films*, vol. 520, pp. 986–993, 2011.

[KAL 14] KALETTA U.C., WENGER C., "FEM simulation of Rayleigh waves for CMOS compatible SAW devices based on AlN/SiO_2/Si(100)", *Ultrasonics*, vol. 54, pp. 291–295, 2014.

[KAR 11] KARDOUS F., EL FISSI L., FRIEDT J-M., *et al.*, "Integrated active mixing and biosensing using low frequency vibrating mixer and Love wave sensor for real time detection of antibody binding event", *Journal of Applied Physics*, vol. 109, p. 094701, 1–8, 2011.

[KOG 10] KOGAI T., YOSHIMURA N., MORI T., *et al.*, "Liquid-phase shear horizontal surface acoustic wave immunosensor", *Japanese Journal of Applied Physics*, vol. 49, p. 07HD15–5, 2010.

[KRI 08] KRISHNAMOORTHY S., ILIADIS A.A., BEI T., *et al.*, "An interleukin-6 ZnO/SiO_2/Si surface acoustic wave biosensor", *Biosensors and Bioelectronics*, vol. 24, pp. 313–318, 2008.

[LAN 03] LANGE K., BENDER F., VOIGT A., *et al.*, "A surface acoustic wave biosensor concept with Low Flow Cell Volumes for Label-Free detection", *Analytical Chemistry*, vol. 75, pp. 5561–5566, 2003.

[LEE 11] LEE J., CHOI Y.S., LEE Y., *et al.*, "Sensitive and simultaneous detection of cardiac markers in human serum using surface acoustic wave immunosensor, *Analytical Chemistry*, vol. 83, pp. 8629–8635, 2011.

[LEE 13a] LEE J., LEE Y., PARK J.Y., *et al.*, "Sensitive and reproducible detection of cardiac troponin I in human plasma using a surface acoustic wave immunosensor", *Sensors and Actuators B*, vol, 178, pp. 19–25, 2013.

[LEE 13b] LEE W., JUNG J., HAHN Y.K., *et al.*, "A centrifugally actuated point-of-care testing system for the surface acoustic wave immunosensing of cardiac troponin I", *Analyst*, vol. 138, pp. 2558–2566, 2013.

[LI 12] LI P., ZHANG Z., ZHANG Q., *et al.*, "Current development of microfluidic immunosensing approaches for mycotoxindetection via capillary electromigration and lateral flow technology", *Electrophoresis*, vol. 33, pp. 2253–2265, 2012.

[LOV 67] LOVE A.E., *A Treatise on The Mathematical Theory of Elasticity*, Dover, Cambridge, 1967.

[LUP 01] LUPPA P-B., SOKOLL L-J., CHAN D-W., "Immunosensors principles and applications to clinical chemistry", *Clin. Chim. Acta*, vol. 314, pp. 1–26, 2001.

[MAR 14] MARIANI S., MINUNNI M., "Surface plasmon resonance applications in clinical analysis", *Analytical and Bioanalical Chemistry*, vol. 406, pp. 2303–2323, 2014.

[MIT 09] MITSAKAKIS K., TSEREPI A., GIZELI E., "SAW device integrated with microfluidics for array-type biosensing", *Microelectronic Engineering*, vol. 86, pp. 1416–1418, 2009.

[MOR 96] MORGAN C.L., NEWMAN D.J., PRICE C.P., "Immunosensors: technology and opportunities in laboratory medicine", *Clinical Chemistry*, vol. 42, pp. 193–209, 1996.

[MUL 14] MÜLLER A., KONSTANTINIDIS G., BUICULESCU V., *et al.*, "GaN/Si based single SAW resonator temperature sensor operating in the GHz frequency range", *Sensors and Actuators A*, vol. 209, pp. 115–123, 2014.

[NAR 12] NARDI D., ZAGATO E., FERRINI G., *et al.*, "Design of a surface acoustic wave mass sensor in the 100GHz range", *Applied Physics Letters*, vol. 100, p. 253106, 1–4, 2012.

[O'SU 99] O'SULLIVAN C.K., VAUGHAN R., GUILBAULT G.G., "Piezoelectric immunosensors – theory and applications", *Analytical Letters*, vol. 32, pp. 2353–2377, 1999.

[OTO 13] OTORI H., HIGASHIYAMA T., UEHARA A., *et al.*, "Signal change of surface acoustic wave (SAW) caused by H_2O_2 damage to SV40-T2 cells cultivated on SH-SAW sensor", *Sensors and Actuators A*, vol. 200, pp. 162–167, 2013.

[PAN 12] PANG W., ZHAO H., KIM E., *et al*., "Piezoelectric microelectromechanical resonant sensors for chemical and biological detection", *Lab on Chip*, vol. 12, pp. 29–44, 2012.

[POW 06] POWELL D.A., KALANTAR-ZADEH K., WLODARSKI W., *et al.*, "Layered surface acoustic wave chemical and bio-sensors", in GRIMES C.A., DICKEY E.C., PISHKO M.V. (eds.), *Encyclopedia of Sensors*, vol. X, pp. 1–18, 2006.

[PRU 90] PRUSAK-SOCHACZEWSKI E., LUONG J.H.T.A, "New approach to the development of a reusable piezoelectric crystal biosensor", *Analytical Letters*, vol. 23, pp. 401–409, 1990.

[QUR 12] QURESHI A., GURBUZ Y., NIAZI Z.H., "Biosensors for cardiac biomarkers detection: a review", *Sens. Actuators B*, vol. 171, pp. 62–76, 2012.

[RUP 08] RUPP S., VON SCHICKFUS M., HUNKLINGER S., *et al.*, "A shear horizontal surface acoustic wave sensor for the detection of antigen–antibody reactions for medical diagnosis", *Sensors and Actuators B*, vol. 134, pp. 225–229, 2008.

[SHA 07] SHANKARAN R.D., GOBI K., MIURA N., "Recent advancements in surface plasmon resonance immunosensors for detection of small molecules of biomedical, food and environmental interest", *Sens. Actuat B Chem,* vol. 121, pp. 158–177, 2007.

[SHO 72] SHONS A., DORMAN F., NAJARIAN J., "An immunospecific microbalance", *Journal of Biomedical Materials Research*, vol. 6, pp. 565–570, 1972.

[STU 02] STUBBS D.D., HUNT W.D., LEE S.H., *et al.*, "Gas phase activity of anti-FITC antibodies immobilized on a surface acoustic wave resonator device", *Biosensors and Bioelectronics*, vol. 17, pp. 471–477, 2002.

[STU 03] STUBBS D.D., LEE S.H., HUNT W.D., "Investigation of cocaine plumes using surface acoustic wave immunoassay sensors", *Analytical Chemistry*, vol. 75, pp. 6231–6235, 2003.

[STU 05] STUBBS D.D., LEE S.H., HUNT W.D., "Vapor phase detection of a narcotic using surface acoustic wave immunoassay sensors", *IEEE Sensors Journal*, vol. 5, pp. 335–339, 2005.

[SU 95] SU C., BRANDT L.J., "Escherichia coli O157: H7 infection in humans", *Annals of Internal Medicine*, vol. 123, pp. 698–707, 1995.

[TAM 03] TAMARIN O., COMEAU S., DEJOUS C., *et al.*, "Real time device for biosensing: design of a bacteriophage model using love acoustic waves", *Biosensors and Bioelectronics*, vol. 18, pp. 755–763, 2003.

[TSO 08] TSORTOS A., PAPADAKIS G., MITSAKAKIS K., *et al.*, "Quantitative determination of size and shape of surface-bound DNA using an acoustic wave sensor", *Biophysics Journal*, vol. 94, pp. 2706–2715, 2008.

[VAU 03] VAUGHAN R.D., GEARY E., PRAVDA M., *et al.*, "Piezoelectric immunosensors for environmental monitoring", *International Journal of Environmental Analytical Chemistry*, vol. 83, pp. 555–571, 2003.

[VEL 09] VELASCO-GARCIA M.N., "Optical biosensors for probing at the cellular level: A review of recent progress and future prospects", *Seminars in Cell and Developmental Biology*, vol. 20, pp. 27–33, 2009.

[VOI 12] VOICULESCU I., NORDINB A.N., "Acoustic wave based MEMS devices for biosensing applications", *Biosensors and Bioelectronics*, vol. 33, pp. 1–9, 2012.

[WEI 98] WEISS M., WELSCH W., VON SCHICKFUS M., *et al.*, "Viscoelastic behavior of antibody films on a shear horizontal acoustic surface wave sensor", *Analytical Chemistry*, vol. 70, pp. 2881–2887, 1998.

[WEL 96] WELSCH W., KLEIN C., VON SCHICKFUS M., *et al.*, "Development of a surface acoustic wave immunosensor", *Analytical Chemistry*, vol. 68, pp. 2000–2004, 1996.

[WES 99] WESSA T., RAPP M., ACHE H.J., "New immobilization method for SAW-biosensors: covalent attachment of antibodies via CNBr", *Biosensors and Bioelectronics*, vol. 14, pp. 93–98, 1999.

[YAN 00] YANG V.C., NGO T.T., *Biosensors and Their Applications*, Kluwer academic, 2000.

[ZHO 04] ZHOU C., FRIEDT J.M., ANGELOVA A., *et al.*, "Human immunoglobulin adsorption investigated by means of quartz crystal microbalance dissipation, atomic force microscopy, surface acoustic wave, and surface plasmon resonance techniques", *Langmuir*, vol. 20, pp. 5870–5878, 2004.

[ZHO 10] ZHOU F.M., LI Z., FAN L., *et al.*, "Experimental study of Love-wave immunosensors based on ZnO/$LiTaO_3$ structures", *Ultrasonics,* vol. 50, pp. 411–415, 2010.

4

AC Nanocalorimeter on Self-standing Parylene Membrane

4.1. Introduction

Essentially based on microelectronics methods, microfabrication technology implements coating technologies, engraving and assembly to create structures and active components ranging from a micrometer to a millimeter. The development of these new advanced techniques allowed the thermometric sensor and calorimetry pool and the thermodynamics of small systems team to significantly improve the measurement performances in the field of thermometric and calorimetric measurements. By applying these innovative methods, we have developed an original measurement device used for specific heat experiments or more generally enthalpic measures not only at low temperatures but also at room temperatures. We developed this sensor using conventional cleanroom methods and hybrid metal/polymer structures.

4.2. Advantage of this type of microdevice

The heat capacity is a fundamental property of matter. It contains information on the densities of electronic and phononic states, magnetic interactions and phase transitions. The interest of a "tailor made" sensor is to

---

Chapter written by Emmanuel ANDRÉ, Aitor FERNANDEZ LOPEANDIA, Jean-Luc GARDEN, Dominique GIVORD and Olivier BOURGEOIS.

fully determine the dimensional and specific parameters needed to measure the desired type of sample. Now, new microfabrication techniques are used to work out temperature-tailored sensors and heating components to suit any type of sample. This technique also allows the reduction of addenda, which is a very important requirement in any calorimetric measurement. Moreover, the small dimensions of the support and active elements are an asset when the sample size is reduced.

4.2.1. *The samples*

The technical objective is to make measurements on samples weighing less than a milligram. This allows the study of materials such as thin films, small and structurally pure monocrystals and all kinds of samples that take a long time to synthesize and are, therefore, only available in small quantities. Furthermore, their small size makes them easy to thermalize, which is an essential condition for any fine calorimetric measurement.

4.2.2. *Measurement method: the AC calorimetry [SUL 68]*

Classical calorimetric measurement, called "adiabatic", is the most known and used today. It involves providing a known amount of heat in a thermally isolated sample and measuring its rise in temperature:

$$C = \frac{\delta Q}{dT}$$

This calorimetric method is difficult to apply for small sample measurements. Indeed, due to their small size, they are very hard to thermally insulate from their environment. The use of "quasi-adiabatic" methods is recommended with small samples because the thermal coupling between the measurement cell and the heat bath can be controlled.

A sinusoidal power $P(t) = P_0(1 + \cos \omega t)$ is delivered to the sample connected via a thermal conductance K_b to a temperature bath T_b. Under

stringent conditions (quasi-adiabaticity and uniform temperature), the temperature of the sample is the sum of a direct current (DC) component:

$$\Delta T_{dc} = \frac{P_0}{K_b}$$

and an oscillating component whose modulus is inversely proportional to the heat capacity of the sample that we want to know:

$$\delta T_{ac} = \frac{P_0}{\omega C}$$

The measurement of this oscillation amplitude using a locking amplifier allows us to obtain superior sensitivity to other methods of measurement. The drastic conditions mentioned define the measurement frequency regime for the sensor.

$$1/\tau_b << \omega << 1/\tau_{\text{int}}$$

where τ_b is the relaxation time of the temperature to the thermal bath and τ_{int} is the internal relaxation time due to the diffusivity in the sample and the sensor. In general, we want to work in a reasonable frequency band between 100 mHz and 1 KHz and with an adiabatic frequency lower than the thermal diffusion rate. With these constraints, we evaluate what should be the geometry, materials used and the thermal characteristic time for the device.

4.3. Nanocalorimeter for measuring nano objects

The specificity of this sensor is to work with temperature oscillations at very low frequencies to highlight heat released in magnetic nanomaterials. We used a sample holder consisting of a cross suspended polymer para-xylylene (or parylene) composed of lithographed elements for the measurement. Parylene, with its many qualities, allows the manufacture of very thin membranes (200 nm) with fine (50 µm) and long suspension arms (1 mm). Thus, the system has a very low specific heat and is very isolated to the thermal bath.

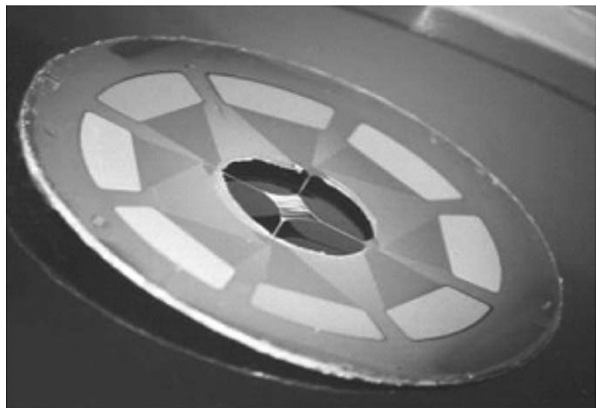

Figure 4.1. *Nanocalorimeter of suspended parylene membrane*

4.3.1. *The parylene membrane*

A new polymer (parylene or para-xylylene) deposited with chemical vapor deposition (CVD) process permits us to obtain very thin membranes with controlled thickness and, thus, dramatically improve the performance of the sensor by reducing addenda.

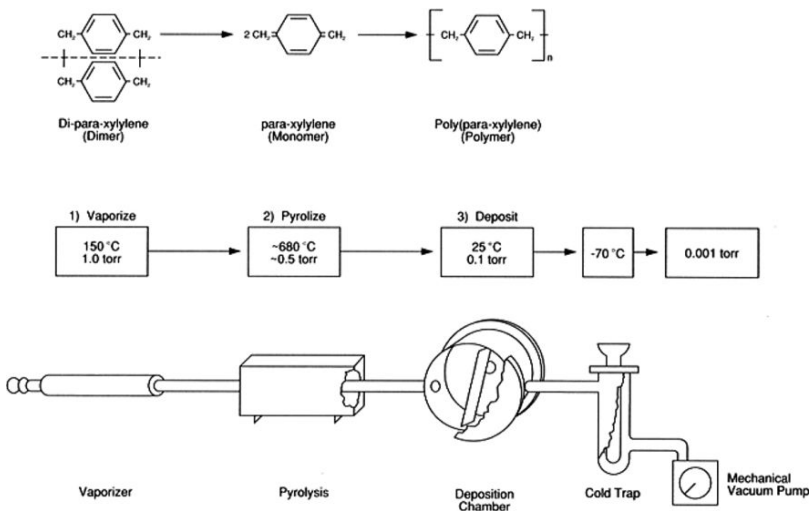

Figure 4.2. *Parylene deposition principle [GOR 66]*

The process of development similar to CVD gives very interesting properties in terms of homogeneity and thickness uniformity of the coating. Moreover, the deposition is performed at room temperature without solvent, therefore, without residual stress in the coating. This transparent film, semi-crystalline, with a thickness between 10 nm and 100 μm has high thermodynamic stability, excellent solvent resistance and high dielectric strength.

4.3.2. *Thermometer and heater in NbN_x*

All the active coating and the current leads are made in niobium nitride by reactive sputtering. They have different compositions in order to obtain thermal and electrical resistivity adapted to the specifications. The NbNx deposition is performed with a magnetron cathode powered with pulsed DC for sputtering a pure Nb target (99.95%) in an Ar/N2 gas mixture of high purity (99.99%). Mass flow controls precisely the amount of gas injected into the deposition chamber and a butterfly valve allows us to obtain a fixed work pressure of 2.10–2 mbar. The sputtering parameters, such as the gas mixture ratio, the frequency and the power supplied to the magnetron, are carefully controlled to adjust the nitrogen content in the layer and achieve the good stoichiometric composition and microstructure [BOU 06]. Depending on the ratio x = N/Nb, the electrical properties are very different. For $x < 0.6$, the material behaves like a metal superconductor with a critical temperature of about 15 K. For $x > 1$, the material behaves as a Mott insulator [IMA 98] characterized by a metal–insulator transition at a temperature dependent on the nitrogen content of the layer. A material with a high nitrogen concentration (NbN1.7) was recommended for a thermometer having a metal–insulator transition at high temperature [BOU 06]. The thermometer sensitivity defined by the temperature coefficient ratio (TCR) is nearly 10 times the typical values found for the platinum thermometers. Otherwise, as a heating element, a material with low TCR in the temperature range will be preferred. In fact, the power dissipated by the Joule effect will be substantially constant in the temperature range even if the same current value is used. For this reason, a material with a low nitrogen concentration (NbN1.1) is chosen (Figure 4.3).

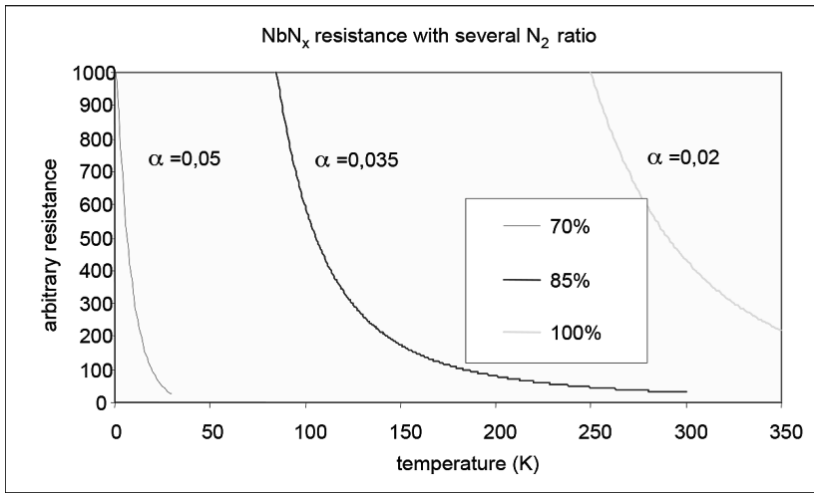

Figure 4.3. *NbN_x with different N2 ratios in the process gas ($\alpha = 1/R.\Delta R/\Delta T$)*

Moreover, with this nitrogen composition value, this compound has a high electrical resistivity, two orders of magnitude greater than the typical values of the metallic Nb (10–5 Ω cm for NbN1.7 to 10–3 Ω cm for NbN1.1 at room temperature [LER 07]). An estimation of the thermal conductivity using the Wiedemann–Franz law shows a thermal conductivity value 70 times lower compared to the platinum value, for example. This demonstrates that the NbN is perfectly suited for the manufacture of the current leads, since the edge of the sensor to its center.

4.3.3. *Manufacturing*

Twenty-one various technological steps and seven alignment levels are necessary for the achievement of this sensor. We are going to develop here the main steps. On a polished copper substrate of 20 mm diameter and 0.5 mm thickness, a first thick coating (3 μm) of parylene is deposited under vacuum. After this, a first thin NbNx layer is deposited, microlithographed and etched. This will be the heating element. In an another step it will be electrically insulated with another thinner layer of Parylene (0.3 μm) and

will again be coated with a thin layer of NbNx with a small amount of nitrogen (x ~ 1.1). After microlithography, this lithographic element will supply the thermometer which will be made later.

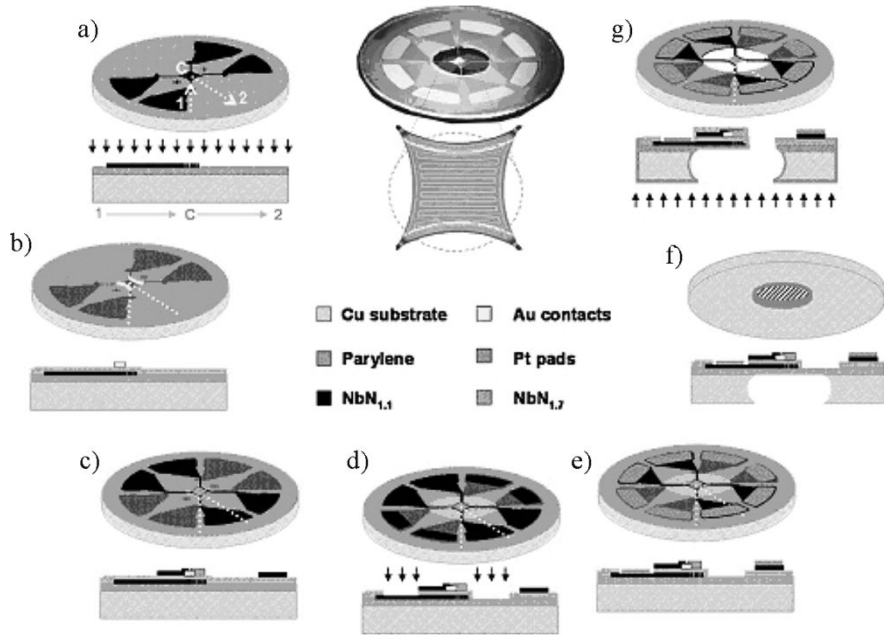

Figure 4.4. *Central picture: finished device and a detailed view of the heater shape by transparency. Drawing: schematic of the cell fabrication, all three-dimensional views are complemented by a cross-sectional view following the direction described in a), b): gold contact deposition; c): contact leads of NbN1.1; d): soft plasma attack; e): Pt contact deposition; f): backside copper etching; g): final structuring by plasma*

A detailed view of the heating layout is show in Figures 4.4 and 4.5. The heating zone is defined by 1 mm^2 of active lithographed meander coating area with 33 μm width. This meander is used in a "four wire" configuration and the voltage and current wires come from the four structuring bridges of the membrane. To improve the suspension arm mechanical strength, a parabolic design is chosen, thereby enhancing stress resistance during thermal expansion of the support relative to the membrane during the steps of etching or deposition.

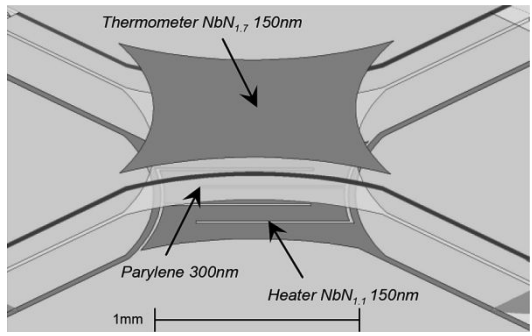

Figure 4.5. *Schematic view of the sensor center*

Electrically isolated with the parylene to the NbNx heater located on the lower layer, the thermometer is deposited on the third level. It is divided into three parts which are detailed in Figures 4.4(b) and (c): the gold contact electrodes, the current wires and the thermometer in NbNx with good nitrogen composition (x = 1.1 and x = 1.7), all made by standard lithography and "lift-off" process. First, 50 nm of gold is deposited on the electrodes with an adhesion layer of 10 nm W/Ti. Subsequently, the electrodes are connected by four current leads of 100 nm NbN1.1 with the same layout as the current wires of the meander heating. In the end, the thermometer is deposited on and between the two connecting electrodes (Figure 4.5). The best conductivity of gold compared to NbN1.7 permits us to generate a perpendicular electric field to the meandering heating. Thus, the voltage can be measured in a four wire configuration and the uniform distribution of current through the thermometer avoids inductive coupling with the heating and inversely with the thermometer. Furthermore, in the measurement temperature range, the thermometer is comparable (few kΩ) to the heating (Figure 4.7).

After the deposition of the thermometric NbNx layer, the thin parylene membrane is etched using an O2/Ar soft plasma etching step by the upper face of the sample. As shown in Figure 4.4(d), the thermometer and the current leads in NbNx are used as a mask to protect parylene insulating the two levels (thermometer and heating). Only 500 nm of exposed parylene is eliminated. This process also releases the contacts coated by this layer of parylene. Moreover, after this step, all contacts are covered with 100 nm of platinum by the "lift off" method to improve the contact resistance with external connections. Then the membrane is released as shown in

Figure 4.4(f): the two sides of the device are protected by a photosensitive resin and a window is opened by lithography on the back of the copper substrate. Once immersed in a ferric chloride bath, the unprotected copper is attacked up to the parylene layer of the front side. Then, a plasma attack will completely remove this layer of parylene. This "dry" method provides a completely suspended and very fine structure with long bridges. For this step, the etching is done by the bottom face (the sample is reversed) to etch the first parylene layer of 3 μm and keeping only the parylene layer between the heating and thermometer. Finally, the calorimetric cell is covered by a layer of 100 nm parylene to electrically isolate the thermometer. Only platinum contacts at the edge of the device are protected from deposits. Now, a sample may be deposited or placed on the thermometer, to be characterized.

4.3.4. *Sample placement*

Two types of sample can be placed on the central cross: thin films using a mechanical mask during deposition or microcrystals with microtweezers.

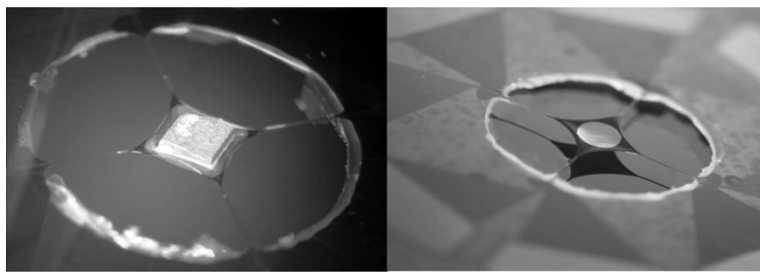

Figure 4.6. *Examples: microcrystal bonding and thin film deposition*

4.4. Device performances

4.4.1. *Temperature calibration*

After cool down, the sample in the cryostat, a calibration of the heater and thermometer as a function of the temperature is performed. They are polarized (in four wire configuration) with an alternating (AC) performed of 50 nA, being careful to avoid self-heating. The first harmonic of the voltages is measured with a lock-in amplifier SR830 in the temperature range of interest.

It has been checked that the stability of NbNx is good enough and the variation of resistance is better than 50 ppm in a week at temperatures below 250 K. Figure 4.7 shows the calibration of the heater.

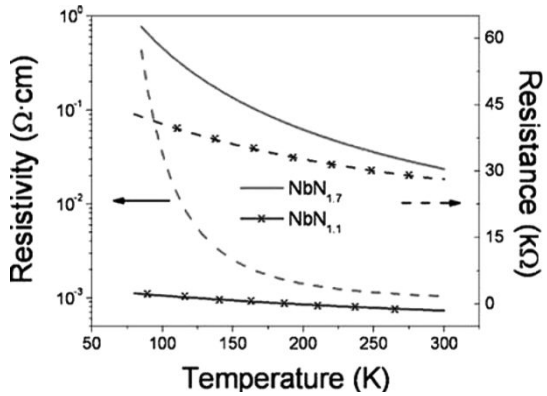

Figure 4.7. *Resistivity (solid line) and resistance (dashed line) in a finished device*

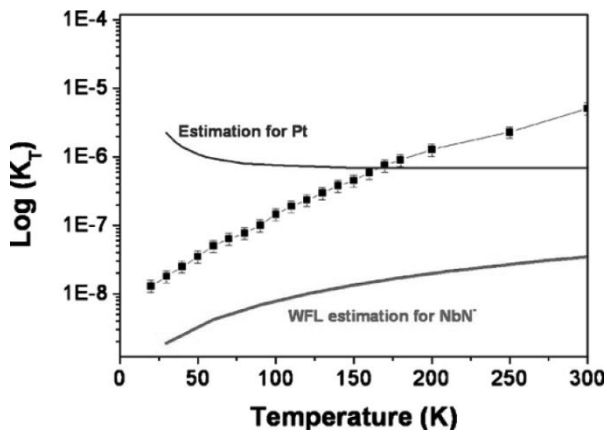

Figure 4.8. *Thermal conductance between the calorimetric cell and the copper frame and estimation of thermal conductance for both materials used as contact leads (Pt and NbN_x)*

4.4.2. *Thermal conductance of the empty cell*

Figure 4.8 shows the measurement of the thermal conductance of the arm. It was determined by measuring the rise in temperature when a constant power is injected into the calorimetric cell.

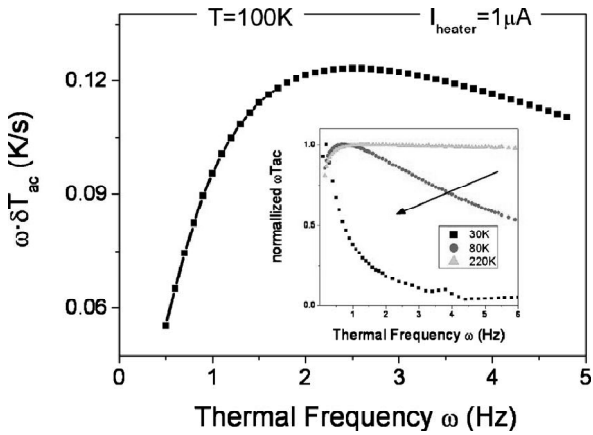

Figure 4.9. *Adiabatic plateau and evolution at different temperatures (in the inset)*

For a given temperature, each point is obtained by adjusting the linear regression δTdc obtained for various input powers. In the same graph, we also numerically estimated the contribution of the thermal conduction of the current leads when using Pt or NbNx. In each case, the geometry considered is four arms with two wires for each arm: 100 nm thick, 100 μm wide and 1 mm long. The platinum thermal conductivity value was found in the literature [SHA 01] and for NbNx we use the Wiedemann–Franz law from the measured electrical resistivity. The difference between the estimation of the conductivity of NbNx by the Wiedemann–Franz law and the experimental measurement can be explained by the contribution of parylene in the total conductance.

4.4.3. *Dynamic characterization of an empty calorimetric cell*

The maximum value of the temperature oscillation in the heating/cooling δTac for a fixed excitation current is a function of the time constant of internal thermal diffusion of the cell and external thermal conduction by the arm. Figure 4.9 shows the adiabatic characteristics of the dynamic response of the calorimeter measured at 100 K with an excitation current of 1 μA. At low frequencies, the decrease in the signal δTac may be observed. This occurs when the frequency is close to the typical values of internal thermal relaxation of the cell across the conducting arms (ωext = 1/τext = K/Cp).

In this case, the calorimeter signal is composed of a background signal due to loss by conduction. As shown in the inset of Figure 4.9, the external relaxation time remains in the same order of magnitude as in the temperature range. This is due to the similar thermal behavior of the thermal conductivity and the heat capacity. To remain thermally isolated, the experiment must base its measurement on this cutoff frequency, always above 0.1 Hz. At high frequencies, the decrease in δTac at the quasi-adiabatic plateau is due to the thermal diffusivity limit in the calorimetric cell. The inset of Figure 4.9 shows us how this threshold moves to lower frequencies as the temperature decreases. This phenomenon is directly related to the reduction of the horizontal conductivity mainly due to the properties of parylene. For all these reasons, all experiments are performed in a range between 0.5 and 5 Hz, where the maximum values of ωδTac, whatever the temperature, can be found. Furthermore, the continuous temperature gradient δTdc is about a few Kelvin between the cell and the baseline.

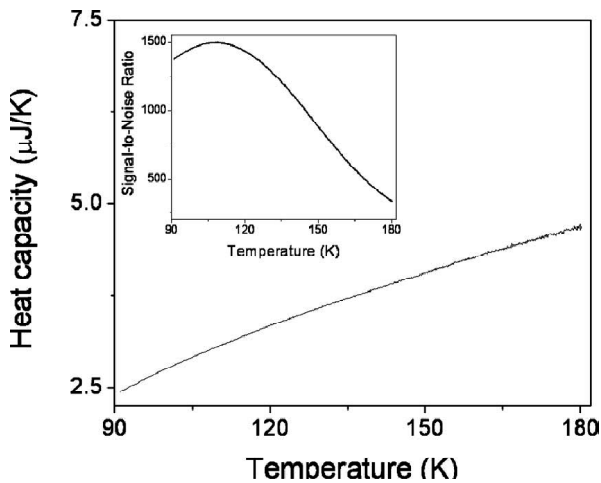

Figure 4.10. *Heat capacity for an empty calorimetric cell and signal/noise (in the inset)*

4.4.4. *Heat capacity of an empty calorimetric cell*

In Figure 4.10, the heat capacity is represented as a function of temperature for an empty calorimetric cell. The value is a few μJ/K. The measurement was taken with 10 μA at a frequency of 2.2 Hz for the heating

power and 500 nA for biasing the thermometer. The heat capacity is measured every 0.1 K in a range between 90 and 200 K. At each temperature level, the signal-to-noise ratio (SNR) is improved by averaging over 50 measurements, each measurement is integrated on 1 s. The calorimeter signal is limited by the Johnson noise thermometer by the very small oscillation in temperature and very low bias current in the thermometer (100 K, Vb ~ 10 nV/√Hz). Also, a compromise is made between the maximum temperature offset (via the heating and the thermometer current) and the temporal averaging. In the box in Figure 4.10, we can observe the SNR remaining around 10^3. This ratio can be improved by increasing the averaging time of measurement. Despite the high thermal decoupling and the limited polarization current of the thermometer and heater, this calorimeter can perform scans continuously over a range of 100 K with a sensitivity less than 1 nJ/K, i.e. detecting a variation of energy less than 1 pJ for 1 mK temperature oscillation [BOU 07, LOP 10]. This calorimeter measures small microcrystals or thin layers; it is interesting to give the figure of merit defining the sensitivity per unit area. To compare with other calorimeters we give the sensitivity by μm^2: 10^{-15} J/Kμm^2.

4.4.5. *Heat capacity of a $GdAl_2$ microcrystal*

To demonstrate the possible use of the calorimeter for phase transition measurement, we measured a GdAl2 pure microcrystal. This material is a rare earth of aluminum alloy that has a high Curie temperature, around 168 K. It is considered as a good example of Heisenberg ferromagnetism [DU 88, DEE 71]. A microcrystal of 450 mg was laid onto the calorimeter using a micromanipulator. To improve the thermal contact, an adhesive microdroplet at low viscosity is deposited (Epotecny® E501) in the center of the sensor before installing the microcrystal (see Figure 4.6). Figure 4.11 shows the heat capacity and the phase measured from 150 to 190 K. In the two curves, the transition of order–disorder phase appears at 172.1 K. After subtracting the phonon heat capacity (calculated with Debye model), the excess magnetic heat capacity is plotted in Figure 4.12. The heat capacity jump of 15 μJ/K corresponds to the specific heat jump of 7 μJ/K mol expected from previous measurements [SHA 01], if we consider a weight of 450 mg with a molar mass of 211 g/mol.

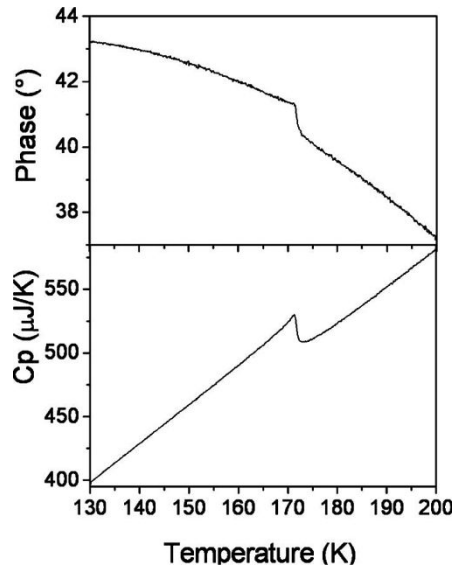

Figure 4.11. *Heat capacity and phase variation of a $GdAl_2$ microcrystal fixed to the center of the sensor*

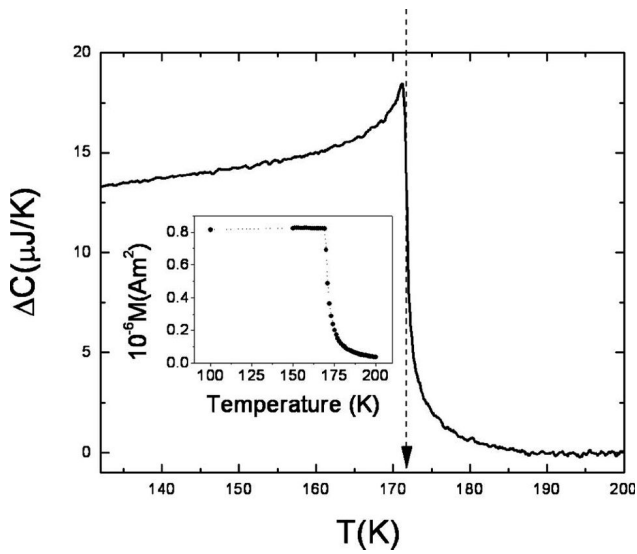

Figure 4.12. *Heat capacity after subtracting the phononic heat capacity and magnetic measurement (inset) of the sample before assembly over the sensor*

4.5. Conclusion

In this work, we presented a very sensitive AC calorimeter based on a new concept using a parylene membrane as a mechanical support. The heater and thermometer are lithographed on both sides of the polymer membrane. The thermal insulation has been deliberately set to enable the sensor to work at low temperatures. The best sensitivity obtained is less than 1 nJ/K, for a resolution (ΔC/C) between 10–3 and 10–4. The performance of the calorimeter is only limited by the Johnson noise thermometer. This sensor has been used to measure the heat capacity of a GdAl2 microcrystal and specific heat jump has been detected correspondent at the ferromagnetic phase transition, reflecting qualities of this new device. This sensor will be used in the future for the study of phase transitions in low dimension magnetic systems. The scientific perspectives are promising not only for the calorimetric study of small mass objects but also for the study of polymers or biophysical systems at room temperature and phenomena involving slow thermal relaxation will be able be observed [CHA 05, GAR 09]. Hybrid thin films and microfluidic sensors are now currents in this scientific research field. Due to the high resolution and sensitivity of the microdevice, new thermal and thermodynamic phenomena can be detected. Moreover, suspended membranes suggest the broader applicability. Other types of active metallic coating or polymeric material element can be used on this type of membrane, especially where mechanical flexibility is required. The use of polymers and more particularly parylene is perfectly suited to this type of field.

4.6. Acknowledgments

We thank the Thermometric Sensors and Calorimetry pool and the Cryogenics and Electronics Service of the Néel Institut for their valuable assistance and J. Chaussy for fruitful discussions and initiating these works. This research was supported by an Intra European Marie Curie grant under the 7th Framework Program of the European Community.

4.7. Bibliography

[BOU 06] BOURGEOIS O., ANDRÉ E., MACOVEI C., *et al.*, "Liquid nitrogen to room temperature thermometry using niobium nitride thin films", *Review of Scientific Instruments*, vol. 77, p. 126108, 2006.

[BOU 07] BOURGEOIS O., MACOVEI C., ANDRÉ E., *et al.*, "A new sensor for thermodynamic measurements of magnetization reversal in magnetic nanomaterials", *Journal of Magnetism and Magnetic Materials*, vol. 316, pp. e94–e96, 2007.

[CHA 05] CHATEAU E., GARDEN J.L., BOURGEOIS O., *et al.*, "Physical kinetics and thermodynamics of phase transitions probed by dynamic nanocalorimetry", *Applied Physics Letters*, vol. 86, p. 151913, 2005.

[DEE 71] DEENADAS C., THOMPSON A.W., CRAIG R.S., *et al.*, "Low temperature heat capacities and related thermal properties of $TbAl_2$ and HoAl2", *Journal of Physics and Chemistry of Solids*, vol. 32, p. 1853, 1971.

[DU 88] DU TREMOLET DE LACHEISSERIE E., "Magnetic properties and critical behaviour of GdAl2: Thermal expansion, magnetization, magnetostriction and magnetocaloric effect", *Journal of Magnetism and Magnetic Materials*, vol. 73, p. 289, 1988

[GAR 09] GARDEN J.-L., GUILLOU H., LOPEANDIA A.F., *et al.*, "Thermodynamics of small systems by nanocalorimetry: from physical to biological nano-objects", *Thermochimica Acta*, vol. 492, pp. 16–28, 2009.

[GOR 66] GORHAM W.F., "A new, general synthetic method for the preparation of linear poly-p-xylylene", *Journal of Polymer Science*, part A-1, vol. 4, pp. 3027–3039, 1966.

[IMA 98] IMADA M., FUJIMORI A., TOKURA Y., "Metal–insulator transitions", *Reviews of Modern Physics*, vol. 70, p. 1039, 1998.

[LER 07] LEROY G., GEST J., VANDAMME L.K.J., *et al.*, "Noise measurements on NbN thin films with a negative temperature resistance coefficient deposited on sapphire and on SiO_2", *Fluctuation and Noise Letters*, vol. 7, p. L19, 2007.

[LOP 10] LOPEANDIA A.F., ANDRÉ E., GARDEN J.-L., *et al.*, "Parylen membrane-based AC-calorimeter for small magnetic samples", *Review of Scientific Instruments*, vol. 81, no. 5, p. 053901, May 2010.

[SHA 01] SHACKELFORD J.F., ALEXANDER W., in SHACKELFORD J.F., ALEXANDER W. (eds.), *Materials Science and Engineering Handbook*, CRC, BOCA RATON 2001.

[SUL 68] SULLIVAN P.F., SEIDEL G., "Steady-state, ac-Temperature calorimetry", *Physical Review*, vol. 173, pp. 679–685, 1968.

[WAN 08] WANG L, SIPE D.M., XU Y., *et al.*, "A MEMS thermal biosensor for metabolic monitoring applications", *Journal of Microelectromechanical System,* vol. 17, pp. 318–327, 2008.

5

Oscillatory Failure Detection in the Flight Control System of a Civil Aircraft Using Soft Sensors

5.1. Introduction

The safe operation of a physical process can be harmed on the occurrence of faults, these faults may affect the process itself or its control components (actuators, sensors, power or information networks, etc.). This observation has naturally led to the implementation of surveillance systems whose objective is to be able at any moment, to provide operating status of the various organs constituting the system. When a fault occurs, it must be detected as soon as possible, even where all observed signals remain in their allowable limits. It must then be located and its cause identified. Thus, the steps of observation and monitoring must be assisted by a "smarter" step.

This step, called supervision, uses all available information through an implicit or explicit model. Here, the goal is the detection of oscillatory failures affecting a flight control surface (FCS) – specifically an aileron – of an aircraft. For these oscillatory failures, airworthiness regulations applied worldwide by all manufacturers require precaution designed to detect and to accommodate these failures (see [GOU 10, MAR 12]). Software embedded on the Airbus A380, for example, is entirely compliant with the current regulations. However, improvements [LAV 08] could be used for the next

Chapter written by Do Hieu TRINH, Benoît MARX, Philippe GOUPIL and José RAGOT.

generation of aircraft from European manufacturers to accompany the future technological innovations and meet changing regulations. That is the purpose of this study. Examples of oscillatory failure detection in other areas can be found in [DAS 00, HE 07]. Note also that these oscillatory failures are different from pilot-induced oscillations (PIO) caused by the pilot (see [JER 03, MIT 04]). In the following, some elements leading to a methodology to detect such failures are presented, which are based on existing sensors and on *soft (or virtual) sensors* capable of reconstructing some information through a model of the sensors.

The principle of supervision is presented in section 5.2 and the design of a soft sensor for the oscillatory failure case detection in section 5.3. Section 5.4 tackles the problem of fault detection and isolation (FDI) by the test of standard deviation. This problem is treated in section 5.5 by a correlation test between several residuals. Conclusion and perspectives end this chapter.

5.2. Modeling of the studied system

The traditional approach to FDI in a flight control system (CS) makes use of hardware redundancy by a replication of hardware [GOU 10] such as sensors, actuators or even flight control computers [SUN 12]. However, in respect to financial cost, there is a growing interest in methods that do not require additional hardware redundancy, these methods being based on software redundancy [ALW 11, VAR 12, SIF 12, CIE 13].

Fault diagnosis methods are generally classified into two groups, model-based and data-driven methods depending on the knowledge we have or not on the system under investigation. Here we are concerned with a relatively simple system that can be easily modeled from mechanical considerations and physical assumptions.

The chosen principle for diagnosis is based on testing the adequacy of available measures in a CS servo-loop toward its model. Thus, it is necessary to establish the model of the system and then to generate failure indicators by comparing the outputs of the simulated models and the available measures. These indicators – also called residuals – must be analyzed to detect the presence of failure(s) as soon as possible. A model called *failure-free* can be proposed simulating the system behavior in the absence of failure. *Failure models* corresponding to system behaviors in occurrence of oscillations can

also be established. Two kinds of failures must be detected, which are identified as "liquid failure" and "solid failure" as a disturbing signal is superimposed on or replaces the control signal [LAV 08, TRI 10]. The probable sources of oscillatory failure are presented in Figure 5.1.

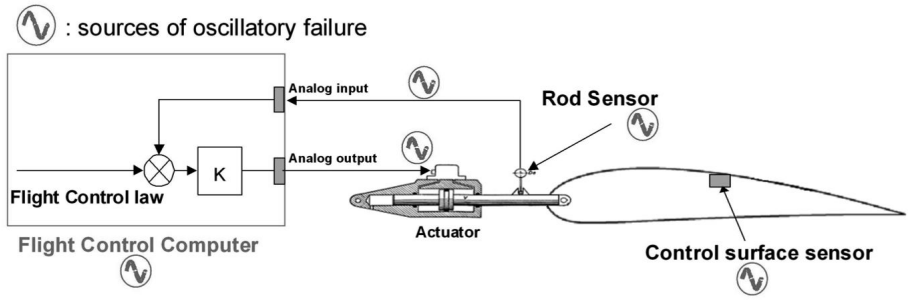

Figure 5.1. *The probable sources of oscillatory failure*

The characteristic variables of the considered CS servo-loop are given in Table 5.1.

$x_b(t)$	position of the rod of CS actuator (aileron)
$u(t)$	position's order of CS actuator
$F_a(t)$	aerodynamic forces applied on the CS
$M_a(t)$	aerodynamic hinge moment
$\Delta P(t)$	difference of hydraulic pressure in the input of the CS actuator
$V_0(t)$	speed computed by flight control computer
$x(t)$	position (in degrees) of the CS
$K_a(t)$	damping coefficient of adjacent actuator (case of 2 actuators per CS)
ΔP_{ref}	pressure of reference
τ	transmission delay of the sensor
S	surface area of the actuator's piston
K	control gain

Table 5.1. *Characteristic variables and constants of CS servo-loop*

The failure-free model M_b is structurally described as follows:

$$M_b = \begin{cases} \dot{x}_b(t) & = V_0(t)\sqrt{\dfrac{S\Delta P(t) + \text{sign}(V_0(t))F_a(t)}{S\Delta P_{ref} + K_a(t)V_0^2(t)}} \\ V_0(t) & = K(u(t) - x_b(t-\tau)) \\ \Delta P(t) & = f_1(x_b(t)) \\ K_a(t) & = f_2(x_b(t)) \\ F_a(t) & = f_3(M_a(t), x_b(t)) \\ x(t) & = f_4(x_b(t), \tau) \end{cases} \quad [5.1]$$

where the structure of functions $f_i(.)$ are not detailed here. The quantities $\Delta P(t)$, $K_a(t)$ and $F_a(t)$, generally unmeasurable, play the role of disturbances, for that the range of variation is known. Failure models of solid and liquid types, respectively, take the following forms:

$$M_s = \begin{cases} \dot{x}_s(t) & = V_{0,s}(t)\sqrt{\dfrac{S\Delta P(t) + \text{sign}(V_{0,s}(t))F_a(t)}{S\Delta P_{ref} + K_a(t)V_{0,s}^2(t)}} \\ V_{0,s}(t) & = S_{def,s}(t) \end{cases} \quad [5.2]$$

$$M_\ell = \begin{cases} \dot{x}_\ell(t) & = V_{0,l}(t)\sqrt{\dfrac{S\Delta P(t) + \text{sign}(V_{0,\ell}(t))F_a(t)}{S\Delta P_{ref} + K_a(t)V_{0,\ell}^2(t)}} \\ V_{0,\ell}(t) & = K(u(t) - x_\ell(t-\tau)) + S_{def,\ell}(t) \end{cases} \quad [5.3]$$

where the magnitudes of $\Delta P(t)$, $K_a(t)$ and $F_a(t)$ depend on flight scenario; $S_{def}(t)$ represents the oscillatory failure signal of unknown magnitude and frequency, but characterized by a known frequency range (from 0.5 Hz to 10 Hz). It is important to note that the two models M_b, M_s are related to the failure of a nonlinear way through the influence of $V_{0,\ell}$ and $V_{0,s}$. That will explain the further comments in section 5.4.4 about the frequency of the failure.

The models [5.1], [5.2] and [5.3], taken from [GOU 10], are used for FDI. The principle of supervision, which is therefore to determine at every moment which mode of the system M_b, M_s or M_ℓ is active, is the subject of section 5.3. Note that after recognition of a faulty mode, we have to apply the control signal to another adjacent actuator in order to reduce the oscillation magnitude. Control reconfiguration is not the purpose of the current work, but some details on this topic can be found in [KIM 03].

5.3. Design of a soft sensor for the oscillatory failure detection

The evolution of the system outputs, respectively, denoted by x_b, x_s and x_ℓ, whether they are generated by [5.1], [5.2] or [5.3], are computed by integrating, according to the time, the equations related to the three operation modes of the CS. In this case, we speak about soft sensors, because the simulation provides information comparable to what gives a physical sensor, under condition that the model is well representative of the system. At each time instant, this allows us to propose a diagnostic strategy summarized in Table 5.2.

E_1	At time t, acquire the available measures, mainly $x(t)$ and $u(t)$
E_2	Evaluate the outputs ($x_b(t)$, $x_s(t)$, $x_\ell(t)$) of the three soft sensors
E_3	Calculate the residuals $r_\lambda(t) = x(t) - x_\lambda(t)$, $\lambda = b, s, \ell$
E_4	Compare the residuals $r_\lambda(t)$ in respect to given thresholds
E_5	Test the persistency over time of the result of statistic tests
E_6	Take the decision of the occurrence of a failure

Table 5.2. *Strategy for fault detection*

The comparison between the outputs of these soft sensors and the growths measured by physical sensors results in three residual signals allowing us to determine the most representative model of the actual behavior of the CS and thus to determine online the type of the potentially occurring failure. Note that one of the major difficulties in the implementation of this technique is due to the fact that the physical system is subjected to hardly measurable disturbances ($\Delta P(t)$, $K_a(t)$ and $F_a(t)$). In [LAV 08], the authors have shown that $\Delta P(t)$ and $F_a(t)$ cannot be simultaneously identified and they have chosen to set $\Delta P(t)$ to its most likely value then identify $K_a(t)$ and $F_a(t)$. Taking into account the complexity of the estimation of $K_a(t)$ and $F_a(t)$ as well as the limited power of the flight control computer, the model was simplified by fixing the three perturbations $\Delta P(t)$, $K_a(t)$ and $F_a(t)$ to constant values ΔP_b, K_{ab} and F_{ab}[1]. From equation [5.1], the corresponding evolution of the output $x_b(t)$ is then reduced to:

$$M_b = \begin{cases} \dot{x}_b(t) = V_0(t)\sqrt{\dfrac{S\Delta P_b + \text{sign}(V_0(t))F_{ab}}{S\Delta P_{ref} + K_{ab}V_0^2(t)}} \\ V_0(t) = K(u(t) - x_b(t-\tau)) \end{cases} \quad [5.4]$$

In fact, there are several flight scenarios. We may cite the following scenarios: cruise phase, "nose-up" (abrupt longitudinal maneuver), triggering of pitch protection, "yaw-angle-mode" (which roughly corresponds to an enhanced auto-pilot hold mode). For each scenario the values of ΔP_b, K_{ab} and F_{ab} are adapted. This adaptation is not a handicap, because the recognition of the scenario is pretty obvious. Figure 5.2 shows the input of the system, the output of the nonlinear model [5.1] and that of its simplified model [5.4]; the low amplitude of the difference between the two outputs (namely $r_b(t) = x(t) - x_b(t)$) fully justifies the use of the simplified model [5.4].

1 Numerical values of the system parameters are not given here for the sake of confidentiality.

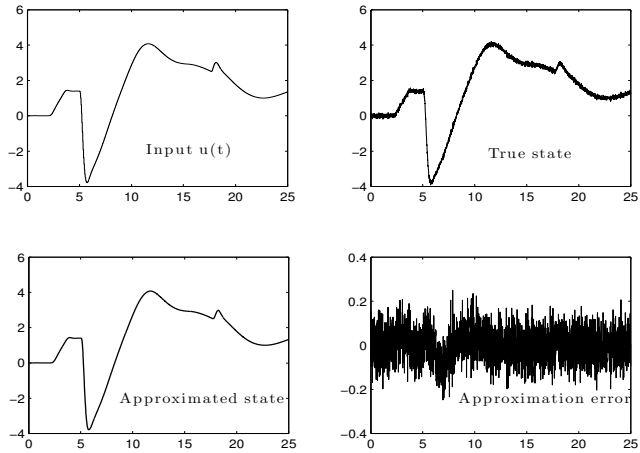

Figure 5.2. *Validation of simplified model a) system input, b) full model output, c) simplified model output and d) simplification error)*

For this reason, constant values are also chosen for the perturbations in the solid and liquid failure models [5.2] and [5.3]. In the following, the isolation of an oscillation of 0.5 degree amplitude and 1.5 Hz frequency will be considered as a case study. More generally, this case corresponds to an oscillatory failure signal $S_{def}(t)$ (for liquid and solid failures) described by:

$$S_{def}(t) = A \sin(2\pi f.t) \quad [5.5]$$

The whole FD procedure summarized in Table 5.2 is applied, using the model of oscillatory failure signal [5.5] with the failure models [5.2] and [5.3]. The amplitude range of the faults is from 0.5 to 1 degree and their range of frequency is from 0.5 to 12 Hz (the sampling period for data acquisition is 0.01s).

5.4. Fault detection by standard deviation test

5.4.1. *Residual generation*

As shown in Figure 5.3, with the actual measurement x of the CS position and the outputs corresponding to the three operating modes of the system, three residuals are obtained from the simplified models M_b, M_s and M_ℓ by:

$$r_\lambda(t) = x(t) - x_\lambda(t), \lambda \in \{b, s, \ell\} \quad [5.6]$$

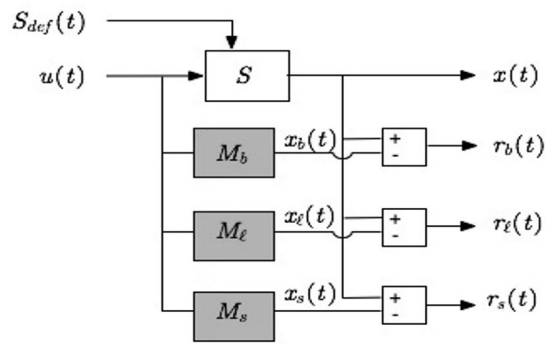

Figure 5.3. *Bank of residual generators for failure detection*

Figure 5.4 represents the residuals $r_b(t)$, $r_s(t)$ and $r_\ell(t)$ in the fault free case. In the absence of failure, model M_b really fits this situation, the amplitude of the residual $r_b(t)$ is clearly limited to approximately 0.2 *degree*; whereas residuals $r_s(t)$ and $r_\ell(t)$ oscillate with a significantly greater amplitude that is justified by the fact that the models M_ℓ and M_s do not accurately describe the fault free behavior of the system.

Two other situations are also considered: Figure 5.5 (*respectively,* Figure 5.6) represents the residuals in the case of liquid failure (*respectively,* solid failure). The failure is simulated between 5.3 and 15.3 s. In this time interval, the variation amplitude of the residue $r_b(t)$ increases and the variation amplitude of the residue $r_\ell(t)$ (*respectively,* residue $r_s(t)$) decreases in the presence of the liquid failure (*respectively,* solid failure). These residues are used for the FDI procedure, the signatures of the residues being clearly distinguished according to the type of failure. Table 5.3 relates to the theoretical signatures and gives the impact of the operating modes on the three residuals.

	fault free	liquid failure	solid failure
r_b	0	1	1
r_ℓ	1	0	1
r_s	1	1	0

Table 5.3. *Fault signatures*

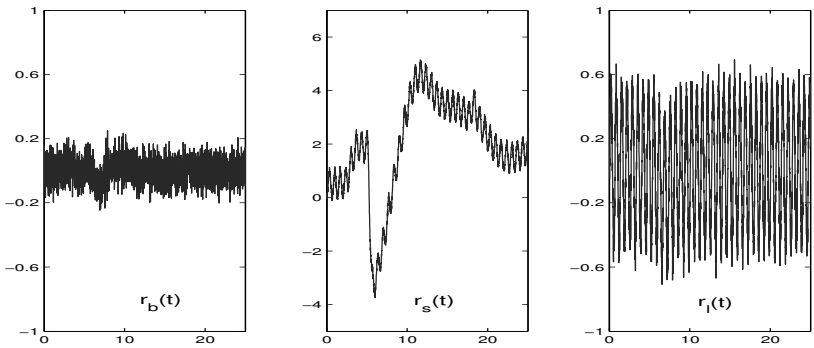

Figure 5.4. *Residuals $r_b(t)$, $r_s(t)$ and $r_\ell(t)$: fault free case*

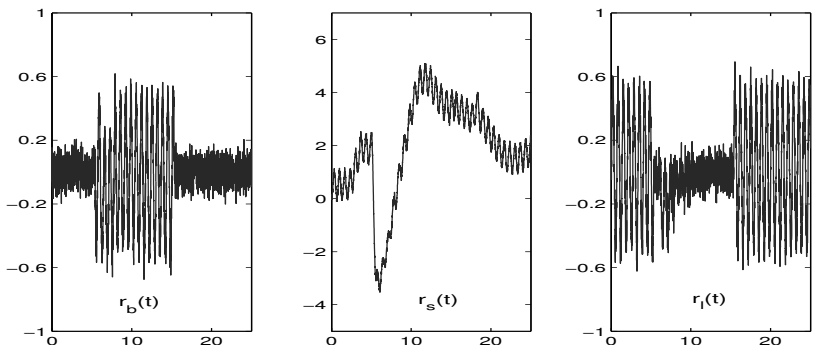

Figure 5.5. *Residuals $r_b(t)$, $r_s(t)$ and $r_\ell(t)$: case of liquid failure*

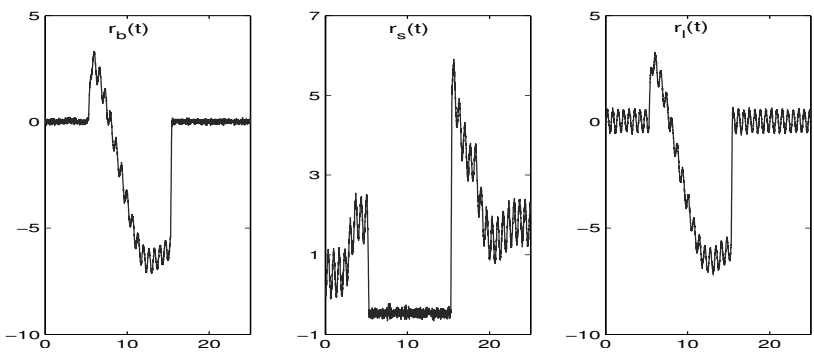

Figure 5.6. *Residuals $r_b(t)$, $r_s(t)$ and $r_\ell(t)$: case of solid failure*

In the so-called incidence matrix or fault signature matrix of [5.3], an (i, j) entry equal to 1 indicates that the i^{th} residual responds to the j^{th} failure, while an entry equal to 0 means that it does not [GER 91]. At each time instant, this table is used to recognize the situation. For example, if at a given time instant the observed signature is $[1\ 0\ 1]$, the Hamming distance between the Boolean residual vector and the different columns of the incidence matrix will be $[2\ 0\ 2]$. Finding the smallest distance allows us to deduce that the liquid failure situation has occurred.

The previous qualitative visual study showed the ability of three residues to easily recognize the actual operational situation. In section 5.4.2, the quantitative analysis of residues confirms this study and shows how the recognition is automatically processed from a numerical point of view.

5.4.2. *Generation of failure indicators*

With the residuals generated from the three operating models, the procedure for detecting and isolating faults reveals to be quite simple to implement. The principle is that, based on the detection of amplitude variations of the residues, any sudden change can be interpreted as a change in operating mode. The standard deviation measures the dispersion of data set around its mean value, its variations may indicate the occurrence or disappearance of a failure. For a residue $r(t)$, this deviation may be calculated (with the discrete time k) over a sliding window of appropriate width N as follows:

$$\begin{cases} \sigma_{r_\lambda}(k) = \sqrt{\frac{1}{N-1} \sum_{m=k-N+1}^{k} (r_\lambda(m) - \overline{r}_\lambda(k))^2} \\ \overline{r}_\lambda(k) \ = \frac{1}{N} \sum_{m=k-N+1}^{k} r_\lambda(m) \end{cases} \qquad [5.7]$$

This assessment is carried out on residuals (r_λ, $\lambda = b, s, \ell$) from the failure-free model M_b and the failure models M_s and M_ℓ. It is well known that the computation of the standard deviation may be performed using a recursive formulation in order to lighten the computational burden in online applications. Another possibility, allowing a significant reduction of computation, is to use an exponentially weighted expression of the mean and the standard deviation of the residuals.

5.4.3. *Failure detection by standard deviation test*

Due to residual deviations, the detection of the operating mode and therefore failure may be performed as summarized by the algorithm 5.1. The principle of this algorithm is to evaluate the relationship between the calculated deviations over sliding windows of appropriate dimensions with the initial deviations (calculated in the absence of failure).

ALGORITHM 5.1.– Failure detection by standard deviation test

1) Initialization: calculate the initial deviations $\sigma_{b,0}$, $\sigma_{\ell,0}$ and $\sigma_{s,0}$ from data collected in the failure free mode.

2) Calculate the deviations $\sigma_\lambda(k)$, from [5.7] over sliding windows and the normalized deviations by: $r_{n\lambda}(k) = \sigma_\lambda(k)/\sigma_{\lambda,0}$, for $\lambda = b, s, \ell$

3) Onset of failure: if the failure was not yet detected and if $r_{nb}(k) \geq 2$ on a significative time interval, the model M_b does not reflect the present situation. Moreover:

- if $r_{n\ell}(k) \leq 0.5$, then the occurrence of the liquid failure is confirmed;
- if $r_{ns}(k) \leq 0.5$, then the occurrence of the solide failure is confirmed.

4) Disappearance of the failure: if a failure has already been detected and if, on a significative time interval, the following inequalities hold:

- $r_{nb}(k) \leq 1.5$, $r_{n\ell}(k) \geq 0.75$ and $r_{ns}(k) \geq 0.75$

then the disappearance of the failure is confirmed.

Obviously, the quantities $0.5, 0.75, 1.5$ and 2, used for thresholding the normalized residual standard deviations, should be considered as parameters to be set according to the admissible level of false alarms and also to the different flight scenario. The length of the sliding window is also a parameter that must be adjusted according to tradeoff between delay of detection and insensitivity to measurement noise.

The result of failure detection by the algorithm 5.1 is illustrated by Figures 5.7, 5.8 and 5.9 for the failure free case, the liquid case and the solid case, respectively. As previously, the failure affects the system between 5.3 s and 15.3 s and is considered at the particular frequency 1.5 Hz.

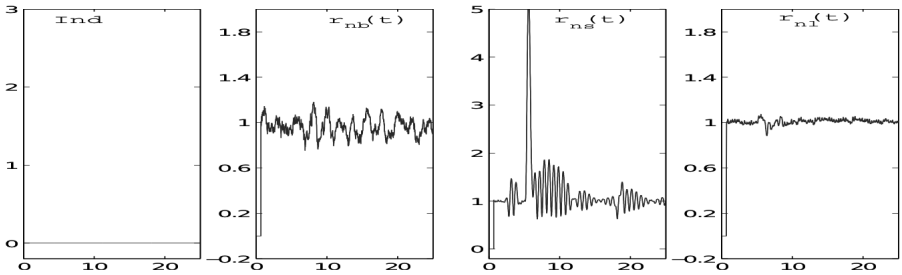

Figure 5.7. *Automatic fault detection: failure free case*

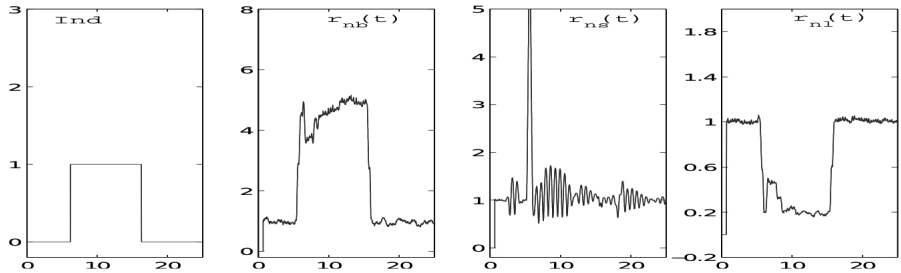

Figure 5.8. *Automatic fault detection: case of liquid failure*

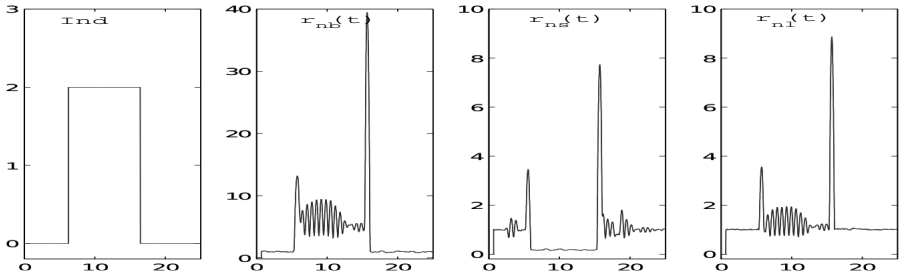

Figure 5.9. *Automatic fault detection: case of solid failure*

On each figure, the failure flag noted `Ind` is one if the liquid failure is detected, two if the solid failure is detected and zero if no failure is detected. The quantity r_{nb} (*respectively,* $r_{n\ell}$ and r_{ns}) is the ratio between the calculated deviation on $r_b(t)$ (*respectively,* $r_\ell(t)$ and $r_s(t)$) and the initial standard deviation $\sigma_{b,0}$, $\sigma_{\ell,0}$ and $\sigma_{s,0}$. This definition justifies the values taken by these ratios around the value 1 for normal operating conditions. The analysis of the different graphs, i.e. the deviation of the quantity r from its normal value 1,

clearly leads to the successful conclusion of situation recognition, in all cases we have analyzed the detection of liquid or solid failure is unambiguous. As explained in section 5.4.1, a fault matrix signature is used to recognize at each time instant the operating mode. Using the definition of the ratio r, Table 5.4 has been constructed, in which element 1 indicates that the residual does respond to the failure, while 0 means that it does not. When using noisy data, fault isolation may become difficult. To prevent errors in the fault isolation procedure, we need to use a specific coding of the signatures such that no degrading code is identical to a valid code. It is the case of the signatures in Tables 5.3 and 5.4 that are different, but the two set of signatures are strongly isolating, according to the classical terminology [GER 91].

	free fault	liquid failure	solid failure
r_b	0	1	1
r_ℓ	0	0	1
r_s	0	1	0

Table 5.4. *Fault signatures*

5.4.4. *Discussion on failure detection by standard deviation test*

The outcomes of algorithm 5.1 show that the failure is detected and identified at approximately 1.0 oscillation periods after its occurrence (0.89 s for the liquid failure case and 0.93 s for the solid failure case). This result is compliant with the required specifications of this case study, that is to say the detection time.

If we focus only on the failure detection (without isolation), then the test of standard deviation of the residual $r_b(k)$ is sufficient, without using the two failure models. In this case, the failure detection condition should be reduced to $r_{nb}(k) \geq 1.75$ for a period of time (algorithm 5.1). The different examples show that we can detect any solid and liquid failure on the frequency range $[0.5 \ldots 10.0]$ Hz even at very low amplitude (0.16 degree).

However, if the goal is not only to detect but also to isolate all failures that may appear in the control loop, the three models need to be used. Moreover, the frequency of oscillation to be detected is not known a priori, but only its range of variation is known.

Thus, several frequencies are to be considered in the pattern of oscillation S_{def} [5.5] because the failure models M_s [5.2] and M_ℓ [5.3] depend on this frequency. The number of failure models described by equations [5.2] and [5.3] must be increased and therefore different frequencies of oscillations must be taken into consideration. Each failure model whose parameters are fixed is specific to a particular solid or liquid failure (of type [5.5]). With the principle used by the algorithm 5.1, any solid and liquid failure characterized by a frequency in $[0.5 \dots 10.0]$ Hz and an amplitude in $[0.5 \dots 1.0]$ $degree$ can be detected and isolated for many flight scenarios. This procedure has been developed and successfully tested on different flight situations.

However, to reduce the number of failure models, another approach is to use a correlation test that is developed in section 5.5.

5.5. Fault detection by correlation test

The dysfunction models [5.2] and [5.3] allow us to study the behavior of the system in the presence of a failure, liquid or solid. When simulating the dysfunction models, the impact of the failure on the output can be directly identified and estimated by forcing the command to zero. In this way, patterns of failures can be generated offline to be compared to the residue $r_b(t)$ or output $x(t)$ to detect and isolate the failure.

Figure 5.10 shows the procedure to be implemented. The first residue $r_b(t)$, generated by the model M_b has already been defined. Signals $f_i(t)$ correspond to failures [5.5] characterized by some specific frequencies (0.5 Hz, 1.5 Hz, 7 Hz for example) whose effect is assessed based on the failure models M_ℓ thus generating signatures $x_{Li}(t)$ specific to each of these frequencies. It is important to note that $x_{Li}(t)$ only reflects the influence of the i^{th} failure, since the input u is not applied to the model M_ℓ. Moreover, by construction, residual $r_b(t)$ is also insensitive to $u(t)$ but reflects the influence of the fault f_i if it is present. Such frequencies are called "selected" because this work aims at detecting and isolating the failures of these frequencies. These signatures are then compared (by correlation over sliding windows) to the previously evaluated residue $r_b(t)$ or output $x(t)$. This principle applies to liquid failure with model M_ℓ as indicated in Figure 5.10. The same procedure is applied for solid failure with model M_s.

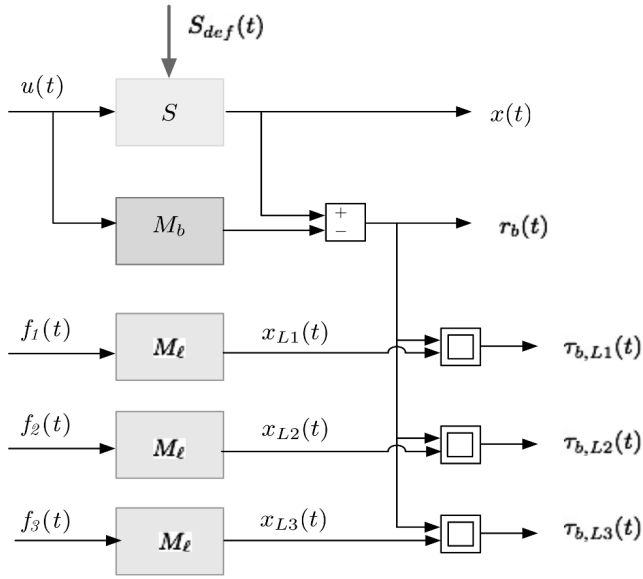

Figure 5.10. *Generation of residues for correlation test. Case of liquid failure*

5.5.1. *Pattern generation*

In this subsection patterns at $0.5\ Hz$, $1.5\ Hz$ and $7.0\ Hz$ are generated from models M_s and M_ℓ by putting the command to zero. As the correlation test does not distinguish the amplitudes of sinusoidal signals, these patterns are generated so that they correspond to the oscillation of $0.75\ degree$. Each pattern is a sequence its length is equal to two periods of the failure of given frequency. The objective of the present case study is to detect and to isolate the three failures $f_i(t) = 0.75sin(2\pi\nu_i.t)$ for the frequencies $\nu_1 = 0.5\ Hz$, $\nu_2 = 1.5\ Hz$ and $\nu_3 = 7.0\ Hz$.

5.5.1.1. *Patterns of liquid failures*

Considering the liquid failures, the three following patterns are generated (Table 5.5) with a sampling period of 0.01 s. These three patterns x_{L1}, x_{L2} and x_{L3} are presented in Figure 5.11. They will be used in correlation tests with the signal $r_b(t)$ previously defined by $r_b(t) = x(t) - x_b(t)$.

As explained before, the patterns x_{L1}, x_{L2} and x_{L3} are the direct impacts of liquid failures on the output of the system and they are comparable in some way with the residue $r_b(t)$ under the presence of a failure. Indeed, the difference

$x(t) - x_b(t)$ reflects the impact of the failure on the output since the effect of the command $u(t)$ on $x(t)$ and $x_b(t)$ is canceled by the difference.

Pattern	Sequence	Frequency
x_{L1}	400 samples	0.5 Hz.
x_{L2}	134 samples	1.5 Hz.
x_{L3}	29 samples	7.0 Hz.

Table 5.5. *Liquid failure pattern characteristics*

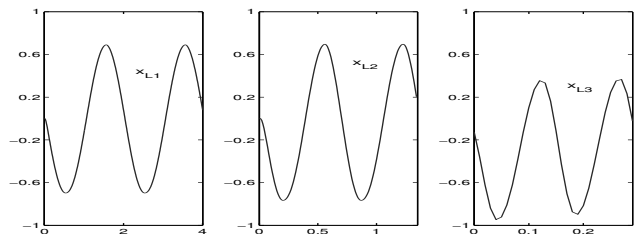

Figure 5.11. *Patterns x_{L1}, x_{L2} and x_{L3}*

Pattern	Sequence	Frequency
x_{S1}	400 samples	0.5 Hz.
x_{S2}	134 samples	1.5 Hz.
x_{S3}	29 samples	7.0 Hz.

Table 5.6. *Solid failure pattern characteristics*

5.5.1.2. *Patterns of solid failures*

For the solid failures, the three following patterns are generated (Table 5.6). These three patterns x_{S1}, x_{S2} and x_{S3} are presented in Figure 5.12. They are analyzed by correlation test with $r_b(t)$.

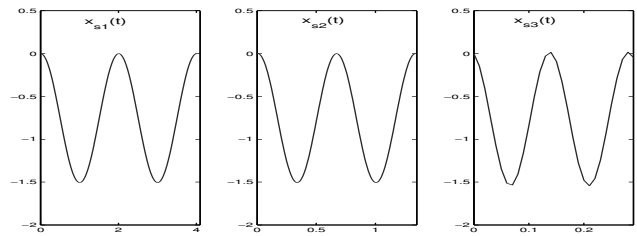

Figure 5.12. *Patterns x_{S1}, x_{S2} and x_{S3}*

5.5.2. *Failure indicator generation and fault detection by correlation test*

The correlation between two or more variables, such as r_b and x_{Li} is the intensity of the relation that may exist between these variables. A measure of this correlation is obtained by the calculation of the linear correlation coefficient. The linear correlation coefficient between two variables r_b and x_{Li} is denoted by $\tau_{b,Li}$.

With the correlation test, FD can be performed as summarized in Algorithm 5.2. The principle of this algorithm is to compute the linear correlation coefficients over a sliding window, on the one hand between the residue $r_b(t)$ with signals x_{L1}, x_{L2} and x_{L3} that represent liquid failures; on the other hand between the output $x(t)$ with signals x_{S1}, x_{S2} and x_{S3} that represent solid failures. If one of these coefficients calculated over a sliding window remains bigger than a given threshold for N sample times, then a failure is detected.

ALGORITHM 5.2.– Fault detection by correlation test

1) Initialization:

- Read the patterns for the liquid failure x_{L1}, x_{L2} and x_{L3}

- Read the patterns for the solid failure x_{S1}, x_{S2} and x_{S3}

- Define the vector of pattern sizes $p = [400,\ \ 133and\ \ 29sample]$

- Chose one threshold as for example $V_s = 0.6$.

2) Perform calculations of linear correlation coefficients for each k^{th} sampling step:

- Calculate the correlation for liquid failure $\tau_{r_{b(k-p(i)+1:k)},x_{Li}}$ for $i = 1, 2, 3$.

- Calculate the correlation for solid failure $\tau_{x_{(k-p(i)+1:k)},x_{Si}}$ for $i = 1, 2, 3$.

3) Evaluate the linear correlation coefficients by counting the overshots:

- If a correlation coefficient is greater than V_s or smaller than $-V_s$, the number of so-called *overshot* associated with this coefficient is increased by one unit.

- If no overshot is observed within a limited time window, the number of overruns is set to zero.

4) Onset of failure: if the failure has not yet been detected and if one of the overruns is greater than or equal to 4; then:

- the onset of failure is confirmed;

- the nature of the failure (liquid or solid) as well as its frequency are indicated by the pattern x_{Li} or x_{Si} whose number of overshot was observed with its correlation coefficient. If it is a pattern x_{Li}, the failure is liquid; if it is a pattern x_{Si}, the failure is solid. The value of i (1, 2 or 3) indicates the frequency of the failure.

5) Disappearance of the failure: if a failure has already been detected and no exceedance was observed within a limited time window, then:

- the failure is declared to have disappeared.

The correlation coefficients calculated over a sliding window are shown first in Figure 5.13 for the case without failure. The result of failure detection by the algorithm 5.2 is shown in Figures 5.14, 5.15 and 5.16. Figure 5.14 (*respectively,* 5.15 and 5.16) represents the result obtained with the liquid failure of 0.5 Hz frequency (*respectively,* the liquid failure of 1.5 Hz frequency and with the solid failure of 7.0 Hz frequency). Failures are simulated between 5.3 and 15.3 s.

The first column represents the correlation coefficients that led to the failure detection ($\tau_{r_b,x_{L1}}$, $\tau_{r_b,x_{L2}}$ and $\tau_{x,x_{S3}}$ respectively). The indicator of nature of the failure is denoted by `Nat` in the second column. If `Nat` = 1, a liquid failure is detected, if `Nat` = 2, a solid failure is detected, and `Nat` = 0 is used in the failure free case. The frequency of the failure is indicated in the third column. With this method, the detection and isolation of failure can be performed in less than three periods of the failure, which is in fact compliant with the required specifications of the case study. More precisely, frequency 0.5 Hz corresponds to period of 2 s. In Figure 5.14, the detection and the recognition of the failure is performed at 10 s, i.e. with a delay of 4.7 s. which is less than three periods of the failure. The same analysis should be done for the two other cases.

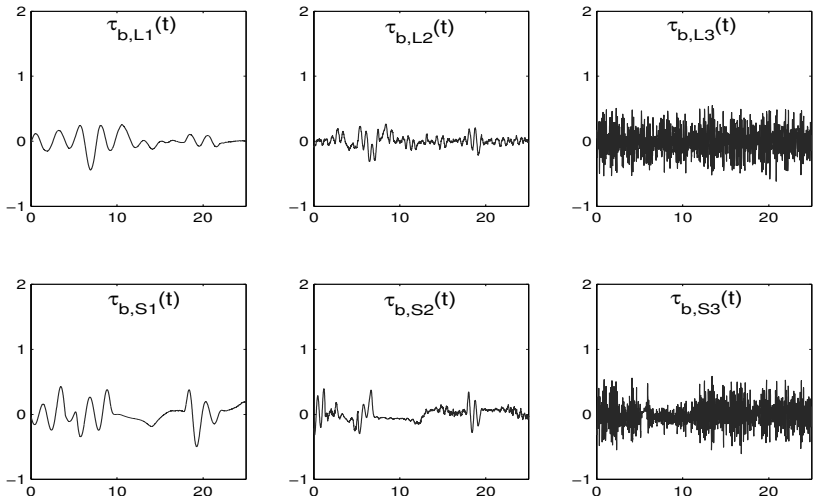

Figure 5.13. *Calculated correlation coefficients: failure free case*

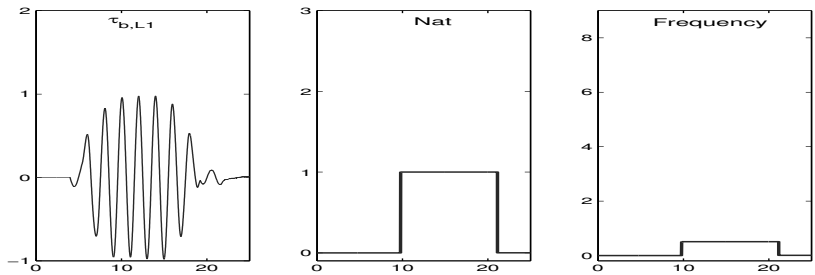

Figure 5.14. *Result of detection: liquid failure of 0.5 Hz frequency*

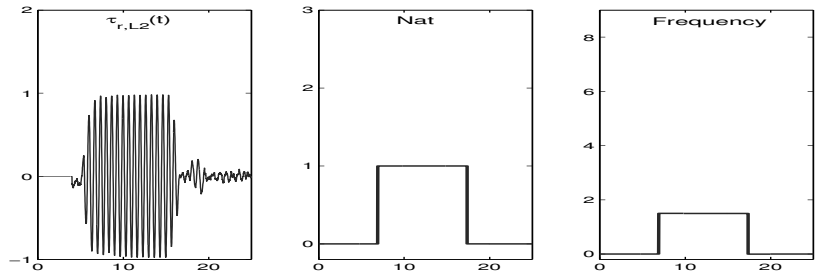

Figure 5.15. *Result of detection: liquid failure of 1.5 Hz frequency*

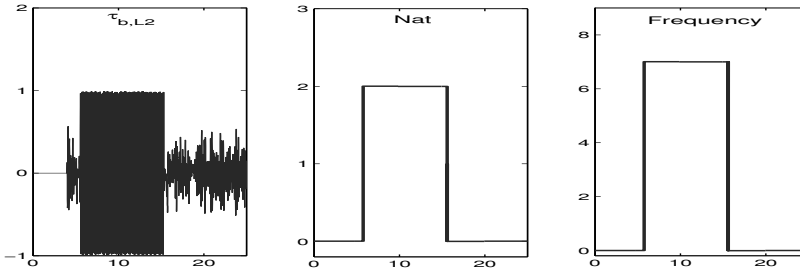

Figure 5.16. *Result of detection: solid failure of 7.0 Hz frequency*

5.5.3. *Discussion on the failure detection by correlation test*

The failure detection by correlation test has significantly reduced the number of failure models compared to the deviation test. In fact, embedding only the failure-free model in flight control computer to generate the residue $r_b(t)$ is sufficient. All the pattern describing liquid and solid failures are generated in advance and stored. Thus, the online computation task is easy to perform. Different treated flight scenarios show that any solid and liquid failure characterized by frequencies in the frequency range $[0.5 \ldots 10.0]\ Hz$, even at low amplitude ($0.16\ degree$) can be detected and isolated. However, this analysis does not estimate the amplitude of the failure. It should be noted that in its current version, algorithm 5.2 uses six correlation tests at every step of simulation (two types of default, three selected frequencies). Although the calculations are simple and only need basic operators, it is possible to substantially reduce the computational load in the following ways:

– the patterns x_{L1}, x_{L2}, x_{L3}, x_{S1}, x_{S2} and x_{S3} are determined by the type of failure. Their means and standard deviations over a window can be calculated offline and stored;

– means, standard deviations of the output $x(t)$ and the residue $r_b(t)$ calculated over a window can be performed recursively when moving a step time of the observation window;

– the covariance, and consequently the correlation, between a reference pattern and a signal $x(t)$ or $r_b(t)$ over a window can also be calculated in recursive way, since correlation does not take into account these amplitudes;

These recurrences are easy to establish, so the correlation tests can be carried out with a reasonable computational load.

5.6. Conclusion

This chapter addresses the problem of detecting the oscillatory failure in the control system of a control surface of a civil aircraft. Two fault detection methods are proposed, based on a simplified model validated regarding the nonlinear models usually used. Any solid and liquid failure in the frequency range $[0.5 \ldots 10.0]$ Hz can be detected by standard deviation test, as well as any solid and liquid failure of selected frequencies by correlation test. Both methods have been successfully tested for a variety of flight scenarios, even with failures of low amplitude (0.16 degree). Future works will consist of extending these methods to other control surfaces (rudder or elevator), by trying to reduce the complexity as well as the number of failure models. The improvement of the robustness of the correlation test for the failures of frequencies neighboring the selected ones is also to be considered.

5.7. Acknowledgments

The authors would like to thank the French Research Foundation for Aviation and Space, for its support to the SIRASAS project. https://extranet.ims- bordeaux.fr/External/SIRASAS/

5.8. Bibliography

[ALW 11] ALWI H., EDWARDS C., "Oscillatory failure case detection for aircraft using an adaptive sliding mode differentiator scheme", *American Control Conference (ACC), 2011*, IEEE, pp. 1384–1389, 2011.

[CIE 13] CIESLAK J., EFIMOV D., ZOLGHADRI A., *et al.,* "Oscillatory failure case detection for aircraft using nonhomogeneous differentiator in noisy environment", *2nd CEAS Specialist Conference on Guidance, Navigation & Control*, Delft, Pays-Bas, April 2013.

[DAS 00] DASH P., JENA R., PANDA G., *et al.*, "An extended complex Kalman filter for frequency measurement of distorted signals", *IEEE Transactions on Instrumentation and Measurement,* vol. 49, no. 4, pp. 746–753, 2000.

[GER 91] GERTLER J., "Analytical redundancy methods in fault detection and isolation; survey and analysis", *IFAC International Symposium on Fault Detection, Supervision and Safety for Technical Processes*, vol. 1, pp. 9–21, 1991.

[GOU 10] GOUPIL P., "Oscillatory failure case detection in the A380 electrical flight control system by analytical redundancy", *Control Engineering Practice*, vol. 18, no. 9, pp. 1110–1119, 2010.

[HE 07] HE Q.P., WANG J., POTTMANN M., *et al.*, "A curve fitting method for detecting valve stiction in oscillating control loops", *Industrial & Engineering Chemistry Research*, vol. 46, no. 13, pp. 4549–4560, 2007.

[JER 03] JERAM G.J., PRASAD J., "Fuzzy logic detector for aircraft pilot coupling and pilot induced oscillation", *The 59th American Helicopter Society Annual Forum*, vol. 59, American Helicopter Society, Inc, pp. 1204–1211, 2003.

[KIM 03] KIM K.-S., LEE K.-J., KIM Y., "Reconfigurable flight control system design using direct adaptive method", *Journal of Guidance, Control, and Dynamics*, vol. 26, no. 4, pp. 543–550, 2003.

[LAV 08] LAVIGNE L., ZOLGHADRI A., GOUPIL P., *et al.*, "Robust and early detection of oscillatory failure case for new generation Airbus aircraft", *The AIAA Guidance, Navigation and Control Conference and Exhibit*, 2008.

[MAR 12] MARTON L., OSSMANN D., "Energetic approach for control surface disconnection fault detection in hydraulic aircraft actuators", *IFAC International Symposium on Fault Detection, Supervision and Safety of Technical Processes*, vol. 8, pp. 1149–1154, 2012.

[MIT 04] MITCHELL D., KLYDE D., "*Recommended Practices for Exposing Pilot-Induced Oscillations or Tendencies in the Development Process*", American Institute of Aeronautics and Astronautics, 2004.

[SIF 12] SIFI M., LAVIGNE L., CAZAURANG F., *et al.*, "Oscillatory failure detection in flight control system of civil aircraft: EHA actuator servo loop case study", *5th International Conference on Recent Advances in Aerospace Actuation Systems and Components (R3ASC '12)*, Toulouse, France, June 2012.

[SUN 12] SUN X., PATTON R.J., GOUPIL P., "Robust adaptive fault estimation for a commercial aircraft oscillatory fault scenario", *UKACC International Conference on Control (CONTROL)*, IEEE, pp. 595–600, 2012.

[TRI 10] TRINH D.-H., MARX B., GOUPIL P., *et al.*, "Design of a soft sensor for the oscillatory failure detection in the flight control system of a civil aircraft", *2010 IEEE International Symposium on Industrial Electronics (ISIE),* IEEE, pp. 2061–2066, 2010.

[VAR 12] VARGA A., OSSMANN D., "LPV-model based identification approach of oscillatory failure cases", *IFAC International Symposium on Fault Detection, Supervision and Safety of Technical Processes*, vol. 8, pp. 1347–1352, 2012.

6

Embedded Sensors for the Analysis of Drivers' Behavior

This research was carried out as part of the French national multidisciplinary research project PREDIT-SARI. A theme has been developed to study the visibility of the road in dangerous portions, particularly crossroads, bends and the coastal summits in a straight line. The aim of our study was to develop a diagnostic tool and a methodology to test the effectiveness of road treatments with these summits. The embedded sensors in the road make an analysis of the trajectories followed by drivers possible.

6.1. Introduction

Before the development of the research project called Automated Road Surveillance for Drivers' and Administrators' Information (SARI), the Maine-et-Loire departmental council office in charge of roads and transportation defines the area where the study has taken place. The defined area is the departmental road 961 (RD 961) from Marans to Segré where a large number of accidents had been observed and for which no tangible proof had been found to explain their frequency.

For instance, between 1998 and 2000, four accidents, objects of an official report, were noted but they remained difficult to explain. In most cases, they were accidents involving only one vehicle. The area has the

Chapter written by Patrick PLAINCHAULT, Sébastien AUBIN, Patrice BRIAND, Jean-Michel AUBERLET and Thierry BOSCH.

specificity of being in a straight line with a summits coast, a specificity that is common to Maine-et-Loire (49) department road network, and that counts a lot of unexplained and regrettable accidents. This road topology is little studied despite the fact that many departments, such as Maine-et-Loire and its 2,800 miles of departmental roads, show a significant frequency of this topology.

According to studies completed between 2000 and 2004, this area shows an average daily traffic of 3,300 cars. An inquiry established in 2007 reports a daily rate of around 1,900 vehicles for each road lane in this area; in other words, there is a 15% growth in traffic in over 3 years. The readers should take into account that although there is a summit hill, the lane's width is only 3 m at this high point. The longitudinal profile is shown in Figure 6.1.

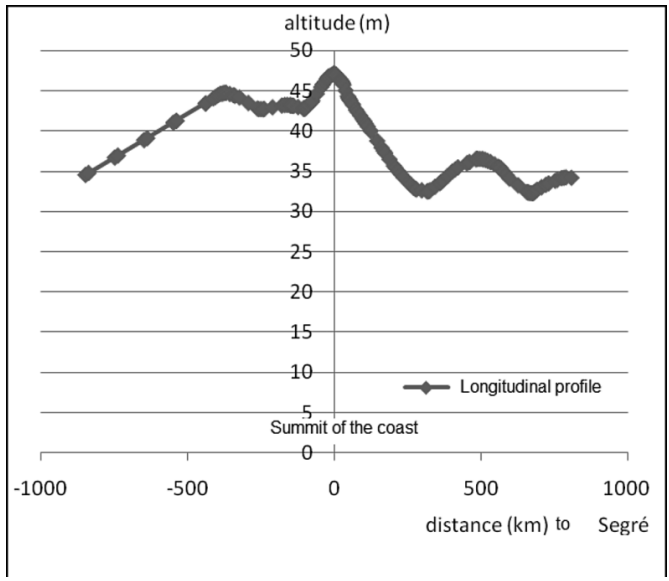

Figure 6.1. *RD961 longitudinal profile from Marans to Segré (1 km from observation)*

As part of our contribution to the SARI program, Intelligent Vision of Potentially Dangerous Areas and Itineraries (VIZIR) was meant to examine the impact of a development on the position of a vehicle on the road.

Therefore, over a first phase (the analysis before the development), the drivers' trajectories were observed. Then, several developments were created:

– rumble strips as central road markings to alert drivers;

– rumble strips as central road markings to alert drivers and the hard shoulder;

– finally, the hard shoulder only.

After each development, a period of the listings of the drivers' trajectories was studied (the analysis after the development). Therefore, compared to the analysis before the development, it was possible to show the development's impact on the vehicle's trajectories.

In this chapter, we will mainly try to present the different embedded sensors on the road, the selected organization for the sensors' deployment, the communication network connecting these different points of measurement and the supervisor. Finally, some results will be pointed out concerning the extent of development's impact, due to the use of this observatory.

6.2. Trajectories' observatory

The study of the vehicles' trajectories is the only valid way to reveal the drivers' behavior. The ideal tool would be to continuously follow these trajectories on the road section concerned. Assuming that the use of a camera device would be too intrusive for the driver, we have therefore resorted to sensors that are distributed and integrated into the road surface; it allows samples of trajectories to be taken and trajectories tracked. Indeed, the acuteness of the selection of samples depends on the number of sensors installed. All vehicles will be located on the trajectory studied, through their longitudinal and lateral positions. Thus, two different types of precision are contemplated and taken into consideration: longitudinal precision and lateral precision. The precision of the sensor's lateral data, indicated by recent technologies, is decametric [AUB 06, KLE 01]. Some sensors displayed in our observatory are able to reach a centimetric lateral precision.

6.2.1. *Trajectory*

In the road traffic field, the car's trajectory is mathematically defined as "a continuing function of R+ in R^3 which at any time *t* associates the position in the car's centre of gravity's space represented by a point" [DAU 08]. In this case, the Cartesian/rational reference source associated with the road is the most convenient point of reference to characterize it.

Nevertheless, this function has to be at least of order C^2 (twice differentiable) because the continuity of the speed and the acceleration has to be taken into account. In practice, it is difficult to know the car's speed without using sensors placed in the same car. This is the reason why a once differentiable function has been chosen.

6.2.2. *The measurement*

Restrictions imposed by our trajectories' study directed us toward using sensors embedded in the road. These sensors, which will be detailed in the following section, provide punctual measurements. Therefore, it seems necessary to deal with these measurements as a sample of continuous variables in time.

Regardless of the sensors' type, generally it is difficult to obtain the same precision laterally and longitudinally in relation to the road. Due to recent technologies, lateral precision is decametric, but to study the vehicles' trajectories, it is desirable to reach centimetric precision. It will be demonstrated that longitudinally it is not fundamental to have a sensor at each centimeter (see Table 6.1, where distance is covered depending on the angle of turn).

6.2.3. *Bragg fibers*

This sensor is based on a series of fibers of a Bragg network [FER 06]. The principal feature of Bragg fibers lies in the local variation of the index of the core of optic fiber of less than 1 cm length. Bragg fibers behave as a spectral mirror on a given Bragg wavelength. An enlargement of the grating creates the Bragg wavelength's variation.

A fiber optic with a Bragg grating – solicited by the pressure exerted by the passage of a car – is therefore extended to modify the internal structure of the fiber and the Bragg wavelength. By detecting this wavelength's variation, we are able to determine the Bragg fiber network concerned by this constraint and therefore able to go back to their spatial position on the fiber which thus corresponds to the vehicle's position (see Figure 6.2).

In this application, we are only interested in the wavelength's shift inferred by the stress exerted on the fiber optic. The other features of Bragg fibers, the alteration of the optical amplitude, the temporal response, etc., are not used.

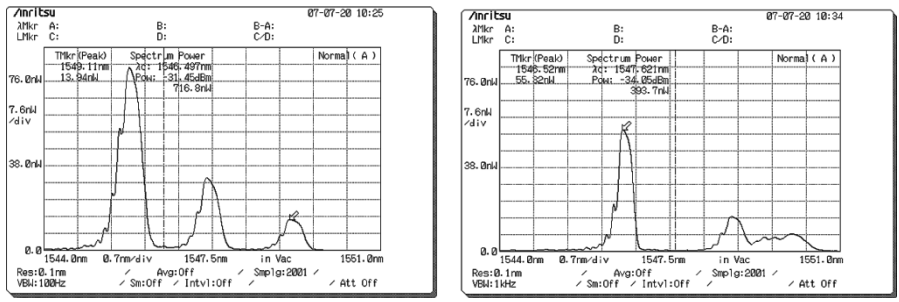

a) b)

Figure 6.2. *Spectrum of a three Bragg fiber network a) before constraint and b) after constraint*

In order to measure a lane of 3 m wide with a centimetric definition, 300 different wavelengths are needed on a fiber with networks placed every centimeter. Technically, this setup is not feasible both because of the number of wavelengths to study and because of the number of gratings to photoregister. A solution of spatial multiplexing resolved the problem. Several fibers staggered spatially formed a single sensor. In order to limit the coast of this Bragg fiber sensor, its length has been limited to 1.30 m, equivalent to half a lane.

The fiber is placed into a 1.5 cm deep cut, which is filled up again with a specific resin adapted for the sensor's device and whose mechanical properties guarantee a good and safe transmission of the constraints induced

by the vehicle's tires. Bragg fiber gratings have been on the market for more than 10 years now; however, its use is the first to our knowledge in this kind of application. The study of this type of sensors was the subject of a specific thesis carried out by the ESEO's TRAME team [AUB 09].

6.2.4. *Resistive sensors*

Regarding the prohibitive cost of the making of the many sensors with Bragg technology placed – and that are needed for the area's study – it was decided to study a cheaper sensor: a resistive sensor. This sensor can be considered as a long potentiometer. A vehicle driving on this sensor changes its resistance. Therefore, the resistor's variation becomes a linear function of the car's lateral position on the road. The tests carried out reveal a precision below 1 cm. The resolution of the designed sensor only relies on the resolution of the electronic purchasing system.

This sensor and its implementation have been patented [PLA 07].

The electronic purchasing scheme is based on a Wheatstone bridge. A basic microcontroller performs the measurement. This simple device is made up of a material that is feasible and economic regarding energy-saving (around 50 mA under 12 V when non-optimized) and the use of electronic equipment (cheap component).

Placed into a cut of the width of the lane, and immersed into resin, it comes up to the road's tread level. Most of the time, it is positioned perpendicular to the car's direction. Due to this arrangement (the measurement is carried out from the edge), it is only necessary to measure the external right tire's limit, namely, the closest to the verge. In order to recognize the vehicle's width, some sensors have been positioned at a 30° angle to the direction of the car circulation; consequently, it is possible to observe the left tire's position and to find out the vehicle's width. This arrangement gives the knowledge of both the vehicle's width and its lateral position. As for the longitudinal position, it is provided at the system's installation. Two sensors sequentially placed, it allows the gain of details about the vehicle's speed (Figure 6.5).

Figure 6.3 illustrates the passage of two vehicles, with two axles of vehicle type (VL) separated by 2.2 s. The two vehicles' lateral positioning is given by the value of the voltage peak that corresponds to the passage of the front right-side wheel first (AVD1: 1.38 m; AVD2: 1.10 m) and then to the passage of the back right-side wheel (ARD1: 1.38 m; ARD2: 1.10 m). It is important to note that according to the basic measuring principle, the amplitude of the signal is directly proportional to the vehicle's lateral position.

In Figure 6.4, the two curves had been detached for reasons of readability. The passage of one vehicle on two sensors separated by 8 m is represented: the upper curve stands for the first sensor, while the lower curve pictures the second one. It took 0.44 s for the vehicle to cross the 8 m at 65.5 km/h. The distance between each axle is 3.2 m, and another chassis (the second vehicle's chassis) follows 3.8 m after the first one. The second chassis' distance between each axle is 1 m – each one on the same lateral position as the tops of the four peaks are equal (upper curve).

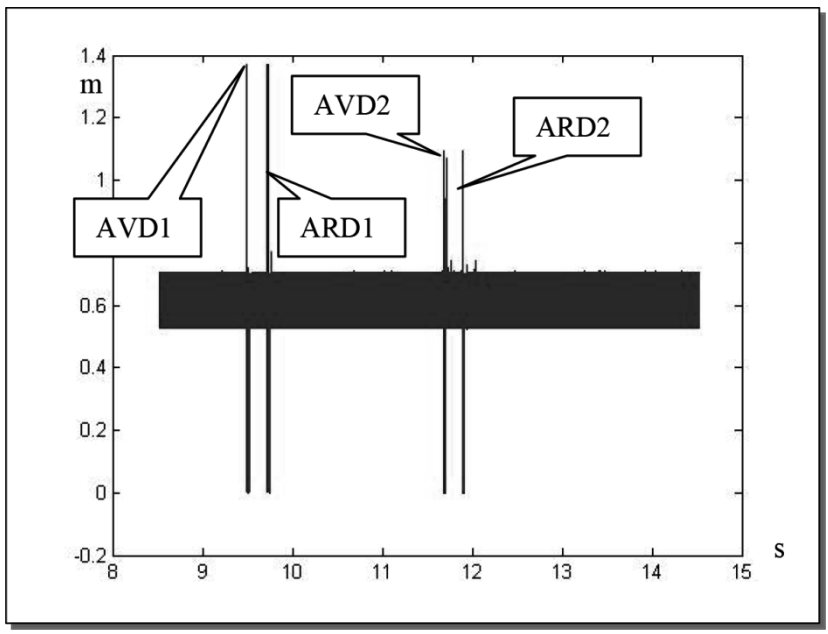

Figure 6.3. *Plotting of the two vehicles' passage on the same sensor*

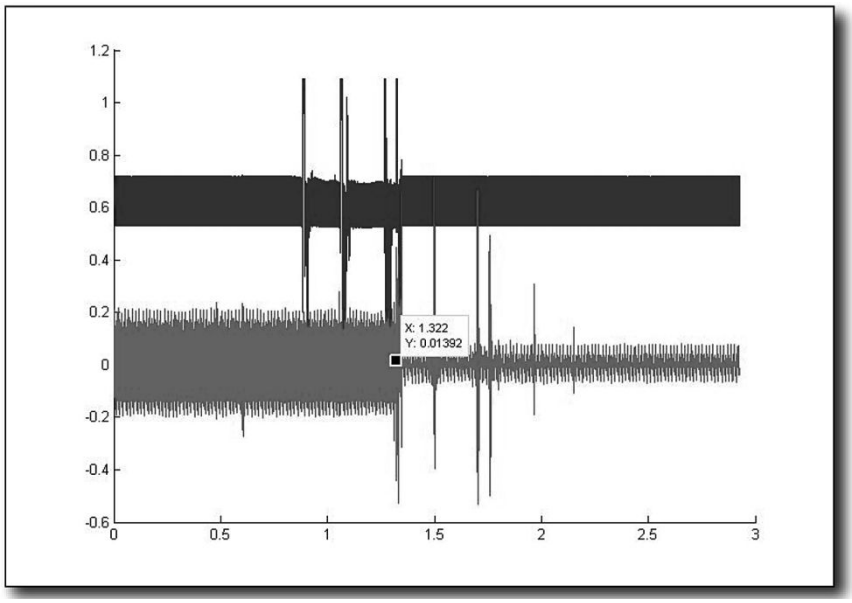

Figure 6.4. *Plotting of the two vehicles' passage on two different sensors placed 8 m away from each other*

6.2.5. *Electromagnetic loops*

Usually, electromagnetic loops are used in systems that detect vehicles' presence. This device is currently deployed to measure the vehicles' speed and/or to count passing vehicles in order to follow traffic progression.

Here, the electromagnetic loops are composed of an enameled wire rolled up in three rectangular coils (2 m × 1.5 m) and inserted into the road at a depth of 7 cm.

They are powered by an electronic oscillator of a 50–150 kHz frequency. This layout has been carried out by the Regional Laboratory of Highways, Angers. A specific positioning of the loops enables the measuring of the vehicles' lateral position with a 10 cm accuracy. The measuring precision for the speed is about 5%. Concerning the measurement of the vehicle's position, the variation's peak, related to each loop's inductance, has to be measured as well as its variation having to be compared by calculating their link.

6.3. The sensors' network

The area studied is 1 km of road, 500 m twice for each side of the summit. Sensors are roughly allocated symmetrically on the road. The road's lane from Marans to Segré is currently the only one fully equipped with sensors. The other lane only possesses electromagnetic loops (Figure 6.5).

6.3.1. *Spacing between the sensors*

As mentioned previously, the trajectory is sampled through several sensors. The sensors have to be arranged in order to obtain an interval of at least 1 cm in the trajectory. Several suggestions were sought to finally reach the desired goal.

A frequency suggestion is also worth considering. The vehicle's trajectory may be contemplated as periodical, with a zigzag shape [LEC 02]. Due to Shannon's theorem, we are able to know the distance between two sensors. Presupposing a 1 Hz zigzag frequency and a 25 m/s speed (90 km/h), a spacing of 12.5 m between the sensors is obtained. However, with Fourier's analysis, the signal's reconstruction needs more calculation.

A second suggestion involves the vehicle diverting from its initial straight trajectory, and performing a circular trajectory – the radius of the trajectory is close to the one which offers a maximal dynamic comfort approved by the driver for a 90 km/h speed [PLA 05]. By applying this theory to our study, the vehicle covers a distance depending on the 2.2 m road's leading axis, and then deviates from its original straight trajectory by more than 1 cm. Unfortunately, this dynamic comfort is not often complied in the event of an accident, implying that the distance between sensors must be less than this value.

In order to define more precisely this suggestion, the "bicycle" model was used [MOU 06]. This method gives a more realistic trajectory than the circular one. Some factors such as the "bicycle's" speed and its direction (or the sharp turn angle) are vital to get a result from the model (these factors constitute the command). Considering a speed between 15 and 31 m/s, as well as a sharp turn angle between 0.001 and 0.05 rad, the model was simulated by Matlab. To achieve a valid result, these starting factors were coordinated with real measures. They were selected after observing the

speeds and orders of magnitude of the wheel's sharp turn angles on several drivers in different situations (overtaking a vehicle, turning, driving in a straight line, etc.).

The speed had been set to be constant. At a certain moment, a sharp turn angle was applied on the models (initially equal to zero). The distance executed by the bicycle had also been studied (based on the roadway axis) when its lateral gap became greater than 1 cm. With a specific angle, the values are roughly constant (small error because of the calculation's steps).

Sharp turn angle (rad)	0.001	0.005	0.01	0.015	0.02	0.05
Executed distance (m)	12.77	6.38	4.64	4.06	3.48	2.32

Table 6.1. *Executed distance based on the sharp turn angle with a 29 m/s speed*

As the study deals with a straight line, a spacing of 4 m between the resistive sensors is sufficient. About 4 s of driving can be observed when 29 resistive sensors, as previously stated, are placed on 112 m. Assuredly a fact, if some vehicles were driving very slowly, the precision on their tracks would be lower. Nevertheless, it is relevant just to be reminded of the fact that the study's purpose was to notice the development's aftermath on the vehicle's position on the road.

6.3.2. *The sensor network's display*

The roadway on the Marans–Segré side has five electromagnetic loops: one on the summit and the remaining four on both sides of the hill with a set distance from the first one (meaning a 1 km total distance). The loops will allow us to obtain a first estimation of the speed and the vehicle's positioning before and after the hard spot. Twenty-nine resistive sensors spaced by 4 m supplement this development, giving a more precise value of the trajectory on the summit. Two sensors are placed before the resistive sensors (see Figure 6.5) to analyze the optic sensors' Bragg technology.

Every optic and resistive sensor's electronic cards are linked by the same communication bus: control area network (CAN bus). The loops are connected to a "detector" card. An RS422 connection relates this card to an

embedded computer/PC (CP8). Each CP8 studies the loop's data and provides a lot of information: the time stamping, the vehicle's category and its speed and position

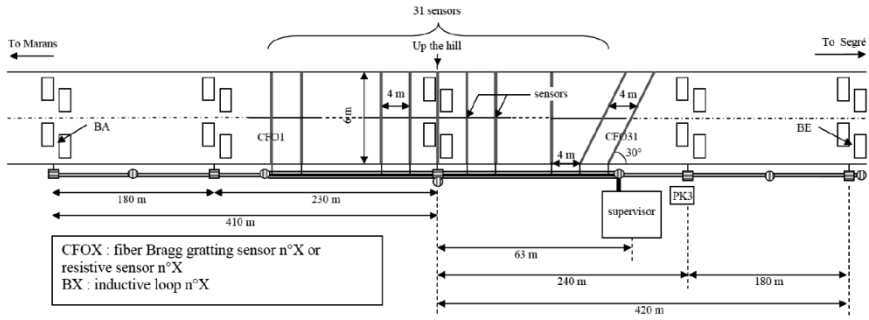

Figure 6.5. *Diagram of the sensors' installation (electromagnetic loops, fiber optic sensors and resistive sensors)*

The experiment site is located in the countryside, 45 km away from LRPC and ESEO buildings. Data collection is executed by Internet connection through a mobile phone used like a modem. Once connected to the Internet, the files of the day are uploaded to the File Transfer Protocol (FTP) server.

6.4. Weather conditions

In terms of clarifying the trajectory tracking issue, it is also mandatory to take into consideration the weather conditions. This information is provided by three Météo France stations, since March 2008. Beaucouzé station (27 km) studies the sunshine, Grez-en-Bouère (34 km) provides the strength and direction of the wind and, finally, Segré (5 km) presents the height of the rain and the air temperature (information measured at 1.5 m above the ground). The axis direction of the road RD961 is north-south.

6.5. Analysis processing

To analyze the position and speed data, a software environment was created to be able to study different decisive criteria at the same time. The following criteria were chosen:

– type of vehicles (car, lorry);

– time of the day (day, night);

– with or without rain;

– small or heavy rain;

– isolated, free or followed-up vehicles;

– with or without crossing (another vehicle).

These criteria are combined altogether in binary order to constitute a decision tree. Definitions attached to these criteria are:

– *isolated vehicle*: only vehicle with a 1,000 m distance ahead and behind;

– *free vehicle:* only vehicle with a 500 m distance ahead and behind;

– *followed-up vehicles*: two consecutive vehicles driving with a distance of less than 125 m between each engine;

– *small rain*: up to 3 mm is considered as a heavy rain for the study;

– distinction between day and night, from the standard time, and 30 min before or after: night;

– if a vehicle is driving on the opposite lane, its trajectory will be mentioned as *with crossing*; if not, then it will be treated as *without crossing*.

6.5.1. *Analysis before installation*

In Figure 6.6, reference 0 represents the lane's center that is used by the drivers, +100 is the edge and –100 is the roadway axis.

The readers can notice from the lateral position layout that:

– during the ascent (the first two graphs on the right bottom part of the figure), most vehicles divert toward the roadway axis;

– during the passage on the summit of the coast (the third graph), most vehicles divert toward the lane's edge;

– at the beginning of the descent (the fourth graph), drivers return toward the axis while staying mainly in the center of the lane;

– at the end of the descent (the last graph), vehicles have taken their position toward the roadway axis back.

An analysis on the drivers' speed was also completed. Speeds of 150 km/h were measured on this secondary road.

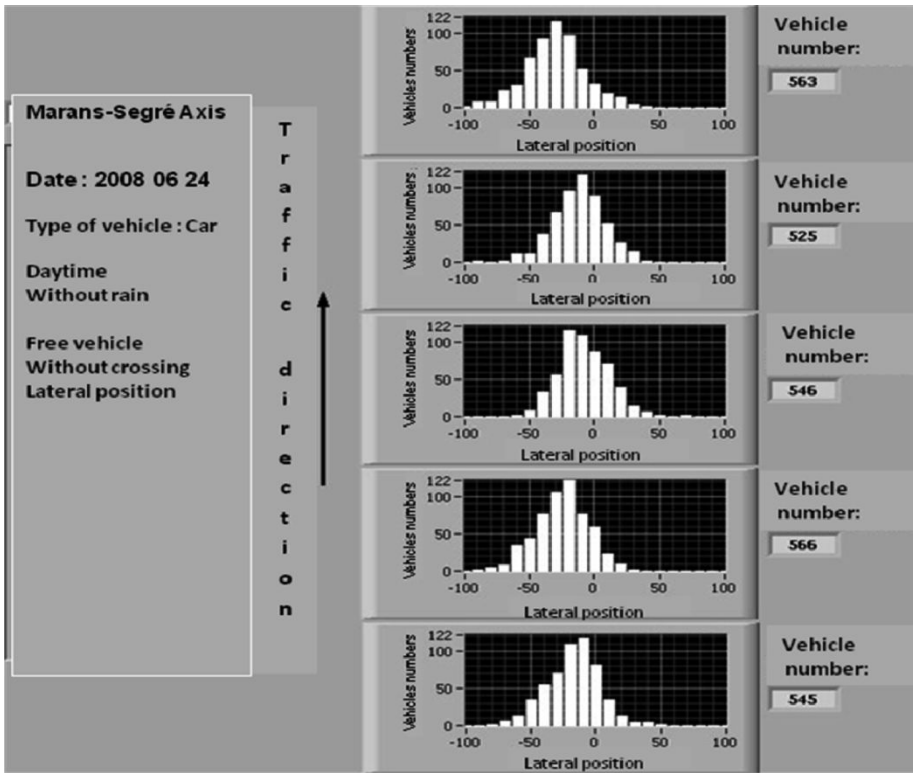

Figure 6.6. *Example of an analysis: on Marans–Segré axis, the arrangement of the lateral positions of the free vehicle during the daytime, without rain and with crossing, on 24 June 2008*

Without getting into specific details on the analysis of the trajectory, Figures 6.7–6.9 enable us to trace back to the drivers' behavior in different situations. During daytime (Figure 6.7), noticeably, whatever the date of the data, the tendencies are the same. In the ascent (points 1–3), "isolated" (square) drivers are more likely to draw closer to the lane axis than the "free" (circle) and "followed-up" (triangle) ones. What can also be noticed is

that when drivers do not experience a crossing situation, they do not hesitate to widely divert on this axis, when arriving at the summit, in order to avoid driving on the undeveloped roadside (point 3).

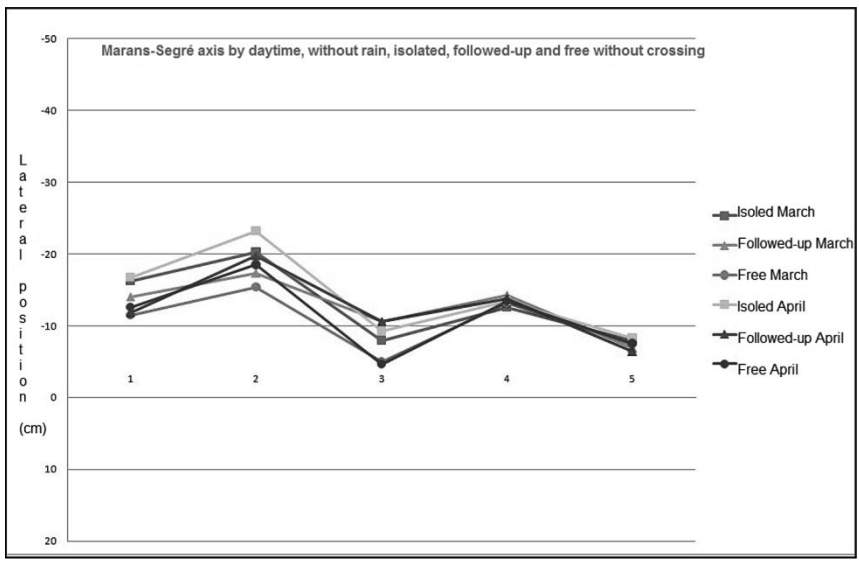

Figure 6.7. *Daytime passage without rain, Isolated, free and followed-up vehicles, and without crossing*

With the same situations at night (Figure 6.8), scatterings as well as more important amplitudes of the lateral position applied by the drivers are observed. An additional 10 cm space toward the roadway axis is present in every situation. For instance, during the ascent, the isolated vehicles run closer to the roadway axis (+32 cm) than they do during the daytime (+20 cm). This is simply due to the fact that at night, drivers make use of the headlights of the vehicles driving on the opposite lane. But as this case study is without crossing, there is no vehicle on the opposite lane.

6.5.2. *Analysis of the development's aftermath*

All the results will not be described but an example of the use of this observational experiment will be presented to enable the analysis of the development's aftermath.

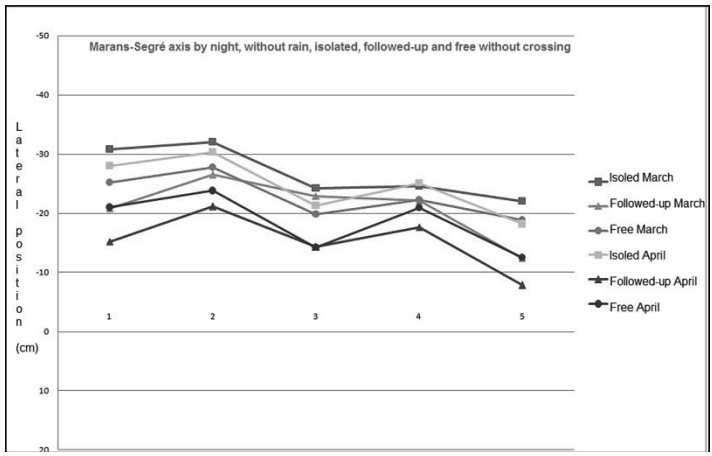

Figure 6.8. *Night passage without rain, isolated, free and followed-up vehicles, and without crossing*

Figure 6.9 illustrates an overview of the two developments: rumble strips on their own on the axis (circle) positioned at 150 m before the summit and the edge verge (triangle) compared to the undeveloped situation (square). The impact of the rumble strips is immediate between points 2 and 3, and drivers' trajectories are recentered on the lane axis (position 0 in the figure). The balanced verge enables the drivers to stay closer to the lane's center.

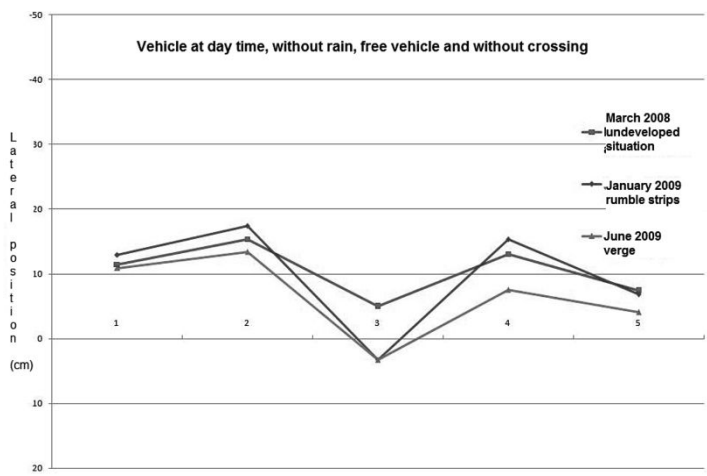

Figure 6.9. *Development's aftermath on vehicle at daytime, without rain, free vehicle and without crossing*

6.6. Conclusion

On a total distance of 1 km, the developed experiment can enter discreet data concerning lateral positioning or speed on the two lanes of both sides of the summit, due to the information of electromagnetic loops. This data is completed with the data obtained by the embedded sensors on the summit, which produce 31 lateral positioning statements, on 120 m, also on both sides of the summit.

All these measures are gathered by communication buses toward the area supervisor, and then transferred at midnight through a connection conveying data packet (GRPS) from the supervisor to the data collection office in ESEO. Finally, they are enhanced with weather data from LRPC.

The processing software allows data analysis considering a defined set of criteria such as the type of vehicles; time of the day (day or night); without rain, small rain and heavy rain; isolated, free and followed-up vehicles; and with or without crossing (another vehicle). A specific analysis of the regular drivers' behavior could also be attempted provided that there is enough data to compare.

This trajectory observatory has been used during the second semester of 2008 to take in initial data before the area's development. Since the second half of 2008, the analysis of the three developments' aftermath is in progress: (1) rumble strips exerted on the central strip, (2) these strips and paved verges and (3) finally the withdrawal of the rumble strips to leave only the paved verges.

6.7. Acknowledgments

Special thanks are due to every participant of the project: members of VIZIR group – and particularly the Maine-et-Loire (49) departmental council office, the technical departmental agency of Le Lion d'Angers, and the LRPC of Angers for their help in the establishment of the observatory – as well as the people who worked on topic 6 of the SARI program.

6.8. Bibliography

[AUB 06] AUBIN S., PLAINCHAULT P., IENG S.-S., *et al.*, "Sensor technologies to follow vehicles for ITS", *6th International Conference on ITS Telecommunications (ITST '06)*, China, pp. 870–873, June 2006.

[AUB 09] AUBIN S., Réseaux de capteurs coopératifs dédiés aux suivis de trajectoire de véhicules, PhD Thesis, National Polytechnic Institute of Toulouse, 2009.

[DAU 08] DAUCHER D., JACOB B., "Investigation of road vehicule trajectory for road safety", *Transport Research Arena Conference* (*TRA '08)*, Slovenia, 2008.

[FER 06] FERDINAND P., "Capteurs à fibers optiques à réseaux de Bragg", *Techniques de l'ingénieur – Mesures mécaniques et dimensionnelles*, R 6 735, 2006.

[KLE 01] KLEIN L.A., *Sensor Technologies and Data Requirements for ITS*, Artech House, 2001.

[LEC 02] LECHNER D., Analyse du comportement dynamique des véhicules routiers légers: Développement d'une méthodologie appliquée à la sécurité primaire, Thesis, INRETS, 2002.

[MOU 06] MOURLION B., GRUYER D., LAMBERT A., *et al.*, "Variance behavior and signification in probabilistic framework applied to vehicle localization", *IEEE Intelligent Vehicle Symposium 2006*, Tokyo, Japan, 13–15 June 2006.

[PLA 05] PLAINCHAULT P., Sécurisation de la conduite par communication véhicule infrastructure à base de transpondeurs, PhD Thesis, National Polytechnic Institute of Toulouse, 2005.

[PLA 09] PLAINCHAULT P., AUBIN S., Dispositif de détection de la position d'un objet dans une zone, Patent FR 2 922 352, 17 April 2009.

7

Large Deformable Antennas

7.1. Introduction

Radio detection and ranging (radar) is a system designed for tracking and identifying weakly cooperative moving targets (such as aircraft and ships). Recent developments in radar front-end technology show a clear trend toward miniaturization of electronic components for transmitting and receiving chains. Current developments include single chip solutions for digital receivers to be attached to individual elements, and on the tansmission side, integration of phase shifter and power amplifier into one Radio Frequency (RF) chip component. These breakthroughs in radar technologies enable us to consider disruptive antenna supports with improved flexibility drastically gaining in weight and volume. However, efficient target localization depends on the antenna directivity. High directivity is directly linked to the antenna size compared to the RF carrier wavelength. The radiation pattern describes the angular dependence of the energy radiated by the antenna in the far-field. Currently, the quality of this radiation pattern emitted by electronically steered antennas is ensured due to an extremely high mechanical rigidity of the planar structure supporting the hundreds of individual emitting dipoles. To obtain optimal performances, the dipoles must be distributed on a perfectly flat reference surface. Therefore, the structure supporting the radiating elements needs to be extremely rigid and almost perfectly assembled. These mechanical constraints imply large weight and volume as well as a high manufacturing cost. Moreover, the deployment of radar systems and their fabrication cost are directly

Chapter written by Sylvain GIRARD, Hervé GILLES, Philippe LEPRINCE, Olivier CLOUARD, Mourad CHTIOUI, Isabelle BARBEREAU, Guillaume LESUEUR and Thomas MERLET.

proportional to the mechanical structure complexity. Therefore, a significant reduction in its rigidity will lead to potential gain in tactical deployment and cost savings. However, this reduction would also induce significant degradations of their performances due to mechanical distortions resulting from external perturbations such as wind, ice and thermal dilatation [SCH 07]. As the use of complete electronically steered arrays allows acting directly on the emitted RF waves, the challenge consists of dealing with the ability to dynamically restore system performances.

Investigations of deformable structures dynamically compensated on the RF domain rely on manufacturing cost diminution as well as maintenance and integration cost reduction, since accurate planarity fabrication and controls will be tremendously reduced.

For radar applications, the tolerances on mechanical distortions depend on the RF carrier. For S-band radar (f_{RF} = 3 GHz, λ = 10 cm) with a 2 m^2 surface antenna, the following constraints are identified:

– the error on the angular location of the target caused by mechanical distortions can reach several degrees while the operational requirement for the radar angular accuracy is the order of milliradian; deformation also induces a rise in side lobes;

– the error on the target velocity depends on the stability of the antenna during the RF burst (with a typical time duration of tens of milliseconds). The dynamic variations of the antenna shape add substantial bias in the measured Doppler frequency.

One way of compensating for these detrimental effects consists of acting directly on the amplitude and phase of the electronic signals sent on each individual radiating element to reshape the global radiation pattern. In this approach, the antenna is instrumented with transducers suitable for measuring in real time the absolute distortions compared to a reference plane. The information provided by the sensors combined with mechanical models should allow recalculating the global mechanical shape of the structure. To be efficient, the electronic compensation must limit the pointing error within few milliradians with a time response in the ms range. Moreover, such compensation should also avoid parasitic target detections by limiting the impact of side lobes.

Emitting radar antennas are highly electromagnetically perturbed environments with peak power reaching up to the megawatt (MW) during the emission process. Therefore, classical approaches based on electrical constraint gauges – or any other electronic components directly implemented on the front of the emitting structure – should be avoided. Considering the strong electromagnetic peak power emitted by active antennas, it is necessary to select sensors totally insensitive to external electromagnetic perturbations. Optical solutions based on purely passive components appear to be very attractive for such applications. A set of passive optical sensors distributed on the antenna structure would be a promising approach for real-time compensation of the mechanical distortions of an active radar antenna.

This application will be illustrated for S-band radar antenna arrays. The originality of the present method is based on the following technical specificities:

– it is an instrumented technique with a discrete series of distributed sensors; all the measurements necessary for the antenna surface reconstruction are done simultaneously in real time with a time response shorter than the fastest strain deformations;

– compensation algorithms take into account the full radiation pattern of the antenna, including the side lobes; the method developed here restores the gain of the antenna in all directions simultaneously, at the emission as well as at the reception [LES 09a].

In this chapter, optical instrumentation for mechanical distortion compensation on a large deformable active antenna is presented. First, a mechanical analysis shows that a limited number of transversal displacement measurements (typically between 5 and 10 points depending on the complexity of the mechanical structure) are sufficient to restore the global shape of the antenna. Two principles for the optical sensors are presented. Both are based on the generation of a laser light plane acting as an absolute reference plane. The first approach uses a passive optical probe made up of fiber ribbons that intercept a laser light plane used as a reference plane. Each optical probe contains only passive optical components, whereas all the optoelectronic and electronic parts of the sensor are delocalized under the emitting front side of the antenna via optical fiber links. Such disposal

ensures a total immunity to electromagnetic perturbations. The second sensor is based on a polarization gradient encoded on a coherent light beam to produce an absolute reference scale.

7.2. Mechanical analysis

The mechanical structures supporting radar antennas have been until now extremely heavy and bulky in order to maintain the radiating surface flatness with an accuracy typically a few percent of the RF wavelength (λ = 10 cm for S-band radar). Based on preliminary mechanical investigations, distortions may be decomposed into a limited number of basic shapes, such as, for instance, distortions due to dynamic loads (wind, pitch and roll, and engine), additional loads (ice and snow) and natural vibrating modes of the antenna. As a result, all the mechanical distortions that can occur on antenna structures are computable and measurable with a limited number of distributed sensors.

The number and precise locations of the sensors are based on mechanical simulations of the radar antenna submitted to the most likely external constraints. Basically, one optical probe is necessary for each vibration mode or stationary distortion. Its location is selected to obtain the best discrimination with the other modes. For our preliminary experimental setup, we have started using a stainless steel plate with a rectangular shape of 1.54 m $\times$ 0.79 m with mechanical properties similar to large deformable antenna (LDA) structures. This experiment will be described in detail in section 7.4. The mechanical models show, as expected, that this structure presents only a limited number of basic distortions or vibration modes with a maximum vibration frequency up to 100 Hz. The distortion range does not exceed ±20 mm and, in order to recover the full shape of the antenna with a reasonable precision, each optical probe should measure the displacement with a resolution down to λ_{Radar}/1,000, which corresponds to 100 μm for a 3 GHz RF carrier.

7.3. Optical instrumentation for deformable antennas

The highly disturbed electromagnetic environment around radar antenna is a major drawback in the development of strain sensors. The radar antennas emit, with an average output, powers ranging from 1 W up to 100 kW. This

corresponds to peak power reaching up to several MW during the emission burst. These extremely high peak powers require a complete galvanic isolation of the measuring instrumentation located on the surface of the antenna.

Recently, various optical solutions have been investigated to determine the full-field deformation of simple planar structure. In most cases, it consists of localized measurements of the structure deformation using a set of distributed passive optical sensors. One approach consists of implementing a series of fiber Bragg grating sensors [WAN 07]. The main drawbacks are a strong sensitivity to temperature fluctuations [KAN 98] and a longitudinal strain measurement instead of a transverse displacement measurement [IOD 05]. Another approach, recently developed in our research group [LES 08, LES 09b], uses a reference optical plane generated slightly above the mechanical structure and a set of optical sensors suitable for measuring the transverse deformations of the structure compared to the reference plane.

We have identified different characteristics for the sensors:

– displacement range: 50 mm/resolution < 100 μm/detection bandwidth: from Direct Current (DC) up to 250 Hz;

– electromagnetic compatibility (EMC);

– easy integration within a rotating antenna structure; adaptability to different antenna configurations;

– performing measurements in real time for an effective amplitude and phase compensation;

– lifetime compatible with a radar system (~20 years).

The basic principle of the optical sensor is illustrated in Figures 7.1 and 7.2. It is based on the generation of a coherent light plane acting as an absolute reference. After reflection on a conical mirror, a collimated laser beam is spread out over 360°, forming a homogeneously distributed optical plane. By precisely adjusting the angular orientation of the conical mirror, it becomes easy to adjust the orientation of the reference optical plane parallel to the pattern of radiating elements. A limited number of identical passive optical probes (typically between 5 and 10 depending on the complexity of the mechanical structure, four probes are represented in Figure 7.1) are

judiciously distributed along the surface for measuring local transversal displacements compared to the reference plane.

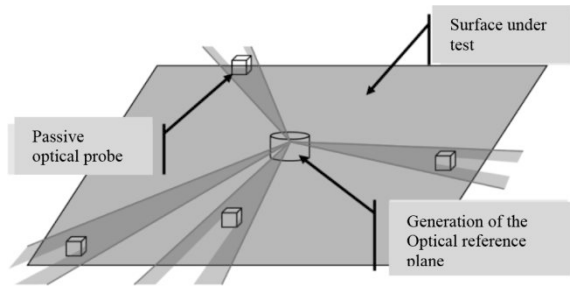

Figure 7.1. *Principle of the optical sensor*

The light distribution collected is optically transmitted to photodetectors through optical fibers. Photodetectors are located below the radiating surface of the antenna. In this way, electronic and signal processing is completely isolated from electromagnetic RF waves emitted by the antenna. The optical probes being fully fiberized and light generating the reference plane being also supplied via an optical fiber link, this principle provides a measuring probe that contains only passive elements near the radiant surface.

Figure 7.2. *Conical mirror used to generate the optical reference plane. For a color version of this figure, see www.iste.co.uk/thomas/sensors.zip*

Several solutions have been investigated in order to detect the position of the probe relative to the reference light plane. The encoding position may first be directly contained in the thickness of the optical reference plane itself. In this case, the position coding is performed at the laser light emission and the optical passive probe located on the antenna surface is only

used to collect this information. A second solution consists of obtaining the position information due to the probe itself, whereas the light plane is only used as the absolute reference. Table 7.1 summarizes the different possibilities for encoding position into the reference light plane or using the optical probe.

Technique	Encoding	Characteristic variable	Reference plane thickness
Emission encoding	Spectral distribution on the thickness of the light plane	λ Wavelength	Thick
Emission encoding	Rotation of the polarization state on the thickness of the light plane	α Polarization orientation	Thick
Emission encoding	Spatial gradient of the light intensity in the light plane	I Intensity	Thick
Detection encoding	Spatial transmission gradient of the probe	I Intensity	Thin
Detection encoding	Image from the light distribution collected on the probe	I Intensity	Thin

Table 7.1. *Summary of the various possibilities of position encoding*

The emission encoding with a spatial gradient of the light intensity in the reference plane was rejected because of its low environmental robustness. A parasitic attenuation of the beam caused by the external perturbation (dust, smoke, etc.) would be interpreted as a displacement of the antenna.

Encoding with spectral distribution on the thickness of the light plane requires the use of a detection system that is able to analyze the spectral distribution of the sampled light. This method is complex to implement for real-time measurements on a large number of individual sensors. This type of devices is, therefore, not suitable for dynamic measurements at a frequency of up to 100 Hz at a reasonable cost.

We have developed two types of sensors based on the general principle described above:

– the first type of sensor is based on the generation of a homogeneously distributed optical plane 5 mm thick slightly above the structure. The passive optical probes are made up of optical fiber ribbons that intercept the optical reference plane and image the light distribution below the antenna. Each optical probe contains only passive optical components, whereas all the optoelectronic and electronic components are delocalized below the emitting front side of the antenna via optical fiber links, ensuring a total immunity from electromagnetic perturbation;

– starting from an expended laser beam, the second type of sensors consists of encoding the position information using a polarization gradient recorded within the thickness of the reference plane.

7.3.1. *Principle of the optical sensor based on fiber ribbons*

This solution consists of collecting the light distribution of the reference optical plane at each measurement point. This technique is directly similar to fiber-optic endoscopy that is widely used for medical imaging inside human body without galvanic connection.

In our optical setup, a single-mode fiber-pigtailed laser diode (LD) (a pump module for Erbium Doped Fiber Amplifier (EDFA) with Plaser = 300 mW at 980 nm) was selected as a laser source with extended lifetime and high reliability. The beam quality is excellent due to the single transverse mode optical fiber acting as an efficient spatial filter. After reflection on a conical mirror, the collimated laser beam is spread out over 360°. An array of optical fibers aligned perpendicularly to the reference laser plane is used to collect the intensity distribution at the location of each probe. Each optical probe (see Figures 7.3 and 7.4) is made of a ribbon of 60 stacked step-index multimode optical fibers (core diameter 105 μm, numerical aperture 0.22). At the extremity located on the antenna surface, the optical fibers are regularly spaced using V-grooves with Λ_1 = 0.93 mm pitch, covering a total vertical height of L = 55 mm. The ribbon extremity corresponds to a passive one-dimensional (1D) imaging detector, each fiber corresponding to an individual pixel that samples the local intensity distribution. The fiber ribbon re-imaged this distribution directly on a position sensitive detector (PSD) located below the antenna (Figures 7.3

and 7.4). These analog photodetectors are used to accurately measure the barycentric position of the incident light distribution. The photocurrent generated by the light distribution on the PSD is divided into two photocurrents i_1 and i_2. The barycentric position x_G could be deduced from the two photocurrents as follows:

$$x_G = \frac{L_{psd}}{2}\frac{i_2 - i_1}{i_2 + i_1} \qquad [7.1]$$

A silicon (L_{psd} = 24 mm length) PSD was selected for its good sensitivity at 980 nm and its excellent signal-to-noise ratio. On the PSD side, the optical fibers are joined. The pitch of the fiber ribbon at the detection extremity was reduced to Λ_2 = 250 µm so that the total width is equal to L' = 15.34 mm. Taking into account the scaling factor between the two ends of the fiber ribbons, the position of the probe relative to the optical reference plane is given by:

$$X_{def} = \frac{L}{L'} \cdot x_G \qquad [7.2]$$

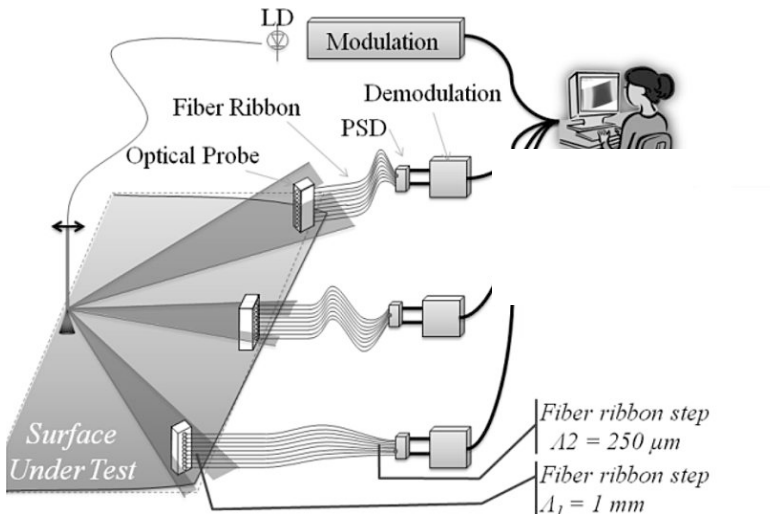

Figure 7.3. *Principle of the optical sensor based on passive probes made up of fiber ribbons*

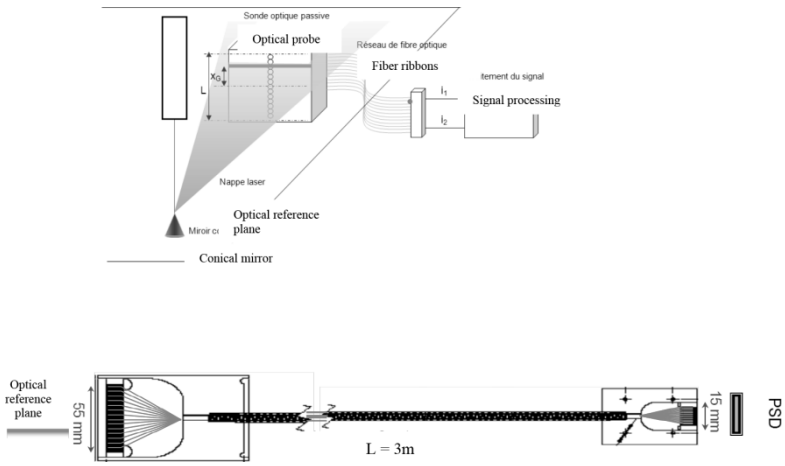

Figure 7.4. *Optical probes with fiber ribbons*

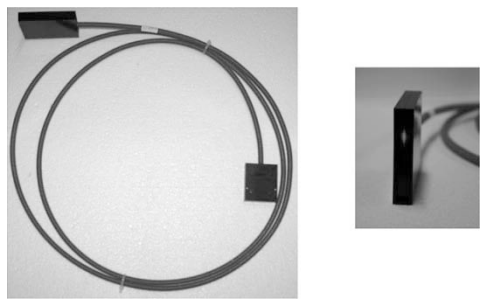

Figure 7.5. *Photograph of the fiber probes: side of the probe located on the radiating plane, total width L = 55 mm*

One of the main problems to solve concerning the optical sensor is the extremely low photon flux collected by each optical probe. For example, assuming that the optical probes are located on the edge of the stainless steel plate in our experimental setup, the expended laser beam covers a perimeter equal to $\varphi_1 = 5m$. The diameter of the fiber core being limited to $\varphi_2 = 105\mu m$ and the transmission of the optical probe measured as T_{probe} = 10%, it is easy to estimate the optical power P_{meas} collected by each probe:

$$P_{meas} = P_{laser}.T_{prob}.\varphi_2 / \varphi_1 = P_{laser}.T_{tot} \qquad [7.3]$$

Typically, we obtain $T_{tot} = 2.10^{-6}$ which corresponds to an available optical power on the PSD of only P_{meas} = 0.6 μW. In order to improve the signal-to-noise ratio and to suppress the parasitic ambient light, the output power of the LD was modulated at 10 kHz via the injected current. After analog-to-digital conversion, the signals detected on the PSD were demodulated numerically. When each optical probe is calibrated, only minor imperfections attributed to slight misalignments or imperfections of the optical fibers transmission at the extremity of the ribbon leads to position errors typically lower than 100 μm.

As already mentioned, it is necessary to precisely adjust the thickness of the reference light plane in order to improve the response of the optical probes. This optimization can be obtained by selecting the focal lens used for collimating the laser beam before the angular expansion on the conical mirror. As illustrated in Figure 7.6, a reference light plane with a thickness lower than the period Λ_1 leads to sampling artifacts clearly distinguishable on the measured position. In this figure, the reference plane thickness varies between e = Λ_1 and e = 10Λ_1. A numerical model shows that at least 2–3 optical fibers must be simultaneously illuminated to determine the transverse displacement correctly. In practice, we have adjusted the thickness to cover 4–5 fibers. The averaging effect on the PSD allows an excellent restitution of the detected position, with a typical resolution of the barycenter position better than 100 μm on a dynamical range of 50 mm. The detection bandwidth covers from Continuous Wave (CW) to 1 kHz, allowing us to record in real time the fastest vibration modes of the mechanical structure as well as static distortions.

7.3.2. *Principle of optical sensor based on polarization rotation*

In this section, we describe another approach based on polarization gradient encoding applied to a large coherent light beam. Figure 7.7 illustrates the global principle of our device. Starting from an enlarged laser beam, the method consists of coding a polarization gradient on the beam. This gradient acts as an absolute reference scale and is locally analyzed using distributed passive optical probes made up of polarizer and optical fibers. In Figure 7.7, the linear polarization state is parallel to the z-axis at the bottom of the beam, whereas the polarization state linearly rotates along the y-axis and becomes parallel to the y-axis at the top of the beam.

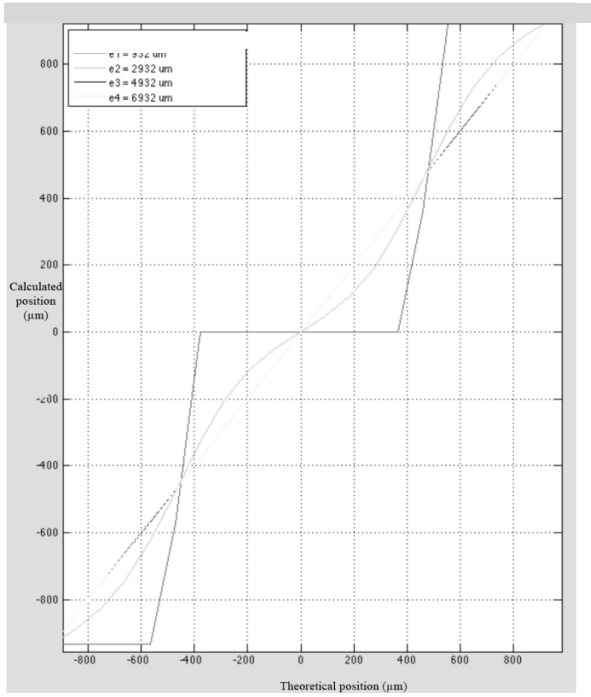

Figure 7.6. *Influence of the light plane thickness. For a color version of this figure, see www.iste.co.uk/thomas/sensors.zip*

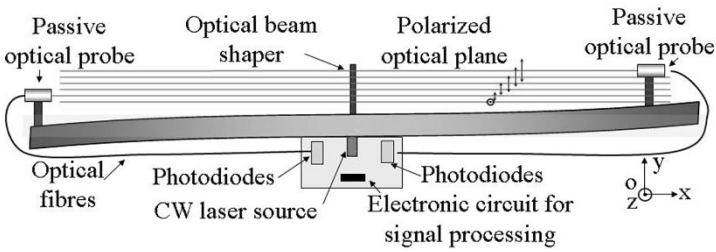

Figure 7.7. *Principle of the optical sensor based on polarization technique*

To check the concept, preliminary investigations are made using 1D geometry as a basic mechanical structure. In our optical setup (see Figure 7.8), a collimated beam emitted by a linearly polarized 3 mW LD (λ = 670 nm) is first enlarged using a beam-expander made up of two cylindrical lenses. A progressive rotation of the linear polarization state is

then obtained using the circular anisotropy (also called optical activity) of a crystalline quartz prism. This prism is cut with the optical axis perpendicular to the entrance facet (two-end arrow in Figure 7.8) to avoid parasitic polarization modification due to birefringence. The optical activity alone introduces only polarization rotation along the y-axis while keeping the polarization state linear. The rotation angle α depends on the prism dimensions (L and h), the refractive index difference between left and right-handed polarization states $\Delta n = n_{right}-n_{left}$ due to optical activity of quartz and the transverse position along the y-axis:

$$\alpha(y) = \frac{\pi}{\lambda} \cdot \Delta n \cdot \frac{L}{h} \cdot \left(\frac{h}{2} - y \right) \qquad [7.4]$$

A second prism made of BK7 glass is glued top-to-bottom with the quartz-prism to avoid any unwanted deviation due to parasitic refraction effects.

In equation [7.4], *y* represents the transverse coordinate compared to a reference plane represented as dashed line in Figure 7.8. To analyze the local polarization state, i.e. measuring the rotation angle α, a passive optical probe is fixed on the studied structure. It is composed of one Glan–Thompson (GT) prism and two optical fibers. Incident polarization states are split by birefringence in two orthogonally polarized components along the *y*- and *z*-axes. The detection is deported via two plastic optical fibers (core diameter 1 mm) located well below the bar.

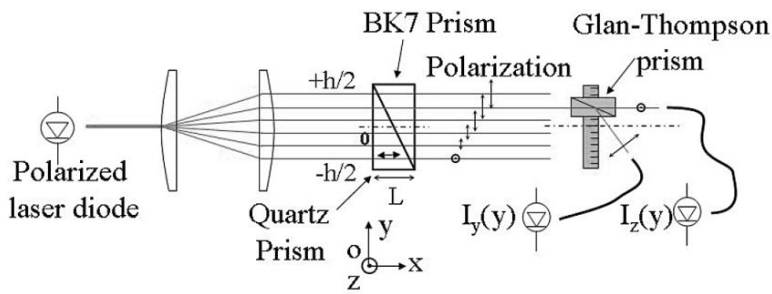

Figure 7.8. *Experimental setup for 1D deformation measurement*

A simple ratio, which involves the two photocurrents I_y and I_z corresponding, respectively, to y and z-components, allows recovering the transversal displacement as:

$$\frac{\Delta I}{I_0} = \frac{I_y - I_z}{I_y + I_z} = \cos\left[2\alpha(y)\right] \qquad [7.5]$$

Figure 7.9 shows that a good agreement is obtained between experimental results and equation [7.5]. These results are obtained by manually translating the optical probe into a 20 mm thick optical beam. For small transversal displacements localized around $\Delta I / I_0 = 0$, we can linearly approximate expression [7.5] with

$$\frac{\Delta I}{I_0} = \frac{2\pi}{\lambda}\Delta n \cdot \frac{L}{h} \cdot (y - y_0) \qquad [7.6]$$

Under these experimental conditions, the optical polarization sensor allows a position measurement with typically 50 µm resolution on the full dynamical range, which is limited to 5 mm mainly due to the prism geometry. The detection bandwidth extends from stationary regime up to a few kHz.

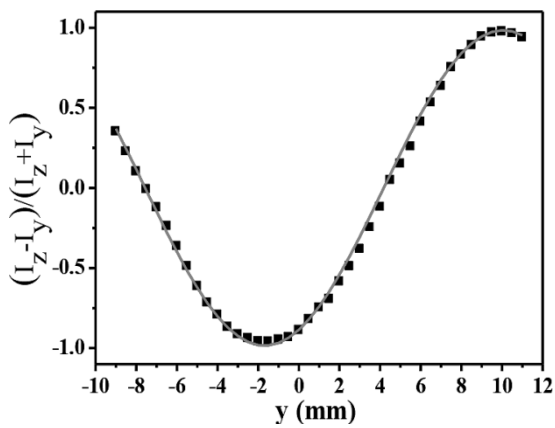

Figure 7.9. *Evolution of ($\Delta I/I_0$) versus the position y of the optical probe for L = 12 mm, h = 20 mm and Δn = 4.8.10-5*

The principle can be easily adapted to a surface distortion analysis like LDA. In this case, the main problem will be to create an optical plane with a polarization gradient. One solution is to use a conical mirror to angularly expand the large laser beam at 360°, creating a homogeneously distributed thick optical plane. The polarization gradient can be coded before or after reflection on the conical mirror using various approaches: optical activity, liquid crystal display or microstructured optical polarizer. Finally, another way to improve the polarization sensor will be to get a more accurate polarization state determination. For that purpose, each passive optical probe would contain four polarizers connected to four individual optical fibers in order to calculate the complete Stokes parameters of the collected light.

In this chapter, the optical sensor with fiber ribbons was privileged. It is more mature and is a good compromise between cost implementation complexity, ease of implementation, size of the sensor board and signal processing on signal detection side. It has been applied to the measurement of deformations of the antenna mockup presented in the following section.

7.4. Experience on a planar structure

In order to validate the global concept of the measurement system with a limited number of optical probes, a stainless steel plate (1.54 m × 0.79 m) was used. This structure allows reproducing deformations similar to that of actual deformable antennas. The material chosen for the deformable surface material is a thick sheet e = 2 mm with a high Young's modulus (E_{steel} = 220 GPa). The plate was mechanically fixed on the center and only one side measuring 0.4 m × 0.79 m was left free to vibrate or to be distorted statically using mechanical actuators. A force of 50 N manually applied to one end of the deformable plate induces a transversal deformation equal to 21 mm. This strain amplitude corresponds to a transverse displacement of $\lambda/4$ for S-band antenna (of wavelength λ = 100 mm). Figure 7.10 shows several views of the deformable structure (plate + support) designed and conducted in the Centre de recherche sur les Ions, les MAtériaux et la Photonique (CIMAP) Laboratory.

Three optical probes similar to the one described in section 7.3 have been distributed on the instrumented stainless steel plate. A laser, collimation system and the conical mirror are fixed on the central frame and can measure the deformations of the structure. A photograph of the model is shown in

Figure 7.11 with seven probes attached magnetically to the deformable metal surface studied. For the experiment, only three probes are used and they were located on the edge of the structure, on the position denoted A, B and C in Figure 7.10.

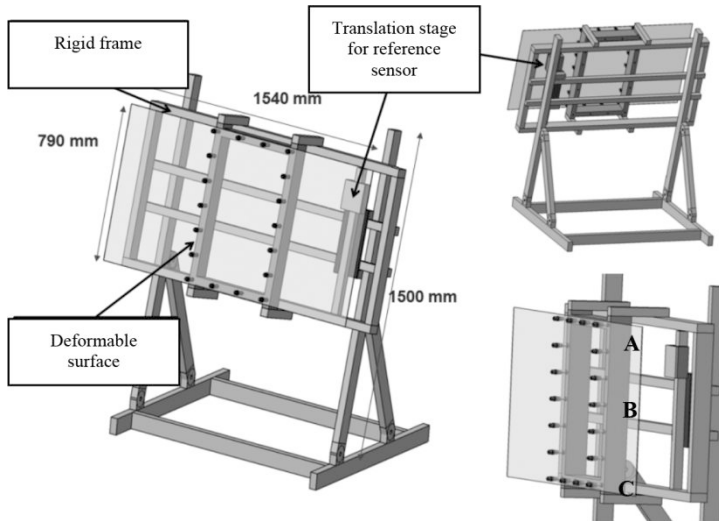

Figure 7.10. *Drawing of the deformable structure*

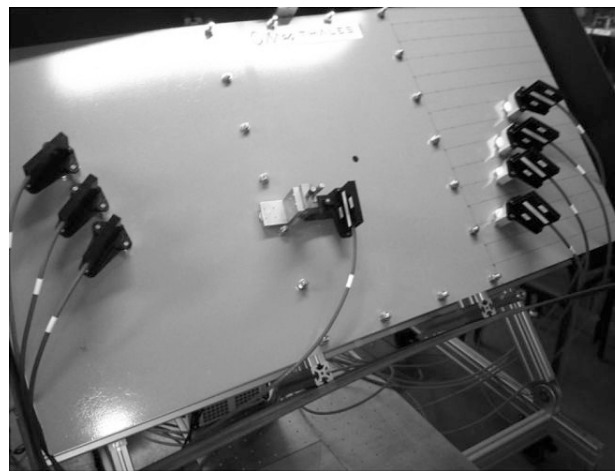

Figure 7.11. *Photograph of the deformable structure with passive optical probes*

To calibrate the system, it is first necessary to precisely measure the topography of the structure without any external perturbation. This initial measurement could be done step-by-step using a commercial optical sensor based on the triangulation technique (Keyence LK-G152). The two-dimensional (2D) topography obtained is noted $S_0(x,y)$ and corresponds to the static deformation compared to a perfect plane due to the deformation of the structure without any external loads.

Then, the second step in the calibration process of the system corresponds to an individual determination of the different distortion/vibration modes of the structure. The corresponding topography for the *i*th eigen-modes is called $S_i(x,y)$ and it could be obtained via a direct measurement after controlled excitation or via finite element calculation models. In the algorithm, we used the difference between dynamics and statics deformation.

$$D_i(x,y) = S_i(x,y) - S_0(x,y) \qquad [7.7]$$

For the half-plate used during the preliminary experiments, only three main vibration modes were identified and three corresponding distortions, D_i, were mapped. It is straigthforward during the initial calibration to also obtain a matrix M representing the response of the three optical probes located, respectively, at (Xp_1,Yp_1), (Xp_2,Yp_2) and (Xp_3,Yp_3) to the three distinguishable vibration modes:

$$M = \left(\Delta Z_i(Xc_i, Yc_i)\right)_{i=1..3} \qquad [7.8]$$

where $Z_i(Xp_j, Yp_j)$ corresponds to the displacement measured on the probe *j* due to the distortion mode *i* alone. The best position of the optical probes corresponds to a matrix M close to unity.

During a real-time reconstruction, the displacements Zp_1, Zp_2 and Zp_3 recorded simultaneously by the three optical probes could be directly represented by a column vector Z,

$$Z = \left(Zp_i\right)_{i=1..3} \qquad [7.9]$$

As each displacement should be a linear combination of the distortion modes, a vector A corresponding to this linear combination could be introduced as follows:

$$Z = M.A \quad \Rightarrow \quad A = M^{-1}.Z = \left(a_i\right)_{i=1..3} \qquad [7.10]$$

As M only depends on the location of the optical probes, it could be considered as an intrinsic and constant characteristic of the measurement system.

Knowing the decomposition vector A, it is easy to reconstruct the shape of the global structure using [7.7]

$$S_{meas}(x,y) = S_0(x,y) + \sum_{i=1}^{3} a_i.D_i(x,y) \qquad [7.11]$$

As the calculations are based on matrix algebra, it is easy to reconstruct the whole form of the structure in real time, without using high-power calculator as illustrated in Figure 7.12.

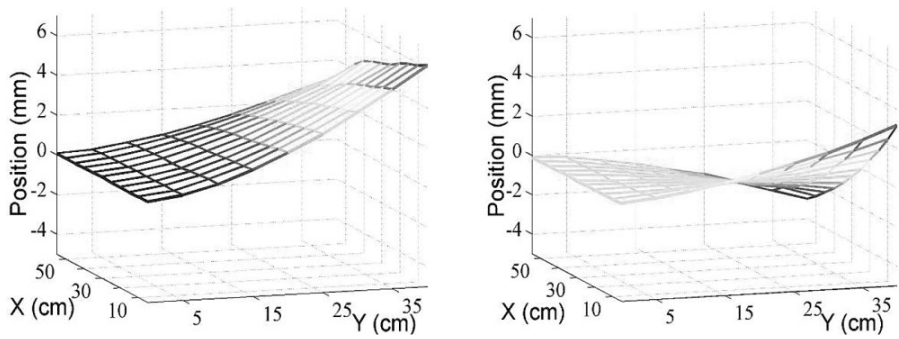

Figure 7.12. *Examples of the real-time reconstructed forms for the half stainless steel plate. For a color version of this figure, see www.iste.co.uk/thomas/sensors.zip*

To check the validity of the technique and to verify the precision obtained, we have compared the measured topograghy reconstructed $S_{meas}(x,y)$ with a measured topography step-by-step using a commercial

optical triangulation sensor as already described in the sequence of calibration (Figure 7.13).

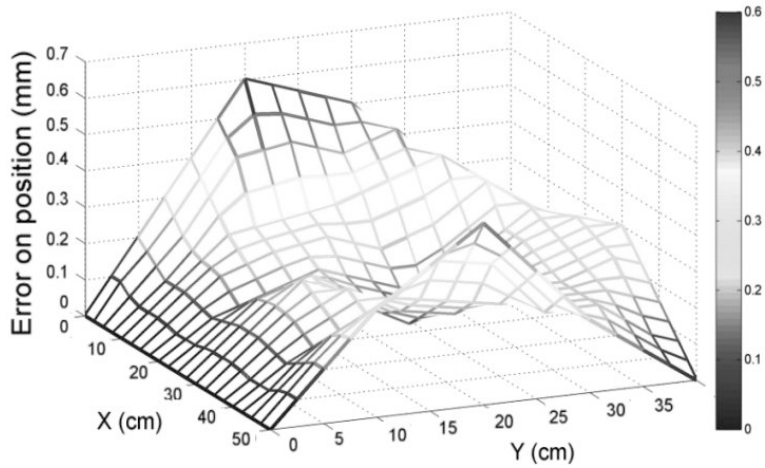

Figure 7.13. *Local error map obtained using a comparison between the reconstructed surface and a step-by-step measurement using a commercial laser sensor. For a color version of this figure, see www.iste.co.uk/thomas/sensors.zip*

The local error map shows that less than 0.6 mm is obtained on the whole recovered surface for displacement up to 20 mm.

An array of radiating elements has finally been simulated on the surface subjected to deformation. As the positions of the radiating elements of our model are known, it is possible to calculate the compensation law for antenna emission. Figures 7.14 and 7.15 show the front face of the LabVIEW program allowing the acquisition, signal processing and real-time display of the reconstituted distorted shape. This program allows the comparison between uncompensated and compensated radiation diagrams. To simply illustrate the results obtained, we simulated a linear array consisting of 40 elements placed at the edge of the plate subjected to deformation. These elements are located on the axis connecting the three sensors (A-B-C). Figure 7.14 corresponds to a pair deformation on the half deformation area and Figure 7.15 corresponds to an odd deformation.

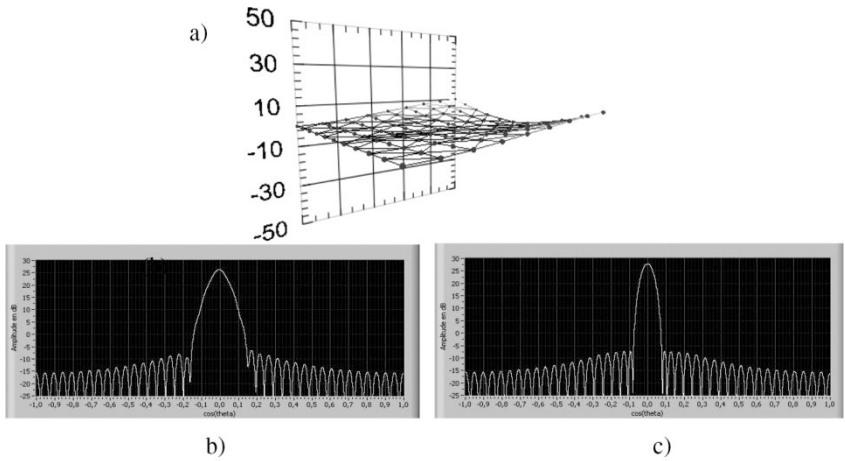

Figure 7.14. *Front face of the LabVIEW program for a pair deformation: a) 3D visualization of the antenna shape, b) uncompensated radiation diagram and c) compensated radiation diagram*

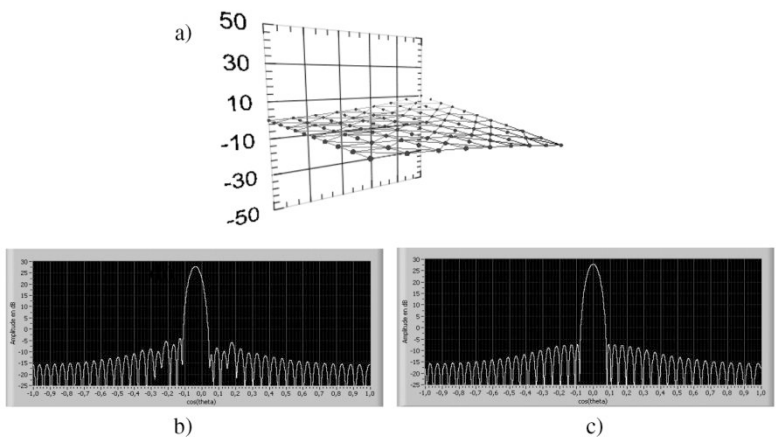

Figure 7.15. *Front face of the LabVIEW program for an odd deformation: a) 3D visualization of the antenna shape, b) uncompensated radiation diagram and c) compensated radiation diagram*

Pair deformations have the effect of broadening the main beam of the antenna emission; odd deformations do not alter the width of the beam, but highly alter the main emission direction. Figures 7.14(c) and 7.15(c) clearly

show that knowledge of the shape of the antenna given by the sensors is used to reform a satisfactory radiation pattern very close to that of an ideal antenna.

7.5. Conclusion

We have shown in this chapter a way to measure the deformation of a flat structure. In our approach, the antenna is instrumented with optical transducers suitable for measuring in real time the absolute displacement compared to a reference plane on a limited number of points. Two solutions for optical probes have been studied and developped in our laboratory. The first solution is based on a measurement of light polarization and the second solution is based on the use of an imaging fiber device. In both cases, electromagnetic immunity is provided by the use of optical fiber to take the laser light on the antenna and bring back the light distribution underneath the surface. The first optical sensor is based on a polarized twisted beam discrimination. Starting from an enlarged laser beam, the method consists of coding a polarization gradient on the beam. This gradient acts as an absolute reference scale and is locally analyzed using distributed passive optical probes made up of polarizer and optical fibers. The second passive optical sensor is based on a set of optical fiber probes allowing local transverse displacements to be accurately measured. The probes are robust and have a reasonable manufacturing cost. The passive optical sensor developed allows the reconstruction of an electronically steered antenna structure without any perturbations due to the electromagnetic environment. Its extreme simplicity while keeping good resolution and dynamics is an encouraging preliminary step for the development of the concept of dynamically compensated deformable antennas. It has an adjustable geometry depending on the dynamics and resolution required. It is adaptable to electronic scanning antennas of different sizes and operating in different frequency bands. In order to check the validity of the technique and evaluate its precision on a real environment, we have compared the reconstructed distortions to the real one on a stainless steel plate (0.4 m $\times$ 0.79 m). With only three probes, the resolution on the whole surface is better than 1% of the RF wavelength for displacement up to half the RF wavelength. Data from optical sensors have been finally processed to effectively compensate the radiation pattern.

The sensor is now instrumenting an S-band antenna mockup (Figure 7.16) and the first tests will be performed soon.

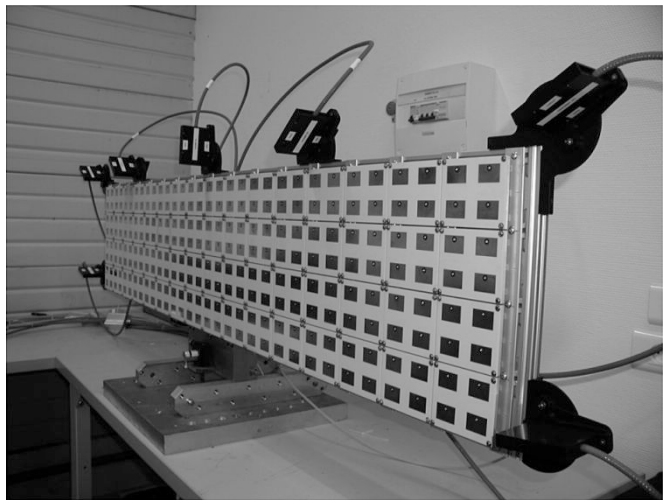

Figure 7.16. *Photograph of the S-band antenna mockup with passive optical probes*

7.6. Acknowledgments

A part of this work was supported by Délégation Générale de l'Armement – France (DGA) in the framework of PEA – GRANDE project.

7.7. Bibliography

[IOD 05] IODICE M., STRIANO V.,CAPPUCCINO G., *et al.*, "Fiber Bragg grating sensors-based system for strain measurements", *Proceedings of Fibers and Optical Passive Components*, pp. 307–312, 22–24 June 2005.

[KAN 98] KANG S.C., KIM S.Y., LEE S.B., *et al.*, "Temperature-independent demodulation technique for fiber Bragg grating strain sensors using a tilted fiber Bragg grating", *Proceedings of Lasers and Electro-Optics (CLEO 98)*, pp. 329–330.

[LES 08] LESUEUR G., GILLES H., GIRARD S., *et al.*, "Optical sensor for real time reconstruction of distortions on electronically steered antenna", *IEEE Photonics Technology Letters*, vol. 20, no. 21, pp. 1763–1765, 1 November, 2008.

[LES 09a] LESUEUR G., CAER D., MERLET T.H., *et al.*, "Active compensation techniques for deformable phased array antenna", *Conference on Antenna and Propagation (EuCAP)*, Berlin, Germany, March 2009.

[LES 09b] LESUEUR G., MARCINIAK A., GILLES H., *et al.*, "Polarization optical sensor for dynamical deformation measurements on 1 or 2D mechanical structures", *IEEE Photonics Technology Letters*, vol. 21, no. 18, pp. 1311–1313, 15 September 2009.

[SCH 07] SCHIPPERS H., *et al.*, "Vibrating antennas and compensation techniques research in NATO/RTO/SET 087/RTG 50", *IEEE Aerospace Conference*, Big Sky, MT, March 2007.

[WAN 07] WANG Y., CHEN N., YUN B., *et al.*, "Use of fiber Bragg grating sensors for determination of a simply supported rectangular plane plate deformation", *IEEE Photonics Technology Letters*, vol. 19, no. 16, pp. 1242–1244, 15 August 2007.

List of Authors

Emmanuel ANDRÉ
Néel Institute – CNRS
Grenoble
France

Jean-Michel AUBERLET
IFSTTAR – COSYS – LEPSIS
Bouguenais
France

Sébastien AUBIN
LUNAM University
ESEO
Angers
France

Abdellatif BARAKET
University Claude Bernard Lyon 1
CNRS
ISA – Institut des Sciences Analytiques, Equipe SIMS (Surfaces (bio)-Interfaces Micro/nano Systèmes)
Villeurbanne
France

Isabelle BARBEREAU
Thales Air Systems
Limours en Hurepoix
France

François BESSUEILLE
University Claude Bernard Lyon 1
CNRS
ISA – Institut des Sciences Analytiques, Equipe SIMS (Surfaces (bio)-Interfaces Micro/nano Systèmes)
Villeurbanne
France

Laurianne BLANC
University François Rabelais de Tours
CNRS, CEA, INSA-CVL, GREMAN UMR 7347
Blois
France

Cédric BOISSIÈRE
Laboratoire LCMCP – UMR CNRS 7574
UPMC
Paris
France

Olivier BOURGEOIS
Néel Institute – CNRS
Grenoble
France

Thierry BOSCH
LAAS-CNRS
ENSEEIHT
Toulouse
France

Patrice BRIAND
CETE de l'Ouest
Laboratoire LRPC
Les Ponts-de-Cé
France

Mourad CHTIOUI
Thales Air Systems
Limours en Hurepoix
France

Olivier CLOUARD
ENSICAEN
Caen
France

Stéphane COTTE
University Claude Bernard Lyon 1
CNRS
ISA – Institut des Sciences Analytiques, Equipe SIMS (Surfaces (bio)-Interfaces Micro/nano Systèmes)
Villeurbanne
France

Corinne DEJOUS
University of Bordeaux
IMS, CNRS UMR 5218, IPB
Talence
France

Abdelhamid ERRACHID
University Claude Bernard Lyon 1
CNRS
ISA – Institut des Sciences Analytiques, Equipe SIMS (Surfaces (bio)-Interfaces Micro/nano Systèmes)
Villeurbanne
France

Aitor FERNANDEZ LOPEANDIA
Néel Institute – CNRS
Grenoble
France

Najla FOURATI
SATIE, UMR 8029 CNRS
ENS Cachan
CNAM
Paris
France

Jean-Luc GARDEN
Néel Institute – CNRS
Grenoble
France

Hervé GILLES
Centre de Recherche sur les Ions, les Matériaux et la Photonique
UMR 6252, CNRS, CEA
ENSICAEN
University of Caen
Caen
France

Sylvain GIRARD
Centre de Recherche sur les Ions, les Matériaux et la Photonique, UMR 6252, CNRS, CEA
ENSICAEN
University of Caen
Caen
France

Dominique GIVORD
Néel Institute – CNRS
Grenoble
France

Philippe GOUPIL
EYCCC Flight Control System
AIRBUS Operations S.A.S.
Toulouse
France

Stéphane GOUT
University Claude Bernard Lyon 1
CNRS
ISA – Institut des Sciences
Analytiques, Equipe SIMS (Surfaces
(bio)-Interfaces Micro/nano
Systèmes)
Villeurbanne
France

Didier LEONARD
University Claude Bernard Lyon 1
CNRS
ISA – Institut des Sciences
Analytiques, Equipe SIMS (Surfaces
(bio)-Interfaces Micro/nano
Systèmes)
Villeurbanne
France

Philippe LEPRINCE
Centre de Recherche sur les Ions, les
Matériaux et la Photonique
UMR 6252, CNRS, CEA
ENSICAEN
University of Caen
Caen
France

Guillaume LESUEUR
Thales Air Systems
Limours en Hurepoix
France

Benoît MARX
Centre de Recherche en Automatique
de Nancy (CRAN)
UMR 70939, CNRS
University of Lorraine
Vandoeuvre-lès-Nancy
France

Thomas MERLET
Thales Air Systems
Limours en Hurepoix
France

Patrick PLAINCHAULT
LUNAM University
ESEO
Angers
France

José RAGOT
Centre de Recherche en Automatique
de Nancy (CRAN)
UMR 7039, CNRS
University of Lorraine
Vandoeuvre-lès-Nancy
France

Dominique REBIÈRE
University of Bordeaux
IMS, CNRS UMR 5218, IPB
Talence
France

Jean-Hugh THOMAS
University of Maine
LAUM UMR CNRS 6613
Le Mans
France

Grégory TORTISSIER
University of Bordeaux
IMS, CNRS UMR 5218, IPB
Talence
France

Do Hieu TRINH
Centre de Recherche en Automatique
de Nancy (CRAN)
UMR 7039, CNRS
University of Lorraine
Vandoeuvre-lès-Nancy
France

Nourdin YAAKOUBI
University of Maine
LAUM UMR CNRS 6613
Le Mans
France

Chouki ZERROUKI
SATIE, UMR 8029 CNRS
ENS Cachan
CNAM
Paris
France

Index

A, B, C, D

AC calorimetry, 70–71
antenna, 125–146
antigen-antibody recognition, 42–43
bragg network, 110, 111
coast summits, 107, 108
deformation, 126

E, F, G, I

electrodes, 2, 7, 8, 76
electroless, 2, 3, 6
ellipsometry, 20, 21
fault detection and isolation, 86
$GdAl_2$, 81–82
immunosensor, 35, 36, 42, 43, 54–62

L, M

localized metallization, 2
love waves, 12, 13, 19, 25
mesoporous materials, 13–16
microcontact printing, 1–3
microfabrication, 2, 69, 70

N, O, P

optical sensor, 127, 129, 130, 132–139, 141
oscillatory failures, 85, 86
parylene, 71, 72, 74, 76, 77, 79
peeling, 2–3

R, S

radar, 125
rumble strips, 109, 121, 122
secondary road, 119
soft lithography, 1
soft sensor, 86, 88–90
surface acoustic wave (SAW) sensor, 36

Other titles from

in

Instrumentation and Measurement

2014

APPRIOU Alain
Uncertainty Theories and Multisensor Data Fusion

2012

LALAUZE René
Chemical Sensors and Biosensors

LE MENN Marc
Instrumentation and Metrology in Oceanography

2011

GROUS Ammar
Applied Metrology for Manufacturing Engineering

2009

FRENCH COLLEGE OF METROLOGY
Transverse Disciplines in Metrology

2008

LALAUZE René
Physical Chemistry of Solid-Gas Interfaces

2007

KUNDU Tribikram
Advanced Ultrasonic Methods for Material and Structure Inspection

PLACKO Dominique
Fundamentals of Instrumentation and Measurement

RIPKA Pavel, TIPEK Alois
Modern Sensors Handbook

2006

BALAGEAS Daniel *et al.*
Structural Health Monitoring

FRENCH COLLEGE OF METROLOGY
Metrology in Industry